This is to certify that the

thesis entitled

INSTABILITIES OF SPREADING DIFFUSION FLAMES IN MICROGRAVITY AND THE DESIGN AND CONSTRUCTION OF A HELE-SHAW APPARATUS THAT PRODUCES FLAMES IN THE NEAR EXTINCTION LIMIT REGIME UNDER SIMULATED LOW GRAVITY CONDITIONS

presented by

Lisa Marie Oravecz

has been accepted towards fulfillment
of the requirements for

MS degree in Mechanical Engineering

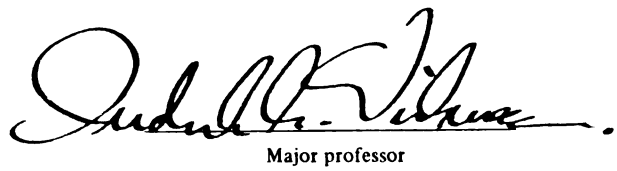

Major professor

Date 4/26/01

INSTABILITIES OF SPREADING DIFFUSION FLAMES IN MICROGRAVITY AND THE DESIGN AND CONSTRUCTION OF A HELE-SHAW APPARATUS THAT PRODUCES FLAMES IN THE NEAR EXTINCTION LIMIT REGIME UNDER SIMULATED LOW GRAVITY CONDITIONS

By

Lisa Marie Oravecz

A THESIS

Submitted to
Michigan State University
in partial fulfillment of the requirements
for the degree of

MASTER OF SCIENCE

Department of Mechanical Engineering

2001

ABSTRACT

INSTABILITIES OF SPREADING DIFFUSION FLAMES IN MICROGRAVITY AND THE DESIGN AND CONSTRUCTION OF A HELE-SHAW APPARATUS THAT PRODUCES FLAMES IN THE NEAR EXTINCTION LIMIT REGIME UNDER SIMULATED LOW GRAVITY CONDITIONS

By

Lisa Marie Oravecz

Microgravity diffusion flame instabilities is a growing area of research due to the direct applications to the safety of space flight. Experiments, which are part of the "Flight Definition Project", named "ATHINA", for NASA were conducted at the 2.2 and 5 Second Drop Towers, in which regions of oscillatory instabilities were observed. Spreading flame fronts fragmented into "flamelets" which oscillated, recombined, or extinguished. Flamelet oscillations were of order 1Hz. Blue intensity measurements of flamelets oscillated suggesting periodic variation of chemical processes. Microgravity flame spread rates of fronts and flamelets were lower than normal gravity front rates due to lack of buoyancy. Fuel surface energies were calculated, and a "critical energy flux" was identified relating number of flamelets to losses at the sample surface.

A Hele-Shaw apparatus named the "MSU Flame Rig" (under ATHINA project) was designed and constructed to produce diffusion flame instabilities in a simulated microgravity environment. Flame instabilities similar to NASA experiments and unlimited test times indicated the device could be employed to determine thick fuels that will be tested on the International Space Station. Unstable flame behaviors unlike those in the drop tower tests showed flames to pulse, form blue cusps, and create fingering patterns. Flamelets and pulses oscillated at much higher frequencies than NASA tests.

I dedicate this thesis to:

My Husband, Ray for his love and support of me pursuing my life's endeavors,
My Parents for showing me how to be brave and work hard,
And Myself for continuing to strive for my dreams.

insight

outstan

of advi

team. Fi

their va

igniter a

I

Combust

the use o

ACKNOWLEDGEMENTS

I would like to thank my advisor Dr. Indrek Wichman for his excellent guidance, insight, and support, and also for giving me the opportunity to work on such an outstanding project with NASA.

I would also like to thank Dr. Sandra Olson and Dr. Fletcher Miller for their hours of advice, assistance, and support for this project. Thank you to the rest of the ATHINA team, Frank Vergilii, Jim Bruewer, John Thomas, Bill Camperchioli, and Phil Stehno for their valuable input on building the MSU Flame Rig particularly in the design of the igniter and selection of diagnostic equipment.

I would also like to thank the NASA Glenn Research Center Microgravity Combustion Branch for funding this project under the NASA Contract *NCC3-662*, and the use of their drop tower facilities.

TABLE OF CONTENTS

LIST OF TABLES viii

LIST OF FIGURES ix

NOMENCLATURE xiii

INTRODUCTION 1

CHAPTER 1
LITERATURE SURVEY 7
- 1.1 OVERVIEW 7
- 1.2 DE RIS ANALYSIS OF SPREADING DIFFUSION FLAMES 9
  - 1.2.1 THEORY 9
  - 1.2.2 THIN FUEL RESULTS 11
  - 1.2.3 SEMI-INFINITE MODEL RESULTS 12
- 1.3 OTHER WORKS OF DIFFUSION FLAME SPREAD IN NORMAL GRAVITY 13
- 1.4 DIFFUSION FLAME SPREAD IN MICROGRAVITY 16
- 1.5 DIFFUSION FLAME INSTABILITIES 19
- 1.6 CANDLE FLAME IN MICROGRAVITY 22
- 1.7 INSTABILITIES IN SIMULATED MICROGRAVITY ENVIRONMENTS 24
  - 1.7.1 LOW STRETCH FLAMES 24
  - 1.7.2 HELE-SHAW APPARATUS 25
  - 1.7.3 MICROGRAVITY FLAME SPREAD LIMITS IN HELE-SHAW TYPE DEVICES 26

CHAPTER 2
EXPERIMENT 29
- 2.1 OVERVIEW 29
- 2.2 NASA COMBUSTION TUNNEL RIG 30
  - 2.2.1 NASA SAMPLES 30
  - 2.2.2 NASA TEST CONDITIONS AND FLOW SYSTEM 33
  - 2.2.3 NASA RIG ELECTRICAL SYSTEM AND DIAGNOSTICS 37
  - 2.2.4 NASA DROP TOWER FACILITIES 39
  - 2.2.5 NASA RIG TEST PROCEDURE 45
- 2.3 MSU FLAME RIG 48
  - 2.3.1 MSU FLAME RIG MATERIALS 48
  - 2.3.2 MSU FLAME RIG FLOW CONTROL AND MEASUREMENT 49
  - 2.3.3 MSU FLAME RIG PLENUM AND CONTRACTION 53

CH
CA

CHAPTE
RESULT
4.
4.

4.3

2.3.4 MSU FLAME RIG POROUS PLATE..... 55
2.3.5 FLOW IN THE MSU FLAME RIG TEST SECTION..... 59
2.3.6 MSU SAMPLES..... 60
2.3.7 MSU FLAME RIG SAMPLE HOLDER AND SUBSTRATE..... 61
2.3.8 MSU FLAME RIG IGNITER..... 63
2.3.9 MSU FLAME RIG SPACERS..... 65
2.3.10 MSU FLAME RIG DIAGNOSTICS..... 68
2.3.11 MSU FLAME RIG TEST PROCEDURE..... 69

CHAPTER 3
CALCULATIONS..... 72
3.1 OVERVIEW..... 72
3.2 NASA CALCULATIONS..... 72
3.2.1 SURFACE ENERGY BALANCE DATA REDUCTION CALCULATIONS..... 72
3.2.2 TEMPERATURE DERIVATIVE CALCULATION..... 76
3.2.3 PEAK TEMPERATURE ENERGY LOSS VERSUS FLAMELETS CALCULATION..... 82
3.2.4 FLAME VELOCITIES..... 82
3.3 MSU FLAME RIG CALCULATIONS..... 83
3.3.1 SCALE ANALYSIS..... 83
3.3.2 MASS FLOWRATE CALCULATIONS..... 90
3.3.3 VOLUMETRIC FLOWRATE CORRECTION AND CONVERSION..... 91
3.3.4 POROUS PLATE CALCULATIONS..... 93
3.3.5 PLENUM FILL TIME CALCULATIONS..... 96
3.3.6 ENTRANCE LENGTH AND BOUNDARY LAYER CALCULATIONS..... 97

CHAPTER 4
RESULTS AND DISCUSSION..... 106
4.1 OVERVIEW..... 106
4.2 NASA DROP TOWER RESULTS AND DISCUSSION..... 106
4.2.1 NASA INSTABILITY REGIONS..... 106
4.2.2 NASA INSTABILITY CHARACTERISTICS..... 112
4.2.3 NASA FLAMELET OSCILLATIONS..... 119
4.2.4 NASA FLAME SPREAD RATES..... 125
4.2.5 NASA SURFACE ENERGY BALANCES..... 127
4.2.6 NASA PEAK TEMPERATURE SURFACE ENERGY BALANCES..... 129
4.3 MSU FLAME RIG RESULTS AND DISCUSSION..... 131
4.3.1 MSU FLAME RIG FLOWMETER VERIFICATION..... 131
4.3.2 MSU FLAME RIG FLAME INSTABILITIES..... 136
4.3.3 DISCUSSION OF MSU FLAME RIG VERSUS DROP TOWERS..... 151

CHAP
CONC

CHAP
FUTU

BIBLIC

CHAPTER 5
CONCLUSIONS..... 153

CHAPTER 6
FUTURE WORK..... 155

BIBLIOGRAPHY..... 158

LIST OF TABLES

Table 1.	Constants of surface energy balance equation.	75
Table 2.	Pressure ratio scaling values in the MSU Flame Rig.	89
Table 3.	Ranges of volumetric flow rates in MSU Flame Rig.	90
Table 4.	Pressure calculations for determining porous plate pressure drop.	93
Table 5.	Entrance length ranges in plane parallel to tunnel side walls.	100
Table 6.	Entrance lengths in the plane parallel to quartz plate.	101
Table 7.	Boundary layer thickness at the beginning and end of sample.	104
Table 8.	Experimental results for drop tower tests with aluminum foil substrate.	110
Table 9.	Experimental results for drop tower tests with steel substrate.	111

LIST OF FIGURES

Images in this thesis are presented in color.

Figure 1. Diffusion flame spreading over a solid surface [2]. 9

Figure 2. NASA sample front and side schematic. 31

Figure 3a. Flat, linear flame front in 1-g. 32
Figure 3b. Parabolic flame front in 1-g. 32

Figure 4. Flat, linear flame front in microgravity. 33

Figure 5. Flammability Map of Olson [24, 26] with new extinction limit branch. 34

Figure 6a. Schematic of flow system in Combustion Tunnel Rig. 36
Figure 6b. Picture of flow system in Combustion Tunnel Rig. 36

Figure 7. 2.2 Second Drop Tower schematic. 41

Figure 8. Drag shield in 2.2 Second Drop Tower. 42

Figure 9. Zero-G or 5 Second Drop Tower facility. 43

Figure 10. Drag shield in the Zero-G Drop Tower. 44

Figure 11. Picture of MSU Flame Rig. 48

Figure 12a. Picture of MSU Flame Rig flow system. 50
Figure 12b. Block diagram of MSU Flame Rig flow system. 50

Figure 13a. Uniform, flat flame front in MSU Flame Rig. 52
Figure 13b. Corrugated, unstable flame front in MSU Flame Rig. 52

Figure 14. MSU Flame Rig plenum schematic. 54

Figure 15. MSU Flame Rig contraction in flow system. 55

Figure 16. Air path through porous plate in MSU Flame Rig. 56

Figure 17. Double blocking plate system for porous plate in MSU Flame Rig. 57

Figure 18. Schematic of MSU Flame Rig exhaust. 59

Figure 19. MSU Flame Rig sample holder system. 62

Figure 20a. Picture of MSU Flame Rig igniter system. 64

Figure 20b. Schematic of MSU Flame Rig igniter system. 64

Figure 21. System of MSU Flame Rig spacers. 66

Figure 22. MSU Flame Rig camera mounting system. 68

Figure 23. Fuel surface energy balance. 73

Figure 24. Schematic for scaling analysis of MSU Flame Rig. 83

Figure 25. Calculation of test section velocities in MSU Rig from rotameter readings. 91

Figure 26. Pressure versus velocity behavior for Mott porous plates. 95

Figure 27. Plenum fill time calculations in MSU Flame Rig. 96

Figure 28. Entrance length in plane parallel to tunnel sides in MSU Flame Rig. 98

Figure 29. Momentum and mechanical energy balances [54]. 99

Figure 30. Boundary layers in plane parallel to quartz plate in MSU Flame Rig. 102

Figure 31. Sample location and boundary layers in MSU Flame Rig test section. 104

Figure 1

Figure 2
Figure 2

Figure 3

Figure 3

Figure 3
Figure 3

Figure 3
Figure 3

Figure 3

Figure 3

Figure 4

Figure 4

Figure 4

Figure 4

Figure 4

Figure 43

Figure 44

Figure 45

Figure 46a

Figure 32. Typical drop tower test showing flamelet formation and interactions. 108

Figure 33a. Flamelet top view. 112
Figure 33b. Flamelet side view. 112

Figure 34. Side view of progression of flamelet extinction. 113

Figure 35. Typical spacing between three flamelets. 115

Figure 36a. Test with close flamelets. 115
Figure 36b. Combination of flamelets. 115

Figure 37a. Spherical flamelet. 116
Figure 37b. Oval flamelet. 116

Figure 38. Typical test with faster side flamelets. 118

Figure 39. Time sequence of right flamelet oscillations. 120

Figure 40a. Examples of time periods of major axis flamelet oscillations. 122
Figure 40b. Major axis of oval flamelet. 122

Figure 41. Line profile along which intensity measurements were taken. 123

Figure 42a. Intensity in blue region over drop time along line profile in Figure 41. 124
Figure 42b. Intensity measurement for single frame of drop with flamelet along line profile in Figure 41. 124

Figure 43. Flame speeds versus substrate distances and air flowrates. 126

Figure 44. Typical surface energy balances for 2 second drops. 128

Figure 45. Number of flamelets versus peak energy losses. 130

Figure 46a. Setup for verifying flowmeter at atmospheric conditions. 133

Figure 46b. Volume flowrates of flowmeter at atmospheric conditions for two orifices. 133

Figure 47a. Setup for verifying flowmeter at inline pressure conditions. 135

Figure 47b. Comparison of flowmeter to calibrated orifice at inline conditions. 135

Figure 48. Typical progression of MSU Flame Rig test. 137

Figure 49. Oscillatory motion of entire flame front in MSU Flame Rig test. 139

Figure 50. Time sequence of uniform flame front changing into flamelets in MSU Flame Rig. 140

Figure 51. Periodic pulses travelling across flame front in MSU Flame Rig. 141

Figure 52. Periodic pulses that extinguish flamelets and flame fronts in MSU Flame Rig. 143

Figure 53. MSU Flame Rig test with unstable flamelets producing fingering pattern. 145

Figure 54. MSU Flame Rig tests with stable cusp flames and unstable flamelets. 146

Figure 55. Burn out of sample by thin flame front in MSU Flame Rig. 149

NOMENCLATURE

A_s	Pre-exponential factor for pyrolysis of fuel (s^{-1})
c_p	Specific heat of cellulosic fuel (J/(kg K))
E_s	Activation energy for fuel pyrolysis (kJ/mol)
g	Acceleration of gravity (9.8 m/s^2)
h	MSU Rig test section height (cm)
D	MSU Rig test section length (cm)
L	Distance between fuel and substrate(cm)
L_v	Heat of Evaporation for cellulosic fuel (kJ/kg)
P	Total Pressure (psi)
R	Universal gas constant (8.314 J/(mol K))
Ra_h	Raleigh number based on test section height h
Re_x	Reynolds number based on dimension x
T_s	Temperature of fuel surface (K)
T_b	Temperature of substrate backing (K)
T_a	Temperature of ambient surroundings (K)
u	Velocity of oxidizer in x direction (parallel to fuel sample) (cm/s)
v	Velocity of oxidizer in y direction (parallel to test section height) (cm/s)
v_f	Flame spread rate (cm/s)
α	Thermal diffusivity of air (m^2/s)
β	Volume expansion coefficient for air at constant pressure (K^{-1})
ε_b	Substrate surface emissivity

ε_s	Fuel surface emissivity
λ_{air}	Thermal conductivity of air W/(m K)
ν	Kinematic viscosity of air (m^2/s)
ρ	Density of air (kg/m^3)
ρ_s	Fuel surface density (kg/m^3)
σ	Stefan-Boltzmann constant ($5.67 * 10^{-8}$ $W/(m^2 K^4)$)
τ	Half thickness of cellulosic fuel (in)

Subscripts

a	Ambient
air	Air
b	Backing or substrate
f	Flame
h	Test section height
s	Surface
v	Vaporization

INSTABILITIES

INTRODUCTION

Combustion provides the majority of useful energy production in the world, which makes it an important area of research. However, combustion has often been a double-edged sword in its use by mankind. While combustion has produced efficient power plants, automobile engines, and gas and oil stoves to cook food and heat homes, it has also produced destructive elements such as forest fires and harmful pollution, which are in most cases products of technological growth. Nonetheless, scientists are working everyday to remedy the undesired effects of combustion while moving forward to better society with its benefits. In this respect, progress in combustion science is a worthwhile endeavor. Therefore, research in this area must be conducted in a careful yet ambitious manner.

Combustion involves many intricate processes that are coupled to each other. Therefore, the combustion scientist must be proficient in several areas; fluid dynamics, chemistry, heat transfer and thermodynamics. Such studies have produced more complete and coherent flame theories, in which flames are categorized as either premixed or diffusion flames. The complicated nature of diffusion flames has caused them to be investigated less than premixed flames, which have been studied extensively. In a diffusion flame, the fuel and oxidizer are not mixed prior to combustion, whereas in premixed flames the fuel and oxidizer have mixed before combusting. Detailed studies of these flames are crucial to understanding real world combustion scenarios because diffusion flames occur more frequently in both nature and technology than premixed flames. Most flames we see are diffusion flames: candles, matches, gas jet burners, jet engines, and wood burning stoves. Some important investigations produced theories that

serve as the foundation for diffusion flame research. Burke and Schumann [1] developed a mathematical description of laminar jet flames that agreed well with experiments, while deRis [2] contributed a theory of laminar flame spread over both thick and thin fuels by neglecting reaction kinetics.

With the advent of the space program over the last few decades, microgravity flames have become a significant area of combustion research. The practical motivation behind understanding this field of study is fire safety in space vehicles like the shuttle and International Space Station (ISS). In the study by Friedman [3], fire safety in spacecraft was investigated. Most of the prevention and defense tactics against fires in space has been established from experience of fires in enclosed cabins like airliners. However, more intensive studies focusing on the fundamental nature of microgravity flames will lead to a firmer basis for microgravity fire safety strategies.

Fuel, oxidizer, and a heat or ignition source are the three factors required for a fire. Microgravity combustion safety is based on prevention of these factors by either control or total removal. The control of fuel is achieved by a systematic process of determining those materials with low upward flame spread in normal gravity. This material testing on earth is actually a worst case scenario since microgravity flames are much less robust than 1-g flames due to the absence of buoyancy. Although many materials produce high flame spread rates, they are controlled by properly reserving them in safe areas. Ignition is restricted by employing circuit breakers and electrical grounding, and safeguarding against conditions that could lead to a spark. The oxidizer cannot be controlled since it is vital for survival in space. For example, the space shuttle contains

21% oxygen at 1 atmosphere during normal operation, and 30% enriched sea level air at 72 kilo-Pascal reduced total pressure for Pre-Extra Vehicular Activities.

As larger space vehicles are constructed, the probability that the crew will detect a fire decreases. It is impossible to prevent fires completely on the shuttle and space station, however, NASA is continuously developing sensitive detectors and effective extinguishing methods. Currently, the fire detection and suppression system on the space shuttle consists of ionization type smoke detectors that identify smoke in microgravity. Non toxic fire extinguishers containing CO_2 that will not exceed a dangerous concentration level can suppress on board fires.

Characterizing the nature of microgravity fires for many materials under various conditions is an equally important task that NASA strives to improve. Besides the practical safety applications, quantitative explanations will lead to fundamental theories of low gravity flames. Furthermore, many of the underlying mechanisms of on-earth flames are masked by buoyancy, which causes a churning motion that increases the mixing of the fuel and oxidizer and produces a more vigorous flame. In microgravity however, processes that were quashed in 1-g are now dominant mechanisms. An understanding of these processes will give a more complete picture of what really occurs in 1-g flames. Since approximately 85% of the United State's energy come from combustion, this knowledge is crucial. Any improvement in the efficiency in nuclear, solar, or hydropower plants, automobiles, jet engines, or even outdoor grills could save millions or perhaps billions of dollars.

Flames near extinction that are in either microgravity or on earth behave in peculiar ways, and it is very important to determine the conditions under which these

flames will survive or quench. In fact, the consequences of not detecting and extinguishing a flame on board the shuttle or space station would be disastrous. Microgravity diffusion flames near extinction exhibit very unstable behaviors. Research by Dietrich *et al.* [4] showed that candle flames onboard the Space Shuttle and Mir oscillated before extinguishing with periodic increases and decreases of flame surface area. Diffusion flames examined by Olson [5] in a simulated microgravity environment in low stretch conditions fragmented into cellular flames that also oscillated and meandered across the fuel surface prior to extinction. In another study by Olson *et al.* [6], microgravity flames smoldering over thin fuels produced fingerlike flames that wandered over the fuel samples. The above examples indicate the elaborate nature of microgravity flame instabilities. Furthermore, because these flames break apart into smaller cellular flames, which can travel across the fuel, detection of them may be difficult. Knowledge of microgravity flames in the "near extinction limit regime" is limited because space exploration is still quite young. However, knowing the conditions where these instabilities occur, and the underlying processes that prolong unstable flames that could undergo a transition into a dangerous fire in low gravity is of the utmost importance for space travel safety.

In general, flame instabilities in microgravity are attributed to two mechanisms. These are thermal diffusive and hydrodynamic instabilities. Thermal diffusive instability processes occur when an imbalance in the mass and heat transfer in the flame presents itself as a bulge at various points along the flame sheet. The hydrodynamic instability occurs when differential thermal expansion of the gases across the flame sheet shows itself as a corrugation in the flame front. A spreading diffusion flame in microgravity at

the n

flame

displa

Analy

Atmo

diffusi

diffusi

endeav

instabil

produce

Therma

instabili

extinctio

making

time in

Space S

experime

will focu

which is

flame ins

those foun

Rig will b

the near extinction limit becomes corrugated and later fragments into smaller separate flames called flamelets. These flamelets may oscillate, recombine, or extinguish thus displaying their unstable and complicated nature.

The overall goal of the NASA flight project named "ATHINA" (stands for Analysis of Thermodiffusive and Hydrodynamic Instabilities in Near-extinction Atmospheres), which funded this thesis, is determining the extent to which the thermal diffusive and hydrodynamic mechanisms contribute to causing instabilities of a spreading diffusion flame in microgravity. This thesis is the first step in accomplishing this endeavor. In the first part of this thesis, the parameter ranges, in which diffusion flame instabilities of a wide thermally thin sample in a microgravity environment occur, will be produced and experimentally investigated using the NASA Combustion Tunnel Rig. Thermally thin fuels are required in the drop tower to study microgravity flame instabilities because their spread rate is sufficiently fast to observe the near limit extinction behavior. Thicker fuels have much slower flame spread rates than thin fuels, making it very difficult to observe instabilities in the two or five seconds of microgravity time in the drop tower experiments. Even though most combustible materials on the Space Shuttle and ISS are considered thick, thermally thin fuels provide valuable experiments that can be used to understand thicker fuels. The second part of this thesis will focus on the design, construction, and preliminary testing of the "MSU Flame Rig", which is a Hele-Shaw apparatus that simulates a low gravity environment and produces flame instabilities in the near extinction limit regime. The instabilities are similar to those found in the NASA drop tests. The overall future primary use of the MSU Flame Rig will be to examine and select thick fuels that will fly on the International Space

Station under the ATHINA project. It will also be used to provide additional results to the drop tower studies for thin fuel flame instabilities. Since there is no limit to the testing time of the MSU Flame Rig, long periods of simulated low gravity can be produced, so long-time unstable flame characteristics in this environment will be observed. The success of the MSU Flame Rig will be important to the NASA flight project because many materials that are potential fuels for a dangerous fire on the Space Shuttle or ISS are not thermally thin. This research is important for the space program because experiments of this nature and the study of low gravity unstable flame behavior is still a relatively new area of study.

This project will be a collaborative effort between NASA Glenn Research Center Microgravity Combustion Branch and Michigan State University. This thesis is one component of the larger "flight definition" project called ATHINA for NASA. "Flight definition" means that if certain scientific requirements are met, the experiment will be scheduled to fly on the International Space Station (ISS) in the future. Therefore, much of this work is preliminary and will serve as a basis for some of the requirements that must be met to fly on the ISS.

CHAPTER 1
LITERATURE SURVEY

1.1 Overview

Flames are categorized as two types: premixed flames and diffusion flames. A premixed flame is one in which the fuel and oxidizer are premixed at the molecular level before combustion, and a diffusion flame is one in which the fuel and oxidizer are not mixed prior to combustion. In many systems, it is not necessarily advantageous to assert this distinction because different regions of the flame may have both diffusion and premixed combustion. An example would be the internal combustion engine. From a global perspective, the internal combustion engine contains a mixture of fuel vapor and oxidizer that is sparked to produce combustion. However, on a microscopic scale, the fuel vapor is really a gas comprised of many tiny droplets that are surrounded by a flame sheet. Therefore, the individual droplets can be categorized as diffusion flames.

Premixed flames have been investigated more extensively because, unlike diffusion flames, they can provide fundamental flame characteristics such as burning velocity or temperature. The burning velocity is more commonly referred to as flame speed and is the velocity at which the flame travels into the unburned fuel/oxidizer mixture. The fuel-to-oxidizer ratios as well as type of fuel and oxidizer are main factors that affect these speeds, which can be important to combustion safety science. Examples of premixed flames are Bunsen burners and spark-ignition engines. In this thesis, the flames studied were diffusion flames because the fuel is a solid.

Diffusion flames have been studied less than premixed flames due to their complex nature. Most flames are of this type in which the fuel and oxidizer have not formed a mixture prior to combustion. When ignition occurs, the fuel and oxidizer

diffuse toward each other and the reaction occurs in a zone between the reactants forming a flame sheet. Diffusion flames are complex because they have no fundamental characteristic that can be identified to them such as flame velocity or mixture strength although overall mass burning rates can be readily calculated. Because of this, scientists in the early stages of diffusion flame research concentrated on flame height and shape and their affect on soot formation, flame stability, and burning rates. Since most flames in nature are diffusion flames, scientists are continually studying them to improve engine efficiencies, and fire safety. Examples of diffusion flames are gas jets, coarse oil sprays or droplet combustion in diesel engines and gas turbines, candle flames, and forest fires.

Since this thesis involved flames spreading over a solid fuel, this literature review will begin with one of the first monumental studies of flame spread theory in normal gravity. A brief history of some of the significant works on diffusion flame spread follows in Section 1.3. Section 1.4 covers past research in microgravity diffusion flame spread, and Section 1.5 discusses flame instability work in both normal gravity and microgravity. Section 1.6 discusses the candle flame in microgravity, and Section 1.7 describes studies that simulated diffusion flames in microgravity. These last works in Section 1.7 inspired the second part of this thesis, which involved the construction of an apparatus that simulates the "near extinction limit regime" of spreading diffusion flames in low gravity. All sections will present the work in a chronological order to illustrate the development of areas of research while showing how they are related to each other.

1.2 deRis Analysis of Spreading Diffusion Flames

1.2.1 Theory

In 1969, J.N. deRis [2] produced a classic study on the thermal theory of a spreading diffusion flame in an opposed flow configuration in which the oxidizer and flame travel in opposite directions shown in Figure 1. deRis was the first to provide an analytical solution to the flame spread problem in two dimensions for both a thin and a semi-infinite fuel bed. Because this was a landmark study and this thesis involves a flame spreading over a thin fuel, a more detailed description will be presented here.

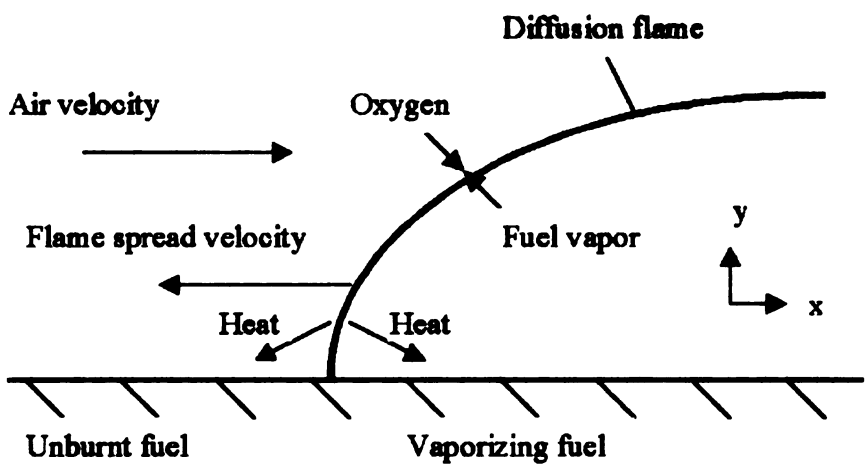

Figure 1. Diffusion flame spreading over a solid surface [2].

In his theory, deRis assumed the following.

1. Heat Transfer

    a. The constant air velocity affected the forward gas phase conduction.

b. Constant gas phase properties and a uniform velocity profile were assumed.

c. Downstream convection was accounted for in both the thin and semi-infinite cases, but radiation was only included for the semi-infinite case.

d. The thin fuel was so thin that there was a uniform temperature distribution across it, however, the thick fuel used the fully conductive solution for temperature.

e. Gravitational buoyant effects were negligible.

2. Fuel Vaporization

a. The fuel was initially in the condensed solid phase and had not yet vaporized.

b. When the flame approached, fuel surface temperature increased sharply causing the fuel surface to sublime. deRis assumed that the fuel vapor pressure was strongly dependent on temperature.

c. The fuel does not vaporize until it reaches the vaporization temperature.

3. Mass Transfer

a. Diffusion and convection of fuel vapor, products, oxygen, and inert gases were assumed.

b. Fuel mass transfer in the vertical direction off the fuel surface was by diffusion, and the boundary conditions at the surface of the fuel were linearized to give an approximation of perpendicular convection.

4. Gas-Phase Combustion

a. Combustion occurred only in the gas phase.

b. Fuel and oxygen reacted instantly upon mixing, indicating that the mass transfer of the reactants rather than the chemical kinetics governed the rate of combustion. This was referred to as "infinitely fast kinetics" (Burke-Schumann solutions). The flame sheet was located directly between fuel and oxidizer zones that did not overlap.

c. Schvab-Zeldovich diffusion flame theory was used.

1.2.2 Thin Fuel Results

Using the above assumptions and fuel theory, deRis solved the thin fuel case first by employing a single global reaction equation, species, mass, and energy equations. He obtained a set of solvable ordinary differential equations by taking the Fourier transform of the governing partial differential equations, and produced the following relation between the flame spread rate and flame temperature shown in Equation 1.

$$\rho_\omega C_{p\omega} \tau V (T_{vap} - T_\infty) \cong \sqrt{2}\lambda (T_f - T_{vap}) \qquad (1)$$

In this equation, the constant properties ρ_ω, τ, λ, T_∞, $C_{p\omega}$, T_{vap} are the fuel bed density, fuel bed thickness, gas phase conductivity, far field temperature, fuel bed specific heat, and the fuel bed vaporization temperature. The remaining variables T_f and V are the adiabatic flame temperature and flame speed respectively. The left side of Equation 1 represents the amount of heat required for fuel vaporization, whereas the right side represents the conductive heat that travels ahead of the flame in the gas phase. Equation 1 is an important result illustrating that the flame speed V depends on the adiabatic stoichiometric flame temperature with linearized mass transfer, T_f. Therefore, flame speed is independent of pressure and air velocity for a thermally thin fuel. However,

Equation 1 cannot be applied to lower oxygen concentration limits, when the flame is near extinction, because reaction kinetics become important and the thin flame sheet Burke Schumann approximation is no longer valid.

1.2.3 Semi-Infinite Model Results

The semi-infinite model governing equations consisted of the same gas phase equations as in the thin fuel case as well as the full solid phase equations for the fuel bed. In the solid equations, both conduction and radiation were included. A system of equations was formed with the gas phase and solid phase equations, and an eigenvalue relation was formed from the fuel bed relations. A solution was obtained by transforming the governing equations to three simultaneous Wiener-Hopf integral equations that were solved exactly. The result was a relation between the flame temperature T_f and the flame spread rate V shown in Equation 2.

$$\left\{\frac{T_f - T_{vap}}{T_{vap} - T_\infty} + \frac{2R_1 F(2\lambda / \rho C_p V_a l_1}{\rho C_p V_a (T_{vap} - T_\infty)} + \frac{2R_2}{\pi \rho C_p V_a (T_{vap} - T_\infty)}\right\}^2 = \frac{\rho_\omega C_{p\omega} \lambda_{\omega y} V}{\rho C_p \lambda V_a} \qquad (2)$$

Equation 2 contains the same constants as in Equation 1 as well as the constant values of gas phase density ρ, gas phase specific heat C_p, radiation constants R_1, R_2, l_1, fuel bed conduction in the y direction $\lambda_{\omega y}$, and air velocity V_a. As in the thin fuel model, Equation 2 gives a relation between the flame velocity V and the adiabatic flame temperature. The semi-infinite model, however, also includes a dependence on the air velocity V_a, which was not obtained in the thin fuel case. The first two terms on the left side are the forward heat transfer in the gas phase, while the last term is the forward and downstream radiative heat transfer. If radiation is neglected though (R_1=R_2=0), the thin fuel equation is retained.

In deRis' PhD thesis [7], the effect of radiation on the distance between flame and fuel, or standoff distance was calculated. For the semi-infinite problem, the flame is close to the fuel, however, for no radiation, the flame touches the surface, which may cause extinction. Therefore, for thick fuels, the flame spread rate is lower since more heat is lost to the fuel surface.

The analysis by deRis showed that for thin fuels, the pressure and oxidizer velocity do not affect the flame spread rate when reaction kinetics are ignored. For thicker fuels, an equation was derived that revealed the influences of radiation on flame spread velocity. The solution was approximate and exhibits physically realistic behavior.

1.3 Other Works of Diffusion Flame Spread in Normal Gravity

The work of deRis provided a basic understanding of opposed flow flame spread theory that is still used today. The work by McAlevy and Magee [8-11], which was simultaneous with deRis' research, supported advances in flame spread theory experimentally. At the same time, Friedman [12] wrote the first published journal review of flame spread including the experimental and theoretical flame spread findings of that time. Together, these studies provide a foundation of diffusion flame spread that has helped to produce many of the flame spread theories of today.

McAlevy and Magee's work contributed experimental improvements to flame spread theory. They pioneered the use of small wind tunnels, which are now essential in combustion laboratories, to measure flame spread rates in an opposed oxidizer flow configuration. They also were the earliest researchers to take advantage of the constant burning properties of PMMA, which are used in many thick fuel flame spread studies of today. Moreover, McAlevy and Magee's explanations are still used today such as the

need for understanding the flame zone and aerodynamics of the flame as well as the Damkohler number (ratio of characteristic flow time to characteristic chemical reaction time) effects due to heat losses at the flame tip.

In the studies by Sirignano [13-15], a model for flame spread theory was established which included solid fuel heat conduction ahead of the flame and changes in fuel density. His analysis was similar to deRis, however, he produced a double branched flame spread eigenvalue. His contribution was important though because it addressed some of the criticisms of deRis' flame spread theory.

Unlike deRis who used infinite rate chemistry, Fernandez-Pello and Williams [16,17] employed finite rate kinetics in their flame spread model. They also included first, a thorough investigation of the solid phase heat conduction ahead of the flame and second, the gas phase processes. In their analysis of a downward spreading flame, they included the effects of gravity throughout their calculations and solved the mass and momentum gas phase equations. Fernandez-Pello and Williams also utilized one irreversible Arrhenius reaction ($F + \nu O \rightarrow P$) with high activation energy to represent the gas phase combustion, where F is fuel, O is oxidizer, and P is product. Overall, their model was significant in that it directly related flame spread rate to forward solid heat conduction.

Parker [18] and Hirano *et al.* [19, 20] carried out considerable experimental research on flame spread. Parker measured the leading edge flame temperatures in the gas phase, which influenced further work on the gas phase velocity and temperature fields near the flame tip. Hirano *et al.* also took gas phase temperature measurements and

examined the aerodynamic similarities between the flame leading edge and airfoils by investigating a stationary flame.

The first thorough numerical investigation of flame spread was by Frey and T'ien [21]. One strong point in their study was the inclusion of flame burnout a finite distance downstream from the flame tip. They generated a numerical model of steady-state flame spread over a thermally thin fuel in an opposed flow configuration. Their analysis was two-dimensional and contained the elliptic, gas phase energy and species equations including an overall one step chemical reaction and second order finite-rate Arrhenius kinetics. In the unsteady solid phase, a first order pyrolysis reaction was utilized as well as conduction ahead of the flame as a dominant factor affecting the flame spread. They looked at non-dimensional parameter effects on the flame spread, and obtained good qualitative agreement between experiment and the model for the changes of flame spread due to different ambient pressures, oxidizer mass fractions, and opposed velocities. Their results showed a relation between the flame spread rate and Damkohler number. In addition, they were able to produce the low reactivity flame zone even near extinction. This study was important because Frey and T'ien were the first to numerically calculate flame spread extinction limits that until then had not been determined in other gas phase theories.

Around the same time of Frey and T'ien's work, Altenkirch *et al.* [22] experimentally studied the effects of buoyancy on flames spreading down thin solid fuels. They concluded that if the flame was assumed to be adiabatic, then the dimensionless spread rate correlated with the Damkohler number. They also reported that variations in

the buoyant force caused a difference in pressure, which affected flame spread by changing the chemical reacting rate in the flame.

The above references are some of the major studies that established a basis for modern day flame spread theory. A detailed review is given by Wichman [23], which presents the history and progression of opposed flow flame spread theory.

1.4 Diffusion Flame Spread in Microgravity

In the 1970's NASA began major construction on the next phase of the space program, prolonged human space flight in the Space Shuttle. As a result, scientists at NASA and abroad began rigorously studying the effects of microgravity on fire. The driving factor has been to preserve the safety of the astronauts in flight. Microgravity flames are studied onboard the space shuttle and space stations, on airplanes that fly in parabolic arcs (KC-135) and in drop towers where experiments plunge to earth. The drop towers supply between 2 to 10 seconds of microgravity in which the experiment is in free fall, and the airplanes give approximately 20 to 30 seconds of 10^{-2} gravity level conditions. These facilities have provided information to determine conditions and parameter ranges that may yield useful results in space. They also can determine the underlying flame processes that are masked in 1-g by buoyancy.

A very useful study in microgravity flame spread was that of Olson *et al.* [24]. In this research, a flammability map for microgravity flame spread over a thin solid fuel was completed, which showed the effects of relative velocity between the flame and opposed flow and the molar oxygen concentration of the environment around the flame. The study focused on the lower limit of opposed flow velocity called "quenching" in which the flame extinguished due to lack of oxygen. At the opposite branch, called "blowoff",

which was already constructed from previous work, the Damkohler number is large and the flame extinguished because the rate of flow was much larger than the rate of chemical reaction. This study was directly applicable to space flight safety because it showed that the typical small gusts of air on the shuttle (6-10cm/s) can sustain a microgravity diffusion flame.

Bhattacharjee *et al.* [25] produced a theoretical model of a flame spreading over a thin fuel in a quiescent microgravity environment. In this analysis, the steady, two-dimensional gas phase energy, species, and momentum equations were solved along with energy and continuity in the solid phase to obtain a relation for the flame spread rate. Bhattacharjee *et al.* produced a dimensionless spread rate that correlated with the Damkohler number, which agreed with previous studies. They also found that the spread rates increased with increasing molar oxygen concentration in the quiescent environment. Measured and computed rates disagreed, however, suggesting the need to include radiation in the analysis.

Olson [26] further studied the microgravity flame spread map for thin fuels, discussed in [24], by describing three distinct regions of flammability that are controlled by different processes. In the low relative velocity region near the quenching branch, she identified a new flame control mechanism. In this near limit extinction regime, the flame was influenced predominantly by the decrease in oxygen transport due to the increase in thickness of the boundary layers caused by the slow, opposed flow. The boundary layers restricted the convective and diffusive transport of fuel and oxygen to the flame tip. This weakened the flame, placing it closer to the quenching limit, where finite rate kinetics became important.

The study of Bhattacharjee *et al.* [27] compared experimental and theoretical predictions of flame spread rate, and total heat flux from a microgravity flame to the fuel surface. The measurements agreed qualitatively with theory showing the importance of including both surface and gas phase radiation in the model. An examination that exhibited the effects of radiation was performed and showed that the surface radiation decreased the heat flux to the fuel by decreasing the flame temperature, thereby slowing flame spread. Gas phase radiation increased the heat flux to the surface, but was also lost to the environment, which also decreased flame temperature and spread rate. Bhattacharjee *et al.* also showed that as the oxygen concentration is reduced, the heat transfer due to radiation becomes a major factor in the survival of the flame.

In 1993, Altenkirch *et al.* [28], developed a theoretical model and compared results with drop tower and Space Shuttle experiments of a spreading diffusion flame when oxidizer velocity and flame spread were of the same order of magnitude. In this research, radiation was shown to be important at the near extinction limit. The effects of pressure on the gas phase radiation were also shown to be important.

Bhattacharjee *et al.* [29] studied the influences of pressure on a spreading microgravity diffusion flame experimentally and computationally. Their experiments showed that the flame spread rate increased with an increase in ambient pressure. These results agreed with the computational model, which included gas phase radiation. However, the experimental findings did not agree with the model that neglected gas phase radiation, further supporting the inclusion of radiation in microgravity diffusion flames.

1.5 Diffusion Flame Instabilities

This section will review some research on diffusion flame instabilities. It includes experiments in both normal gravity and microgravity. Most of the numerical studies neglect gravity. Many studies have been done on diffusion flame instabilities in normal gravity, however, due to the relatively young age of the Space Shuttle program, research of diffusion flame instabilities in microgravity is limited. In addition, the difficulty of observing microgravity flames near extinction for prolonged time periods has also restricted research. Most of the research presented here was not an examination of flame spread across thermally thin fuels. Only diffusion flames were discussed that displayed some of the same unstable behaviors seen in this thesis. This suggested that the flame instabilities in this study are a fundamental aspect of flame behavior. The candle flame is considered in the next section in more detail since it closely resembles qualitative experimental findings in this thesis. The studies are presented in chronological order to give a sense of the subject development.

In the inverted wick experiments of Blackshear and Murty [30], flame wrinkles were seen when the fuel molecular weight increased. Orloff and deRis [31] attributed a critical Raleigh number for observing cellular instability, which comprised two identical internal rotating cells of fuel vapor located in a vortex.

W. Chan and J. T'ien [32] conducted an experimental study of spontaneous flame oscillations near extinction. In this work, which was inspired by Kirkby and Schmitz [33] and Baliga and T'ien [34], high-speed motion picture and temperature measurements were used to analyze extinction mechanisms for wick, tube, and rod flames in normal gravity. Flame oscillations were local and multi-dimensional, and the unstable behavior

originated near the weakest point of flame stabilization or the vicinity of lowest reactivity. Due to the complexity of multi-dimensional analysis, a simplified explanation for the near limit behavior was proposed. The first explanation discussed an increase in temperature at certain points in the flame, which caused an increase in fuel vaporization. If the already disturbed flame temperature was also a local maximum, then this increase in pyrolysis enhanced the flame oscillations. This placed the flame closer to extinction because it was balancing these processes to survive. The second explanation of Chan and T'ien discussed a reduction in the concentration of the oxidizer causing the flame to quench locally due to locally weak chemical reactions. The reduction of oxygen caused the flame to extinguish, which decreased the temperature, and caused the local induced velocity to decrease. At this point, the flame tried to propagate into the quenched region, so the flame "flashed" which appeared as an oscillation in these flames.

Chao, Law and T'ien [35] numerically studied the structure and extinction attributes of a burning fuel droplet as a characteristic diffusion flame. The interesting finding was that radiative heat loss formed two critical extinction turning points. In particular, smaller sized droplets extinguished due to the decrease in the chemical reactions. For larger sized droplets, the heat loss by radiation promoted extinction and in time also caused limited chemical kinetics.

Cellular structures resulting from instabilities of diffusion slot jet flames in normal gravity were experimentally investigated by Chen *et al.* [36]. The unstable cellular flames were only seen near extinction, and flame behavior was found to be similar to premixed flame instabilities. Cellular structures occurred for Lewis numbers

less than one (~0.8) of the more completely consumed reactant, which agreed with Linan's [37] criterion.

A very comprehensive numerical study was carried out by Kim [38,39] in which he looked at a one-dimensional flame and employed the thermodiffusive instability by utilizing non-unity Lewis numbers. He neglected the hydrodynamic instability, but contrary to other works, he accounted for finite rate chemical kinetics with the thermodiffusive mechanism. In his analysis, a periodic wrinkling of the reaction sheet and striped patterns were seen for flames near extinction.

Cheatham and Matalon [40] conducted an investigation of the instability mechanisms of a burning liquid fuel droplet near extinction by reducing the oxidizer. The motivation of this study was to simulate the microgravity candle flame, which was spherical and showed unstable dynamics due to a decrease in the surrounding oxygen concentration They noticed that reducing the Damkohler number manifested a gradual rather than sudden transition to unstable conditions. Cheatham and Matalon further showed that for the near extinction conditions of these flames when the Damkohler number or oxygen was reduced, radiative heat losses higher than a critical value would produce unstable, oscillatory flames. The flames moved away from the fuel source when the Damkohler number was diminished. The flames, though, tended to return to the undisturbed original location. Oscillatory motion started because radiative heat losses below a critical value further reduced the flame temperature and Damkohler number, which again caused the flame sheet to move outward because of weaker chemical reactions. Oscillations increased in magnitude for large heat loss values or reduced oxidizer values. In time the flame quenched. Standoff distances were approximately 5 to

8mm for oscillation frequencies of order 1Hz, which agreed with microgravity candle flame values.

Matalon [41] numerically researched the onset of the diffusive thermal instability in a non-premixed flame. He discovered that cellular instability occurred for a specific range of Damkohler numbers when there was a loss of reactant from the reaction sheet. Also, cellular instabilities transpired for fuel Lewis numbers less than one, and the calculated cell wavelengths were of the same order as those in experiments.

Olson *et al.* [6] observed finger-like smoldering in experiments performed on the Space Shuttle with thin burning cellulosic fuels. The finger smoldering fronts preferred to move against the oxidizer flow. Normal gravity smoldering experiments did not exhibit fingering, possibly due to the large buoyant flows available to the entire flame front. In microgravity, it was proposed that the very low flow velocities did not permit oxygen to be delivered on the sides of the smolder front. Therefore, smoldering in the front was enhanced, which presented itself as a bulge or finger.

1.6 Candle Flame in Microgravity

The most famous and extensively studied diffusion flame in microgravity is the candle flame because it is a steady, non-propagating, diffusion flame, which is quite uncommon, but relatively easy to study. Microgravity candle flame experiments were conducted on board the Space Shuttle and Mir Space Station, and Dietrich, et al. [4], compared results to a numerical model. Besides steady state behavior and numerical simulation, unsteady flame oscillations near extinction were observed and modeled.

The experiments on the Shuttle were conducted in a glovebox that allowed oxidizer to diffuse into the candle environment. The Mir tests, though, used a container

with screens that allowed more oxygen to diffuse in due to the increase in open surface area. As a result, Mir candle flames lasted longer than Shuttle flames. Flames on both the Shuttle and Mir began as yellow, sooty flames that eventually changed into dim blue hemispherical flames. The blue hemisphere indicated the absence of the buoyancy and the churning motion it causes, which would normally produce a yellow tear drop shape on earth. In microgravity, less fuel vapor and oxygen mix than on earth, so a lower flame temperature and burning rate produce the blue color. The flames burned steadily for time periods ranging from 100sec. to 45min. Before extinction, the candle flames oscillated at frequencies of approximately 1Hz. The oscillations occurred when the base of the flame moved up and down, however, the top of the flame remained stationary. This unsteady behavior continued until the flame extinguished. In the Shuttle experiments, the candle flame extinguished because inward diffusion of surrounding oxygen through the small holes of the glovebox was not sufficient to sustain combustion. However, in the Mir experiments, the longer lasting flames extinguished by fuel consumption. It was also determined that the candle flame can be considered "quasi-steady" because the duration of the flames on Mir was much larger than the gas phase time scales.

The two dimensional axi-symmetric numerical model included finite rate chemistry and radiation effects. The end of the wick was considered to be a small sphere through which fuel evaporated. Numerical reaction rate contours compared well with experimental flame shapes in steady state for different oxygen mass fractions. Model behaviors in the near extinction limit regime were brought about by sudden small decreases in the oxidizer mass fraction, similar to the steady depletion of oxygen during experiments. Oscillations in the model became larger in size until extinction, in which

the amplitude depended on the magnitude of oxidizer reduction. Frequency rates, though, were approximately 0.2Hz., but this increased with decreasing fuel Lewis numbers. The model oscillations agreed qualitatively with the experiment in that the motion of reaction contours was similar, nonetheless, the size of oscillation in the experiment was greater. The microgravity candle flame study is very important because it looks at a diffusion flame without the complex motion of buoyancy in both steady and unsteady states experimentally and numerically.

1.7 Instabilities in Simulated Microgravity Environments

Experiments have been performed in normal gravity in which the gravitational effect was "removed". These types of experiments provide an economical means of looking at flame instabilities in pseudo-microgravity conditions. Coupled with drop tower and in-flight experiments, these simulated results can supplement flame theory that can be applied to characterizing combustion of different materials in space. The second part of this thesis involved the construction of such an apparatus, which produces flame instabilities in a reduced buoyant atmosphere. The following experiments motivated this endeavor.

1.7.1 Low Stretch Flames

In the doctoral thesis of Olson [5], low strain rates ($\sim(g/R)^{1/2}$) yielded a simulation of a microgravity flame. This was achieved by varying curvature (radius) of the burning PMMA cylinders. The diffusion flames broke into smaller cellular flames when the radius of the PMMA was increased beyond a critical limit. The smaller flames, herein denoted as flamelets, wandered across the surface for long periods of time on the order of 10min. Flamelets interacted with each other through their edges pulsating across the dark

non-flaming portions. This dark channel was most likely fuel rich due to the leakage from the flamelets. Prior to extinction, an entire flamelet would oscillate.

1.7.2 Hele-Shaw Apparatus

Hele-Shaw apparatuses, which are wind tunnels where the test section is made of two closely spaced parallel plates, have been typically used to observe inviscid flow patterns [42]. However, flames spreading over thin solid fuels between the two parallel plates in a Hele-Shaw apparatus will break up into smaller unstable fingerlike flames. If the distance between the plates is below a "critical" value, buoyancy is suppressed, thereby simulating a microgravity flame. The critical spacing between the plates can be estimated using the condition that the Raleigh number based on the spacing is greater than or equal to 1708 ($Ra_h \geq 1708$) [43]. The Raleigh number is the product of the Grashof number (ratio of buoyant to viscous forces) and the Prandtl number (ratio of momentum and thermal diffusivities). For spacing that produces Raleigh numbers below 1708, the commonly known *Benard cells* or natural convective flow patterns will not occur. Therefore, the effects of buoyancy may be neglected. The flame depends on diffusion due to the absence of the bulk motion that would mix the fuel and oxidizer. In the recent study by Zik *et al.* [44] a uniform smoldering front over a thin cellulosic fuel in an opposed flow oxidizer situation became unstable and separated into fingers when the incoming oxygen flow was decreased. Further reduction of the oxidizer flow led to splitting where only a few fingers remained and eventually extinguished.

Zik *et al.* calculated that the two length scales, finger width and finger spacing, were affected by the non-dimensional Peclet number (ratio between molecular convection and diffusion). They further evaluated the critical Peclet number when the finger

spacing would be zero (a uniform flame front). From the experiments, Zik *et al.* concluded that the spacing between fingers was determined by the contention of oxygen by adjacent fingers. Therefore, they assumed that the fingering was a form of the thermal diffusive instability mechanism. They also showed that finger width was linearly dependent on the spacing between the parallel plates.

Zik *et al.* and Olson *et al.* [6] showed that fingering instabilities could occur in the form of smoldering in which the reaction is not in the form of a flame and does not appear as the typical yellow color. This instability is difficult to detect and can undergo transition into a flame if oxygen concentration or heat losses are increased. Therefore, it is important to know all of the conditions for their survival since they present a fire hazard onboard the space station.

1.7.3 Microgravity Flame Spread Limits in Hele-Shaw Type Devices

As mentioned earlier, determining the limiting conditions under which combustion fronts will be sustained and propagate over a solid material is a goal of the space agencies. The Russian Space Agency (RSA) conducted an experimental study to predict the worst case scenarios of flames spreading over combustible solids [45]. They based their experimental work on previous investigations that showed a flame extinguished if the oxidizer flow rate was reduced below a critical value in a microgravity environment. Therefore, a method of fighting fires in space could be based on decelerating the fan flow in space station compartments below the critical velocity if combustion occurs. Coupled with this, a systematic selection of the proper materials, which have a favorable limiting oxidizer flow, would also be employed.

The RSA used three different experimental Hele-Shaw type devices that produce microgravity conditions on earth:

1. A narrow horizontal chamber device containing two closely spaced parallel plates, with samples burning on the bottom plate.
2. A vertical chamber device that also suppressed buoyancy by burning cylindrical samples 1mm. away from a cylindrical quartz tube containing the sample.
3. A horizontal chamber device with two closely spaced parallel plates with the burning sample on the upper plate instead of the lower one.

Results from these facilities were compared to data obtained during prolonged space flight onboard the Mir Space Station by using the Skorost facility. The Skorost facility is a combustion flow chamber that allows velocities from 2.5-20cm/s. Three non-metallic fuels were burned. Data from the Skorost mini wind tunnel was used to test the validity of the three ground apparatuses.

The RSA obtained limiting values of oxidizer velocity from all facilities, and suggested that data from ground tests should be taken into account for determining materials for space flight. The RSA concluded that every effort had to be made to decrease the oxygen concentration to the lowest allowable limit because doubling the oxygen concentration lowered the minimum oxidizer velocity that would yield combustion by four to five times. The RSA also concluded that further tests in "space" had to be conducted in order to attain a critical Damkohler number that would aid in defining the combustion region of the materials.

The investigation performed by the RSA demonstrated the difficulty in choosing non-hazardous materials for spaceflight. Currently, the only systematic procedure involves determining the worst case scenario of flame spread on earth. In the future, Hele-Shaw devices coupled with drop tower and other ground-based experiments may prove to be effective components in this process.

CHAPTER 2
EXPERIMENT

2.1 Overview

Experiments were conducted using the "Combustion Tunnel Rig" (CTR) at NASA Glenn Research Center in Cleveland, Ohio, and the "MSU Flame Rig" at Michigan State University in East Lansing, Michigan.

The CTR was a wind tunnel that was dropped in either the 2.2 Second Drop Tower or 5 Second Drop tower at NASA that provide short periods of microgravity conditions. Microgravity flames were produced during the drops, by burning thin fuel samples inside the CTR while low speed oxidizer flowed across the fuel opposite to the flame propagation direction. Videos of the front and side views of the burning sample were taken, and surface thermocouples recorded the temperature of the samples during the drops. Results were analyzed using "TRACKER", an image processing system capable of tracking the flame over time, which led to flame speed measurements. Thermocouple data was reduced using mollification and spline algorithms, which gave temperature measurements over time. These thermocouple results were used for an energy balance at the surface of the fuel sample. The overall use of the CTR in this thesis was to locate the near extinction regimes of the thin fuels that can be difficult to find and perform a preliminary analysis of these experimental results.

The "MSU Flame Rig" is a Hele-Shaw apparatus, which is a wind tunnel where the top plate of the test section was placed at a very close distance to the floor of the test section. Hele-Shaw devices are used to visualize inviscid and irrotational flows in the two dimensional plane parallel to the top plate, which occur due to the viscous flow produced between the sample and top plate. Another aspect of Hele-Shaw apparatuses was that

buoyant flows caused by flames inside the test section were suppressed by the close proximity of the top plate to the bottom of the test section. The MSU Flame Rig utilized this feature of the Hele-Shaw device to produce a simulated microgravity flame near extinction. The near extinction conditions resulted from the low air speeds (1-28cm/s) produced in the test section, which were smaller than characteristic buoyant flows (approximately 30 cm/s). These velocities ensured that the burning samples on the bottom plate did not extinguish due to blowout and that diffusive flow was the main process for mixing of fuel and oxidizer. The samples in the MSU Flame Rig were in the same opposed flow configuration as the CTR, however fuels with different thickness can be accommodated in the MSU Flame Rig. Distances between the sample and top plate varied from 2-10mm. Most of the work in this portion of the thesis was devoted to the successful design and fabrication of a device that burned thin samples that exhibited near extinction limit behavior. Future results from this device will aid in the selection of thick fuels that will fly on the International Space Station (ISS), help to determine the maximum sample width, and allow more time to qualitatively study flame instability.

2.2 NASA Combustion Tunnel Rig

2.2.1 NASA Samples

A schematic of the experimental setup used in the CTR is shown in Figure 2. The cellulosic, thin, solid fuel used was Kimberly Clark[1] brand Kimwipes 10.5cm. in width and less than 10^{-4}in. thick A Kanthal[1] brand hotwire that was formed into many sinusoidal curves ignited the sample. The sample was held straight and taut by gluing it

[1] Trade names or manufacturer's names are used in this report for identification purposes only. This usage does not constitute an official endorsement, either expressed or implied, by Michigan State University or the National Aeronautics and Space Administration.

to the outer edges of the sample holder frame, which was either an aluminum (conducting) holder or a polymeric (insulating) holder.

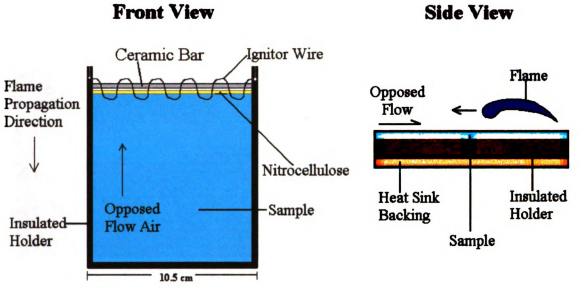

Figure 2. NASA sample front and side schematic.

Thicker fuels generated slower spread rates than thin fuels. A fuel was considered thermally thin if conduction into the thickness of the fuel (perpendicular to the flow and spread in Figure 2 side view) was negligible. In other words, the sample was not so thick that it acted as a heat sink draining the flame of its energy because gradients of temperature across the thickness were infinitesimal $\{(\Delta T_{\text{sample thickness}}/\Delta T_{\text{characteristic}})<<1\}$. Thermally thin, cellulosic Kimwipes were chosen because the spread rates were fast enough for flames to show unstable behavior during the 2.2sec. and 5sec. drop periods.

Samples were ignited in normal gravity and then dropped after a one-dimensional flat flame front was established like the one shown in Figure 3a. It was important that the

flame front was linear as opposed to a parabolic flame shape that lags near the sides of the sample holder, like the one shown in Figure 3b. This is because for a parabolic flame front, the flame instabilities might be attributed to edge effects instead of inherent flame dynamics.

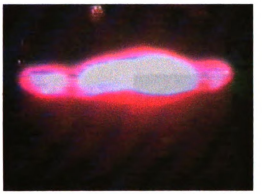

Figure 3a. Flat, linear flame front in 1-g.

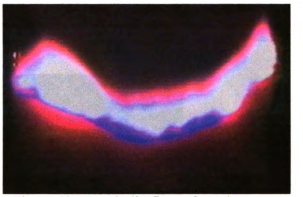

Figure 3b. Parabolic flame front in 1-g.

Several conditions assured the generation of a flat spreading flame front. The wire was woven into dense sinusoids, so that better contact between the fuel and wire was achieved. Thus, uniform ignition across the entire sample was more likely instead of patches of flames travelling down the sample. An alumina ceramic bar held the igniter in place, so that the wire would not sag when heated and cause a parabolic flame front that trailed at the sides. Also, a thin strip of nitrocellulose was glued across the top of the sample that served as an extra source of initial heat generation for ignition. The thermal expansion caused by exothermic heat release by the nitrocellulose did not complicate the problem, since its effects were washed away by the opposed flow before the drop commenced. Lastly, the metal holder used in the beginning of testing was replaced with

an insulating holder because it caused the flame front to be parabolic as it conducted too much heat away at the sides of the flame.

It was clear that the samples had to be ignited in normal gravity and then dropped because it was nearly impossible to produce a flat flame in the near extinction regime during the 2.2sec. or 5sec. drop time. If a front like the one shown in Figure 3a occurred, the rig was dropped in the drop tower, and the flame underwent transition into a flat, linear microgravity flame front. An example is shown in Figure 4. Hence, if a flame as in

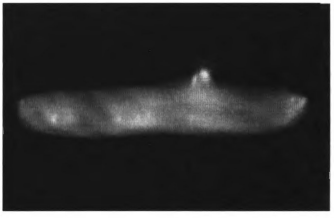

Figure 4. Flat, linear flame front in microgravity.

Figure 4 later corrugated, produced flamelets, and progressed to near extinction, it was not because of influences at the sides of the sample near the holder.

2.2.2 NASA Test Conditions and Flow System

As stated previously, a flame in low gravity will enter into the near limit regime and extinguish if one of the major components for flame survival (fuel, oxidizer, or heat) is reduced below a critical level. In the beginning of testing, the concentration of oxygen was reduced to 17-18% in order to reach near limit behavior. Since it was difficult to produce a uniform flat flame front in normal gravity at such low oxygen percents, it was

obvious that a uniform flame would not occur in low gravity. Hence, instead of lowering the oxidizer mass fraction, a metal or insulator backing that served as a heat sink was placed a finite distance away from the sample. The backing provided a means with which to vary the heat loss in the tests, so that the near extinction limit could be attained while burning in air. This is best illustrated by observing the flammability map of Olson [24, 26] in Figure 5. In both normal gravity and microgravity, the burning sample was in

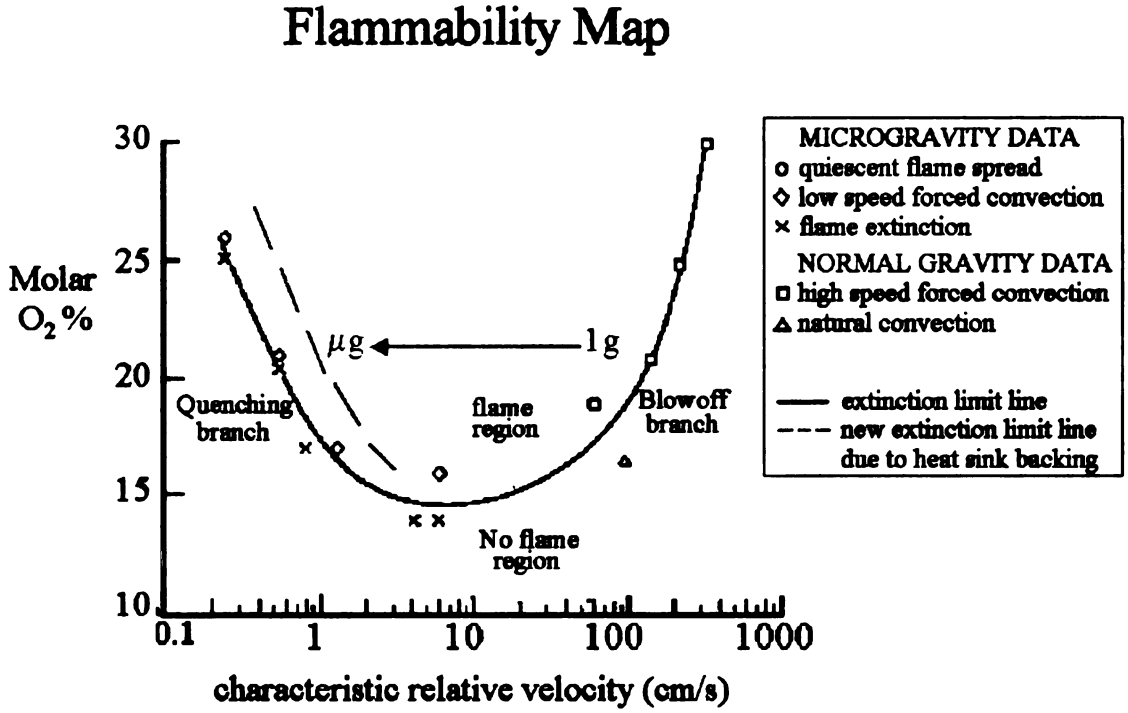

Figure 5. Flammability Map of Olson [24, 26] with new extinction limit branch.

the flame regime. For each drop, the flame followed the green line from normal gravity to microgravity. If conditions were favorable (low oxidizer flows or low characteristic relative velocities), the sample would reach the near extinction limit in microgravity, which corresponded to the quenching branch on the left. However, by employing the heat sink backing, the quenching branch was in effect moved up and to the right as shown

by the portion of the red dashed line. This new displaced quenching branch enabled higher oxygen concentration conditions such as air to be used. In summary, air was preferable because steady downward spread in normal gravity was easily established prior to each drop, and the backing (not the low oxygen concentration) enhanced transition to instability when the drop occurred.

Care was taken to prevent the sample and backing from touching in order to avoid heat conduction changing the fundamental processes of the burning sample, even though it is considered a thermally thin fuel. At close distances around 5mm., the backing quenched the flame that would have otherwise existed on the sample back side (if there were no backing, two symmetric flames would spread across opposite sides of the sample).

Air velocities with uniform profiles from 1-8cm/s were produced in the test section that contained the sample. A schematic and picture of the flow system on board the CTR are shown in Figures 6a and 6b. The tunnel reservoir stored up to 1800psia of gas mixtures that contained less than 50% of O_2. The reservoir had to be filled before each drop, so it would not entirely drain to zero gage pressure. This was especially important for tests that required high velocities since the reservoir pressure decreased more quickly than at low speeds. Instructions for filling the rig reservoir with air at NASA are found in the Combustion Tunnel Rig (CTR) User's Guide [46]. The pressure regulator was adjusted to set the velocity in the test section, while the calibrated critical flow nozzle controlled the flow and provided choked flow velocities above 2cm/s in the test section. Mass flow rates downstream of the orifice remained choked as long as the upstream pressure was twice as high as the downstream pressure. Calibrations of the

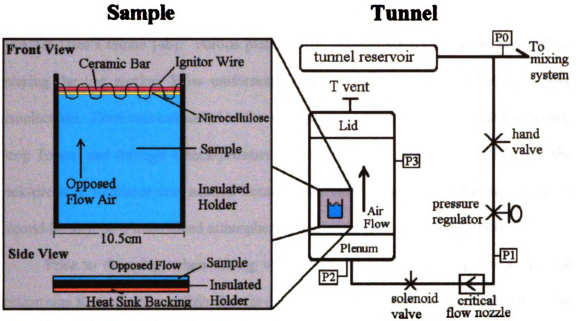

Figure 6a. Schematic of flow system in Combustion Tunnel Rig.

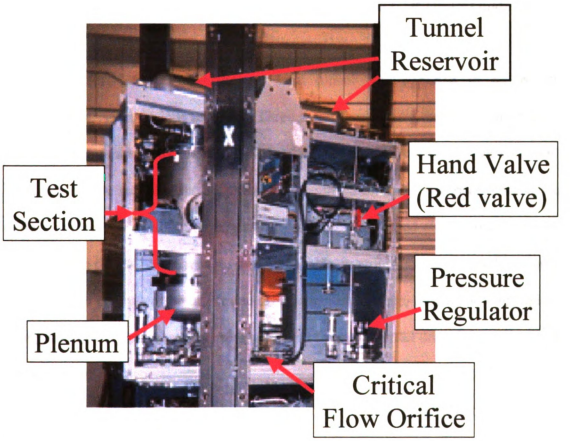

Figure 6b. Picture of flow system in Combustion Tunnel Rig.

critical flow orifice were performed at NASA Glenn Research Center and can be found in the CTR User's Guide [46]. Porous plates in the plenum straightened the flow before entering the test section. Flow uniformity in the test section was verified by smoke visualization. Flow was exhausted to the atmosphere through a T-vent in the 2.2 Second Drop Tower, and through a back-pressure regulator in the 5 Second Drop Tower. The back-pressure regulator was needed because rigs were dropped in a vacuum in the 5 Second facility, so it maintained atmospheric pressure in the tunnel test section.

Prior to dropping, when the rig was secured at top of the drop tower, the test section was flushed with oxidizer flow in order to establish uniform flow conditions. The amount of time for filling the test section varied with flow magnitude, so for higher flow rates less time was needed. The flush times are located in the CTR User's Guide [46].

2.2.3 NASA Rig Electrical System and Diagnostics

The CRT was a self-sufficient wind tunnel that operated in an isolated environment for short periods of time. Three batteries on board the rig supplied power to the electrical components. A model IV Tattletale Control System along with TTOOLS computer software recorded the drop data and regulated different electrical processes on the rig. Software programs that controlled data acquisition and rig electrical switches were written in the BASIC language. Before each drop, programs were loaded and stored in the on board computer, which ran the drop sequence. Hence, turning flow on and off, igniting the sample and other processes necessary for a successful drop did not have to be done manually.

Several digital and analog channels permitted certain diagnostics on the rig. Four pressure transducers at various points on the rig tabulated the pressure versus time for

each drop. These measurements were also needed for filling the rig reservoir with oxidizer and setting the flow rate. Therefore, the velocity through the test section was monitored when filling and throughout the drop. Three portholes around the test section chamber allowed video cameras or 16mm. color film cameras for visualizing the front, back, or side view of the tests. In this project, video cameras recorded the front and side views of the burning sample. Type K thermocouples were incorporated into the rig diagnostics. Up to three thermocouples recorded the temperature at the sample surface, and either side of the heat sink backing. The temperature was measured at time intervals that could be preset by the CTR user. Thermocouples were sewn into the sample, so the bead had thermal-physical contact with the fuel surface. The location of the thermocouple on the sample was marked, so it could be seen on the video recording during the real time of the drop. Since the researcher conducting the tests indicated to the tunnel operator when to drop, this marker was essential to obtain the correct drop timing. In this way, the researcher could determine when to drop the rig, so that the flame would spread over the thermocouple when it was in microgravity. Hence, it was assured that the surface temperature of the microgravity flame was measured regardless whether the flame or flamelet was stable or unstable. In other words, it was not known prior to the drop where along the flame front breakup would occur. Consequently, it was not completely certain beforehand whether the thermocouple would measure the temperature of the flame front, flamelet, or the dead space between flamelets. Besides sample surface measurements, substrate temperatures were recorded by gluing a thermocouple on the front side of the backing for good contact.

2.2.4 NASA Drop Tower Facilities

NASA Glenn Research Center has two microgravity drop towers, a 2.2 Second Drop Tower and 5 Second Drop Tower. The 2.2 Second Drop Tower has been used to obtain preliminary data. This was because the turnover time was much faster, so as many as 3 drops per day were conducted. Therefore, a large amount of information was obtained in a smaller time period. The 5 Second Drop Tower is used for experiments that are further along in their experimental programs. However, scientists have gained information in the 2.2 Second Drop Tower that was sufficient for their research.

Drop towers produce short periods of near zero gravity environments. The following theory behind this is explained by considering the forces on objects located on earth and in its vicinity. The ground provides a feeling of weight because of the reactionary force that it exerts. When a person is falling toward the earth, though, there is no feeling of their weight, hence they experience "weightlessness". This condition is called "free fall" or "zero gravity". All objects falling towards earth experience the same acceleration ($g=9.8m/s^2$) in the absence of air resistance. Any object that moves freely under the control of gravity regardless of initial conditions is said to be in a state of "free fall".

There are two ways to achieve zero gravity. The first is to travel far enough away from the earth's surface, so that the force of gravity has no effect. This originates from Newton's equation of the force of attraction between two bodies of mass m_1 and m_2:

$$F = G\frac{m_1 m_2}{r^2} \qquad (3)$$

In Equation 3, G is the gravitational force and r is the distance between the two particles. Therefore, if the distance between the mass (m_1) and the earth (m_2) is very large

($r^2 >> Gm_1m_2$) then the force between the two objects will be close to zero. If this is applied to a person and the earth, then in order for the object to feel zero force or zero gravity, the person would have to travel a distance far from the earth.

The second and more utilized way of achieving microgravity or freefall was first explained in a thought experiment by Sir Isaac Newton. If a cannon is placed at the top of a very high mountain and fired, the cannonball will travel along a parabolic trajectory and eventually hit the earth. However, if the cannonball is fired with a large amount of energy, it will reach a point where it will not return to the ground. In this state, the cannonball is continuously falling not toward earth but *around* it. This condition of continuous freefall is called orbit, in which the object never reaches the surface of the earth. This is how astronauts feel weightlessness in space. The space shuttle travels with sufficient speed to reach earth's orbit, in which the astronauts and all objects in the shuttle fall together around the earth.

The drop tower facilities use the same principles to produce microgravity. The experiments eventually hit ground, though, so the time of microgravity is not continuous like in orbit, but much shorter. CTR experiments were placed in a capsule, which was analogous to the space shuttle because they shielded the objects inside from the drag. In this way, the objects inside the capsule floated (or dropped) at the same acceleration, thus producing microgravity or weightlessness. Taller drop towers produce longer periods of microgravity.

The smaller of the two drop towers at NASA produces 2.2 sec. of 10^{-4} gravity levels. A schematic of the tower is shown in Figure 7. Experiments in this tower fell

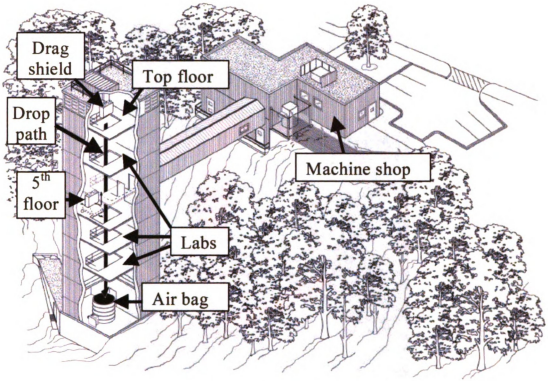

Figure 7. 2.2 Second Drop Tower schematic.

from the top floor below which there were various labs where researchers prepared experiments and staff members built rigs and operated the tower for drops.

A picture of a typical drag shield in the 2.2 Second Tower is shown in Figure 8. Each experiment was placed inside the drag shield on the fifth floor. The drag shields in this tower had a high weight to frontal area ratio, so drag coefficients were low. Drag shields were up to 101.6cm. in height, 96.5cm. in width, and up to 158kg. (350lbs.) of weight. The drag shield that contained the CTR experimental rig was lifted to the top of the tower. After the CTR rig diagnostics and other parameters for the experiment were prepared, the rig was dropped. The rig freely fell 20cm. within the drag shield, while the entire drag shield and experiment fell 24.1m. into a 10ft. airbag. The entire experimental

Figure 8. Drag shield in 2.2 Second Drop Tower.

package endured gravity levels between 15g. and 30g. upon deceleration.

A schematic of the five second drop or "Zero-G Tower" is shown in Figure 9. The "Zero-Gravity Research Facility" was much more complex than the 2.2 Second Tower because the size of the tower, which was actually a 155m. shaft into the ground, was approximately as high as the Washington Monument. Another intricate feature of the tower was that before each drop, the shaft was pumped to a vacuum. A larger staff than in the 2.2 Second Tower was required to operate the vacuum hydraulic system. The entire process usually lasted 45min. on a dry day and more than 1 ½hr. on humid days. The vacuum was necessary because air drag would slow the acceleration of the capsule

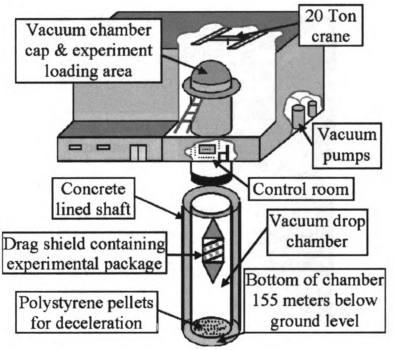

Figure 9. Zero-G or 5 Second Drop Tower facility.

containing the experiment if it dropped 155m. in atmosphere. A large 20ton crane hoisted the experiment that was no more than 455kg. (1003lbs.) at the top of the tower.

The experiment was again placed in an experimental capsule, which were cylindrical and measured up to 3.4m. in length and 1m. in diameter. A typical test where a capsule is being hoisted to the top of the tower is shown in Figure 10. These large enclosed containers were needed to accommodate all of the electrical components that operated the rig during the drop. There were no connections from the rig to the tower once the experiment was dropped. When the capsule was at the top of the tower and sealed from atmosphere, an umbilical cable, connected to the top of the capsule, provided electrical power and communication to and from the experiment before the drop. Seconds

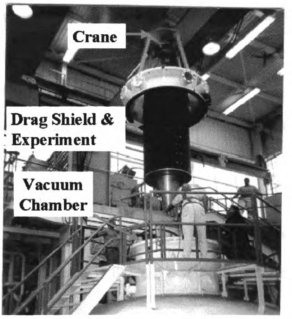

Figure 10. Drag shield in the Zero-G Drop Tower.

before the drop, pins holding the capsule were removed, so that the capsule was hanging from a support shaft less than 1in. in diameter. A pneumatically controlled piston hit the support shaft, shearing it and dropping the capsule. Therefore, a drop from rest was achieved. During the drop, the electrical system, which contained video recorders and all other electrical components, gathered and stored the data. Gravity levels during the drop were 10^{-5}g., producing 5.18sec. of microgravity.

At the bottom of the tower, the capsule decelerated in a pool of polystyrene pellets. The radius of the cylindrical pool was larger than the capsule by inches. Therefore, it was the viscous resistance of the polystyrene that slowed the capsule to a halt. Within this 150millisec., the capsule deceleration was a ramp function during which it experienced from 0g to 65g's.

Due to the time to prepare for a drop in the Zero-Gravity Facility, no more than 2 drops per day were performed. Consequently, many researchers use this facility in the final experimental stages of their projects.

2.2.5 NASA Rig Test Procedure

In this section, an overall procedure is presented in order to give a notion of the steps involved in conducting the drop tower experiments in this project. The following steps illustrate the procedure that was followed to accomplish a drop. Since then, improvements of the test method have been made. In particular, the nitrocellulose is no longer used, and the igniter system is like the one that will be explained on the MSU Flame Rig.

Sample Preparation

- Glue nitrocellulose on cellulose fuel and glue sample to sample holder.
- Form igniter wire, attach to wire leads, and weave sample through it.
- Thread thermocouple in sample, mark it, and attach thermocouple to leads.
- Screw backing into place with thermocouple on front surface near sample.
- Place sample holder in rig so it is secure and immobile.
- Connect thermocouples leads to female ends at top of chamber. Make sure to note which thermocouples correspond to their respective channels.
- Place top on test section and secure in place.

Flow

- Fill rig reservoir with no more than 1800psia of gas (air, O_2-N_2 mixture) (See CTR User's Guide [46] for complete procedure of this step).

- Set flow velocity in test section by adjusting the pressure regulator to the desired flow. CTR User's Guide contains velocity and pressure calibrations for this step. (Complete procedure of this step is in CTR User's Guide [46]).
- Make sure solenoid valve is off.
- Cap T vent at top of chamber if leaving overnight.

Electrical Components

- Set igniter wire current to proper value, so that the wire will not break. Calibrations for this step are in CTR User's Guide. Igniter current controller (ICC) is on side of the test section chamber, and switch must be flipped to "set" position. Also, igniter switch on Power Control Box (PCB) must be in the "on" position. Make sure to switch ICC back to operate when finished. (See CTR User's Guide [46]).
- Check focus of video cameras by connecting to VCR and viewing on TV. Reconnect cables to PCB.
- Charge batteries with power box while the batteries are off.
- On PCB make sure of the following: (See CTR User's Guide)

  3 Batteries are ON.

  Igniter switches are OFF.

  Manual Enable, Video Power, Aux 2, Tattletale Computer are ON.
- Take caps off T vent.

Drop Procedure

- Bring rig to 5th floor and proceed with drag-shield packaging procedures. Tunnel operator will help with this.

- Connect fiber-optic cables that will transmit video data to VCR's. Make sure there are no tangles since fiber-optic cables damage easily.
- Go to 8th floor where rig will be hoisted.
- Insert video tapes and record drop number for reference. Set videos to proper channels.
- Make sure red, green, and yellow switches on control panel are in off position. This is very important since these control the flow and igniter switches.
- Open side of drag shield and connect computer cable to laptop computer.
- Connect three cables at top of rig with the leads and alligator clips to either a red, green, or yellow circuit. Make sure the two far cables have the same color code, which means they are part of the same circuit. The third cable will indicate when the rig is dropped.
- Turn ON batteries and laptop computer.
- Go to TTOOLS on computer and at the prompt load in proper program, which corresponds to drop tower. Type run, then answer questions including flow flush times, and unplug computer cable. Close drag shield.
- Press play and record on VCR's and announce the drop.
- Flip gas solenoid circuit switch on control panel. This will start flow flushing into chamber for a proper period of time before the igniter will automatically turn on.
- While viewing video screen, decide when a flat flame front has developed before reaching the thermocouple, and say "DROP".

Post Drop Procedures

- Collect Tapes and proceed to 5th floor to remove drag shield.

- Bring rig to sample preparation area and connect computer cable and battery cables.
- Open TTOOLS and type run to download pressure and thermocouple drop data.
- Record drop data in blue log book, review drop tapes, and save drop file data

2.3 MSU Flame Rig

2.3.1 MSU Flame Rig Materials

A picture of the MSU Flame Rig is shown in Figure 11. All materials for this experimental apparatus were chosen with safety in mind. Over 90% of the materials were either non-flammable or had very high ignition temperatures. The very few flammable materials were placed at locations where flames from the tests could not possibly ignite them. The plenum was constructed of aluminum plates, and the

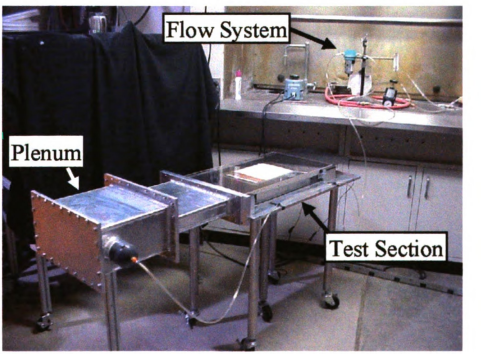

Figure 11. Picture of MSU Flame Rig.

contraction was a steel duct. The plenum also contained an aluminum pipe inside through which the air entered. The porous plate inside the aluminum holder was fabricated from stainless steel. The supporting plate and stilts of the test section were aluminum. All spacers, which adjusted the height of the sample in the test section, were made of either ground steel stock, aluminum bars, or steel shims. The sample tray was aluminum with a mica piece to which the sample was glued. Pyrex windows, which never experienced direct flame, formed the side walls of the test section. A fused quartz plate used to view the flame was the only material that experienced direct flame. However, it was the purest form of glass that could be used having an operating temperature (1250°C) and softening temperature range (1500-1680°C) well above the temperatures of the flames in the MSU Flame Rig. The plenum, contraction, and porous plate holder were sealed using O-rings. Due to the difficulty of removing the quartz plate after testing and not allowing any stresses on it, a soft, removable putty was used to seal the test section, but it never came in close contact to the flames.

A safe and durable flow system was also constructed. Since the flow source produced shop air at 95-110psig, all flow components used were rated to pressures well above any operating values. Polyurethane tubing rated to 150psig connected all of the components.

2.3.2 MSU Flame Rig Flow Control and Measurement

A photo and a block diagram of the MSU Flame Rig flow system are shown in Figures 12a and 12b. Oxidizer was supplied to a nozzle from the in-line shop air in the Engineering Research Complex at between 95psig and 110psig. The red arrows

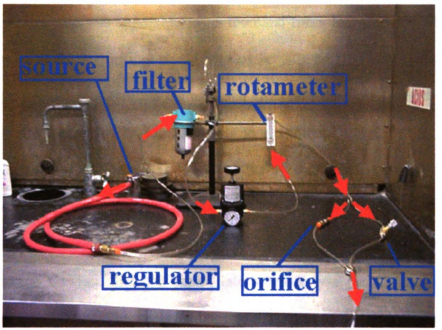

Figure 12a. Picture of MSU Flame Rig flow system.

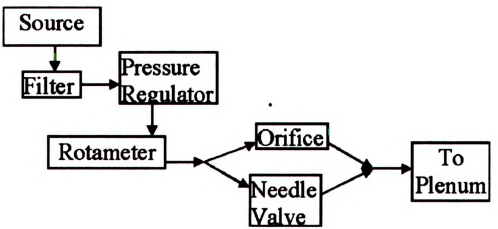

Figure 12b. Block diagram of MSU Flame Rig flow system.

represent the air flow direction. The air flowed through a 5micron filter, which was chosen because its size was approximately a thousand times less than any of the sonic orifices. Therefore the tiny orifices would not clog because nothing larger than 1/1000 of the orifice size would pass through them. After the filter, the flow entered a pressure regulator that was used to set the flow rate in the sonic orifices.

The flowmeter was placed directly after the pressure regulator to determine the test section flowrate and velocity. Since the flowmeter was actually a rotameter calibrated at standard conditions (70°F and 14.7psig) with a range of 5-50scfh, it read a lower volumetric flowrate then the actual rate when it was placed in line and not exhausting to atmosphere. This occurred because the density was substantially higher at in-line pressures, so the volumetric flowrate was lower for the same mass flowrate, since volumetric flowrate equals mass flowrate divided by the density. The actual volumetric flowrate was obtained using a correction factor, which will be explained in more detail in Chapter 3 of this thesis.

After the rotameter, the flow line split with a needle valve on one side and a critical flow orifice on the other side. The needle valve was used to provide a surge of air at the beginning of tests to establish a uniform flame front. At this point in the test, the flow traveled predominantly through the needle valve because the diameter of the critical flow orifice was hundreds of times smaller than the needle valve diameter. In other words, the critical orifice appeared as a closed port to the flow, so it preferred to go through the needle valve. When a uniform flame front like the one in Figure 13a was established, the needle valve was closed at a constant rate until either the needle valve was barely open or the needle valve was closed and air flowed only through the critical

flow orifice. This was one of the main factors that produced a corrugated flame front like the one in Figure 13b. The corrugated flame front eventually led to flame instabilities.

Figure 13a. Uniform, flat flame front in MSU Flame Rig.

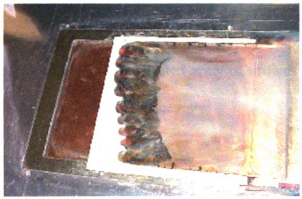

Figure 13b. Corrugated, unstable flame front in MSU Flame Rig.

The critical flow orifices were used to produce the low mass flowrates at which flame instabilities occurred. The orifices were required because they allowed extreme control of flow on the order of centimeters per second because the flow reached sonic velocity at the throat. When the air flowed only through the orifices and not the needle valve, the pressure regulator was used to control the flow in the test section. However, to

ensure sonic flow in the throat and consequently be certain of the mass flowrate, the compressed flow relation in Equation 4 had to be satisfied.

$$P_2 / P_1 \leq .528 \qquad (4)$$

Here P_1 is the back-pressure or pressure of the regulator and P_2 is the downstream pressure. If the back-pressure is higher than approximately twice the downstream pressure, then the flow is choked at the nozzle throat. However, different flowrates in the test section were achieved by setting the back-pressure at values higher than twice the downstream pressure. In these cases, the flow was still sonic at the throat, but the mass flowrate at the throat changed because the density varied due to the different pressure in the nozzle throat. One engineering setback of the nozzles, however, was that the ranges of flowrates for each nozzle were quite small, so the needle valve was utilized in conjunction with them. Otherwise a complicated array of orifices would be necessary, and calibrations for these systems are often inaccurate.

2.3.3 MSU Flame Rig Plenum and Contraction

The critical flow orifice and needle valve were in two separate lines in parallel. After the air flowed through them, the two lines joined to form one flow path again. This flow entered a 2in. diameter pipe that had three rows of 1/8in. diameter holes facing the back of the plenum (see Figure 14). The size of the small holes was chosen to be substantially less than the diameter of the pipe so that the flow entered the plenum through all of the pipe holes. In this way, the pipe appeared as a large plenum to the

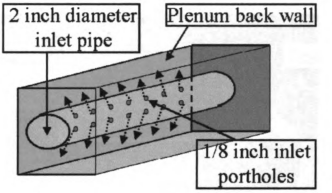

Figure 14. MSU Flame Rig plenum schematic.

smaller holes. If the small holes were close to the size of the pipe diameter, then the air may have only entered the plenum through the first few holes of the pipe, thus producing an irregular downstream flow. The small holes in the pipe faced to the back wall of the plenum to dissipate some of the entry flow kinetic energy, so any individual jets of air were less likely to affect the downstream flow. The size of the plenum (1ft. x 13in. x 6in.) was larger than the test section to create a region with lower velocities than those in the test section.

After the plenum, the 1ft. long by 13in. wide aluminum duct shown in Figure 15 contracted the flow to the 2.3in. height of the entire test section. The contraction contained a ramp that constricted the flow the cross sectional area of the test section.

Both the plenum and contraction were welded along the side seams to prevent any gas leakage. One-quarter inch plates with the duct openings in the middle were welded to the ends of the plenum and contraction. These plates made it possible to facilitate grooves for O-ring seals. The entire apparatus was constructed in separate pieces to enable future additions or adjustments without reproducing the entire device.

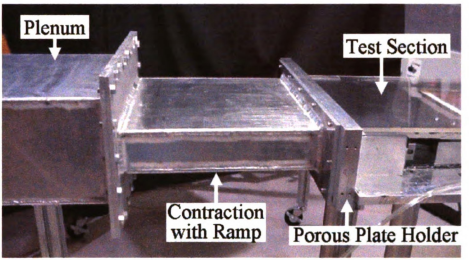

Figure 15. MSU Flame Rig contraction in flow system.

2.3.4 MSU Flame Rig Porous Plate

The purpose of the porous plate was to ensure laminar test section flow. In the MSU Flame Rig, the .062in. stainless steel porous plates had a pore size of either 5microns or 10microns. In practice, the porous plate was the equivalent of many screens, which in other experiments have been used to generate straight and uniform flow. In the MSU Flame Rig, the porous plate, shown in Figure 16, created "uniform" flow by making each flow particle follow a tortuous path. In essence, the porous plate was a large resistance that caused the upstream velocity distribution to "spread" out into a uniform profile downstream.

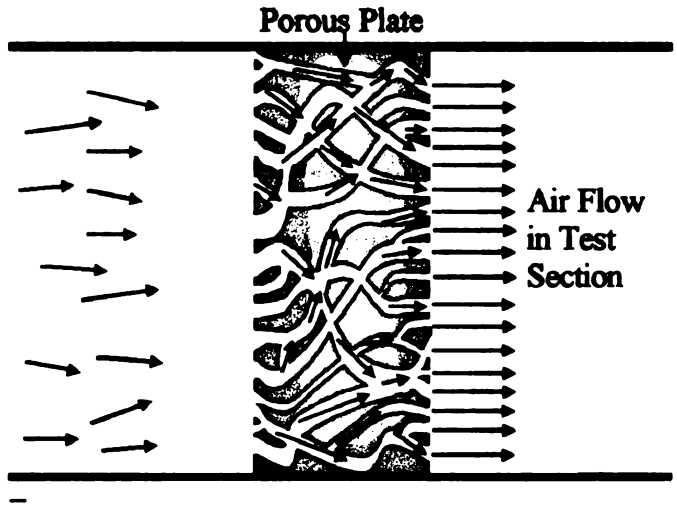

Figure 16. Air path through porous plate in MSU Flame Rig.

Since the plate had very small pores, the effect of the plate was to cause the flow lines to extend evenly over the entire face of the plate. Another way to describe this uses energy balances. When the flow travels through the plate, much of the kinetic energy (due to velocity) is converted to heat energy due to the large viscous forces in the plate. Therefore, mechanical energy from the flow is dissipated, causing the velocity distribution to become everywhere even. This was shown by Baines *et al.* [47] who compared experimental velocity distributions of air through screens with Prandtl's theoretical expression for velocity modification [48], shown in Equation 5.

$$\frac{V_d}{V_u} - 1 = \frac{1}{k+1}\left(\frac{V_u}{V_o} - 1\right) \qquad (5)$$

Here k is the pressure drop coefficient ($k=\Delta P/(\rho V^2_o/2)$), V_o is the mean velocity in the free stream far from the porous plate, V_u is the velocity upstream of the plate, and V_d is the velocity downstream of the plate. Equation 5 illustrates that the downstream velocity depends highly on k, a measure of the energy change through the screen. Baines *et al.*

found that screens with very small pores created an even downstream velocity distribution.

A ramp shown in Figure 17 was placed on the upstream side of the porous plate, so the flow was gradually guided into the porous plate. The ramp was connected to the

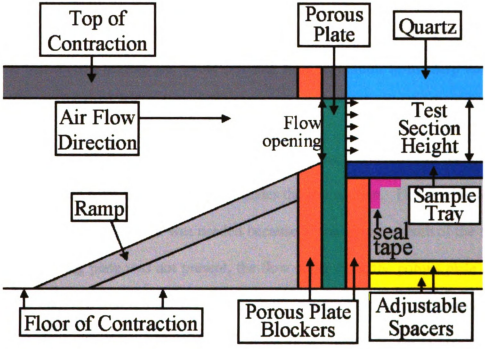

Figure 17. Double blocking plate system for porous plate in MSU Flame Rig.

upstream "porous plate blocker" (first blocker plate on upstream side of porous plate). The ramp and porous plate blocker prevented mass flow from being lost underneath the test section. If the air was allowed to travel through the porous plate in the space below the flow opening, it would be nearly impossible to calculate correct flowrates using the methods described earlier because the flowrates were calculated using the dimensions of the test section. If the dimensions of the test section and spaces underneath were used, only a very approximate estimate based on the area ratios of the two paths could be

determined at best. The ramp was sealed at the base and along the sides of the contraction using duct tape. The ramp also directed the flow gradually into the porous plate, to prohibit separation in the contraction before the first porous plate blocker. The longest ramp possible was used so that the upstream cross sectional area changed slowly. The ramp was connected to the first porous plate blocker on the upstream side of the porous plate. Three different upstream porous plate blockers were fabricated. Each plate had a different test section height of 3mm., 6mm., and 9mm., so the plate openings would match the test section heights and avoid possible flow separation from sharp corners or steps.

On the downstream side of the porous plate was another aluminum plate to block the flow that would have otherwise entered under the test section. This double blocking plate system shown in Figure 17 was needed because of the torturous path of the flow. If the second blocking plate was not present, the flow could enter the porous plate through the flow opening and exit the porous plate near the bottom of it near the spacers. Three aluminum plates were fabricated in order to allow an opening that was equivalent to the test section area, to avoid separation due to changes in flow area. The three plates were made so that the sample tray rested on top of each one and produced the correct test section height. In this way, there was no abrupt step down into the test section from the porous plate. Before placing the aluminum tray in the test section, a piece of duct tape shown in Figure 17, labeled "seal tape", was attached to the sample tray and downstream blocker plate. This prevented air from escaping below the test section, sealing it to obtain proper flowrates. Duct tape was believed sufficient on this low-pressure side. The side edges and bottom of the plates were secured and sealed with putty.

2.3.5 Flow in the MSU Flame Rig Test Section

The flow in the test section was highly viscous because the top plate was very close to the sample. It was therefore concluded that the fully developed test section flow was the commonly known Poiseuille flow in which the flow formed a parabola of constant negative curvature. Furthermore the Reynolds numbers in the test section were computed to be very low in the laminar regime between 1.3 and 300, which can support Poiseuille flow. More of flow in the test section will be discussed in Chapter 3.

The air and combustion products were expelled to atmospheric conditions in a large exhaust plenum connected to the hood, shown in the schematic in Figure 18. The

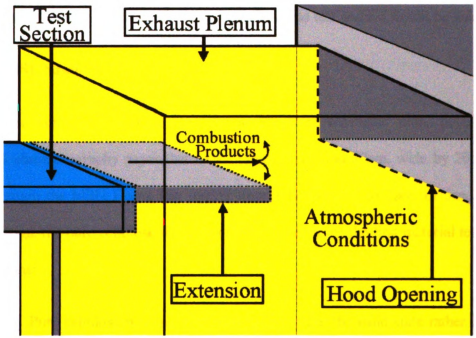

Figure 18. Schematic of MSU Flame Rig exhaust.

dotted lines indicate parts of the system inside the exhaust plenum. The test section was extended to prevent any downstream disturbances from altering test section. The

extension was located inside the large plenum, so the researcher did not inhale combustion products. In addition, the pressure in the test section was estimated to be atmospheric because the hood fan was off during testing.

After testing, the hood fan was turned on to dispose fumes, so velocities in the test section during experiments were unaffected. If the fan were running during testing, then it would have created a lower pressure and higher velocity in the test section than conditions in which the system exhausted to atmosphere. In other words, the fan would have added more of a pressure drop since there is a gain in energy across the fan. Since the fan would have drawn the air and combustion products, the velocity in the test section could not have been calculated, with the fan operating during tests, using mass conservation because the unsteady mass flowrate in the test section would be unknown.

2.3.6 MSU Samples

The samples used in the MSU Flame Rig were Whatman[2] brand pure cellulose Grade 1 chromatography paper that were .18mm. thick and 20cm. wide by 20cm. long. Even though the MSU Flame Rig testing time is not limited to 2sec. or 5sec. like the NASA Rigs, the pure cellulose filter paper was chosen to be the first material tested for a few reasons:

1) Pure cellulose was more likely to gasify from the solid state rather than melt before it pyrolyzed. This was less complicated to study because fuels that

[2]Trade names or manufacturer's names are used in this report for identification purposes only. This usage does not constitute an official endorsement, either expressed or implied, by Michigan State University or the National Aeronautics and Space Administration.

melt often undergo phase change (gasification, bubbles) within the melted material.

2) Thin fuels on the order of paper thickness were considered thermally thin, which meant that the thickness and thus one dimension of the fuel were neglected.

3) A comparison between the NASA tests, which only utilized thermally thin fuels, and MSU Flame Rig tests was desired. However, chromatography paper was chosen over kimwipes because:

    a) It was a research grade material, so many of its properties were known.

    b) Even though the chromatography paper was considered thermally thin, it was thicker than kimwipes. Therefore, the flame speeds were slower than in the drop towers, and instabilities were observed for longer time periods.

2.3.7 MSU Flame Rig Sample Holder and Substrate

The sample holder shown in Figure 19 consisted of a piece of mica and copper backing attached to an aluminum frame, which was attached to a large, aluminum plate forming the floor of the test section. To ensure no obstacles were in the flow, producing separation and unfavorable flow patterns, the sample was glued to the mica, so that it was flush with the aluminum tray. The mica served as an insulator in the same manner as the

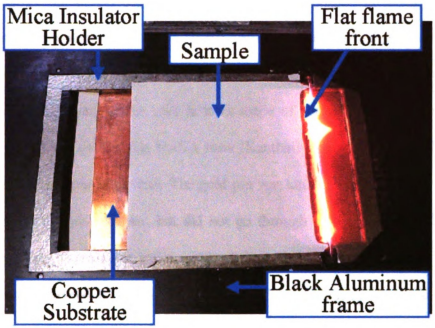

Figure 19. MSU Flame Rig sample holder system.

insulator holder of the NASA Combustion Rig in Section 2.2.1. Like the NASA holder, the mica did not drain heat at the sides of the flame, helping to produce a flat, linear flame front. Like the NASA Combustion Rig, the MSU Flame Rig contained a copper substrate below the sample. The distance from sample to substrate was adjustable. The substrate covered the entire area of the burning sample and acted as a heat sink to promote the onset of instabilities. The aluminum frame sample holder, to which the mica was glued, was attached to an aluminum tray, allowing the frame to be adjusted. With this design, thicker fuels up to ¼in. can be tested in the MSU Flame Rig. For thicker fuels, though, no backing is necessary. This is because the thickness of the fuel causes it to draw heat to pyrolyze, so thicker fuels act as their own substrate. The aluminum tray was painted matte black in order to eliminate reflection from the metal in the video footage.

2.3.8 MSU Flame Rig Igniter

The system igniter shown in Figure 20a provided a flat, linear flame front for most of the tests. For clarity, Figure 20b shows a schematic of the igniter system. The igniter system employed igniter wire holders made of spring steel. The same type of igniter wire that was used in the NASA tests (Kanthal) was pushed through a gold pin holder that was crimped at the end. The gold pin was similar to a dog screw in that it fit in the hole of the igniter holder, but did not go through it. It was crucial that the wire touched the sample across the entire width of the sample to ensure contact between the two. This was achieved by cutting the igniter wire shorter than the distance between the two igniter holders. Therefore, the igniter holders were deflected inward (into the page) towards the sample holder before current was passed through the wire. The inward placement of the igniter wire holders also prevented the wire from sagging when it was heated and losing contact with the sample. When sufficient current was applied to the circuit, the wire glowed bright orange/yellow and became malleable, sinking towards the copper substrate. The spring steel holders pulled the wire taut again and retained good contact with the sample because there was already a load on the spring steel holders due to their inward deflection. In this way, the holders kept the wire from sagging because they acted as a spring and pulled the wire outwards causing it to become straight and produce an even flame front.

The igniter wire holder was attached to the sample holder in a way that insulated it from the metal portion. Hence, the wire was not grounded and did not break when electrical power was applied to it. The igniter holder was connected at the end to a red

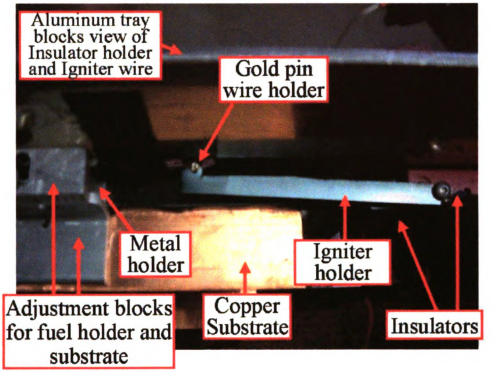

Figure 20a. Picture of MSU Flame Rig igniter system.

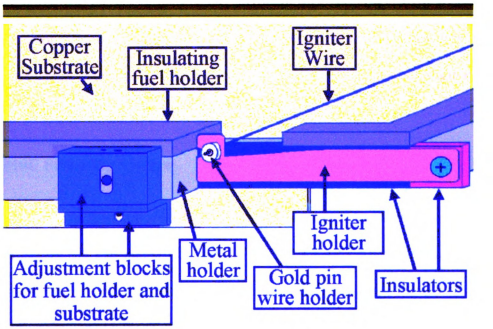

Figure 20b. Schematic of MSU Flame Rig igniter system.

Fiberglass insulator so the holder could be deflected inward. Insulator tape shown in black, which insulated the rest of the igniter holder from the metal holder, was placed along the metal holder. Wires connected the igniter wire holder leads to a voltage source. Using Ohm's law before each test, the proper amount of voltage was calculated to make the wire glow orange/yellow and reach a temperature to ignite the sample. Usually around 20-25volts and 3-5amps of current were utilized.

The space below the igniter wire holders was sealed so that no flow could escape from the test section. Also the wire holder slightly protruded into the cross sectional area of the test section. This could have caused some flow separation. However, our apparatus was an opposed flow configuration, which meant that the flame traveled in the direction opposite of the flow. Therefore, the flame moved away from this area of separation. Furthermore, the separation probably had little effect since the viscous forces were so large in this direction. Moreover, an opposed flow configuration was desired so that combustion products were washed away from the flame instead of towards the flame. If the combustion products flowed into the flame, as in a co-flow configuration, they would have inhibited the oxidizer from reaching the flame.

2.3.9 MSU Flame Rig Spacers

A schematic from the side view of the MSU Flame Rig test section and spacers is shown in Figure 21. The quartz plate lay on four posts, which are not shown, and were precision ground to 2.336in. (accurate to 10^{-4}in.). The posts kept the quartz stationary and were attached to a ½in. thick aluminum plate that supported the entire test section. The aluminum tray that held the sample holder was placed on top of diagnostic spacers,

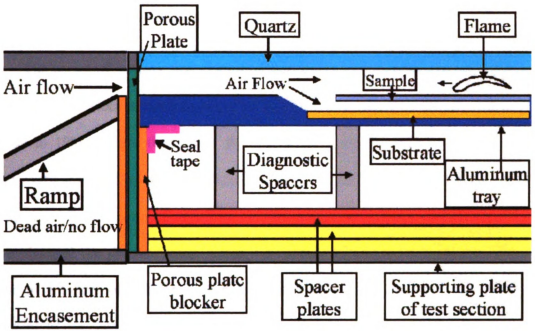

Figure 21. System of MSU Flame Rig spacers.

which were precision ground aluminum bars 1.5in. thick. These bars allowed space for any wires or equipment, such as igniter wires, thermocouple wires, heat flux gauges, etc., that had to be attached to the sample or holder. The bars were placed so that the aluminum sample tray did not sag anywhere, changing the distance between the sample tray and quartz plate. Before each test, putty was placed along the side Pyrex windows. When the sample tray was placed on the spacer bars, the putty stuck to the aluminum tray. The test section was sealed because the putty prevented air from leaking along the sides under the test section. Duct tape (labeled "Seal tape") in Figure 21 was placed along the bottom edge of the aluminum sample tray and connected to the downstream porous plate blocker. This sealed the test section by preventing air leaking from the

porous plate below the test section. The side and bottom edges of the downstream porous plate blocker were sealed with putty.

The series of spacers that changed the height of the sample were composed of precision ground stock spacers accurate up to 10^{-4}in. and aluminum shim stock spacers accurate to 10% of their thickness. By this system, sample distances from 2mm. to 10mm. were achieved by placing the correct spacers underneath the diagnostic spacers. The system of spacers raised and lowered the diagnostic spacers and aluminum tray, which changed the distance from sample to quartz. Therefore, the quartz plate was always at a height of 2.336in. This setup also helped in preventing any expensive machining of the plate.

The system of spacers were used to place the sample at very close distances to the quartz plate, which in turn produced a pseudo microgravity flame in this apparatus. The close proximity of plate to sample prevented formation of the buoyant flow pattern cells. If the quartz were not present, the hot air and combustion products near the flame would have risen because of the fluid's lighter density and the bouyant force due to gravity acting on it. After rising, the fluid would have cooled from the change in temperature of surrounding air, thus causing an increase in density of the fluid. The higher density fluid would have descended towards the flame, forming a continuous circular motion known as *Benard cells*. The MSU Flame Rig did not allow this motion to transpire, so effects of gravity were removed from the experiment, thereby simulating a microgravity flame on earth.

For the fully developed flow in the test section, the air flowed above and below the sample. A downward ramp was formed that led the flow below the sample so no separation occurred because of the downward step. The airflow under the sample was permitted for ease of future model analysis, so a flow profile between the sample and substrate could be estimated.

2.3.10 MSU Flame Rig Diagnostics

Since the first goal of this project was to produce flame instabilities, the only diagnostics utilized initially were video and digital cameras. Figure 22 shows the camera

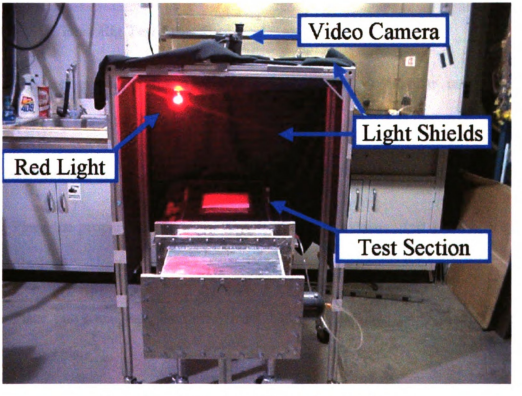

Figure 22. MSU Flame Rig camera mounting system.

mounting system, which is on wheels. This apparatus placed the camera normal to the test section so that distances would not be distorted when using either the digital or video

cameras. The mounting system allowed the user to slide over any part of the test section and zoom in or out. Black poster board and material was draped around the camera mount, so there was no light pollution in the picture. A red background light was used sometimes to obtain a better picture of the flame. For most tests, this light was off.

In the future, a recently purchased digital camcorder will give a large amount of information when coupled with a software program called TRACKER. This software program was obtained from NASA. It is a graphics program that is capable of measuring distances, areas, color intensities and quantitative results for each frame. Diagnostics that will be used later are described in the Future Work Chapter.

2.3.11 MSU Flame Rig Test Procedure

The test procedure for the MSU Flame Rig is very similar to the NASA Combustion Rig procedure.

Pre Test Preparation

- Place the proper spacers in the test section to the correct test section height is obtained.
- Place putty and tape on downstream blocker plate, and press blocker against porous plate.
- Slide aluminum sample tray onto tape, and press firmly to seal. Place aluminum tray on spacers and press firmly, so that the putty seals it along edges.
- Measure four corners to ensure proper test section height.

- Make sure using bubble tests that the flow system is sealed. (This need not be done every time.)

Sample Preparation

- Attach igniter wire to igniter wire holders using gold pins.
- Glue sample to mica using glue stick, and slide sample under igniter wire so that it lies straight across top edge of sample.
- Press and pull sides of sample to produce contact with the igniter wire. It is very important that contact between paper and wire is optimal.
- Slide sample tray into position on top of aluminum bars.

Quartz Plate Preparation

- Carefully place quartz plate on top of posts and slide against the porous plate holder.
- Using the soft putty, fill all holes at points where the quartz and Pyrex side windows meet. Also use putty to fill where the quartz and porous plate holder meet.
- Connect igniter wire leads to voltage source.

Actual Testing

- Center camera mount over sample.

- Turn on the air source valve in the hood.

- Set the pressure regulator to the proper pressure that corresponds to the desired flowrate produced by the orifice at the end of the test time.

- Open the needle valve so that the proper amount of volumetric flow rate that corresponds with the starting test section velocity is registered on the rotameter.

- Allow enough time to establish the proper pressure in the plenum, which will produce the desired velocity in the test section. This should be calculated beforehand.

- Begin video taping.

- Turn on power source that is already set to the proper voltage. Leave on for 5sec. or until uniform flame front occurs.

- Once a one-dimensional flame has formed, begin shutting needle valve at a constant rate until flame instabilities occur and develop over the sample. This takes timing and practice. If done too slow the sample burns out, and if done too fast the flame extinguishes. Note that extinction of flames may occur for either a completely shut needle valve or one that is partially opened. This will depend on other experimental conditions.

- Turn on hood fan to collect residual fumes.

CHAPTER 3
CALCULATIONS

3.1 Overview

Surface energy balances were performed for NASA drop tower tests that included thermocouple measurements. Sections 3.2.1-3.2.3 show the method of data reduction to obtain the energy calculations. Flame velocity calculations are in Section 3.2.4

MSU calculations begin in section 3.3.1 with a scaling analysis of the MSU Flame Rig. Calculations were also performed before constructing the MSU apparatus so that the correct volumetric flow rate and test section velocity, lag time of test section flow, proper porous plate porosity, and sample placement in the test section could be correctly determined. These are presented in sections 3.3.2 through 3.3.6. Due to the nature of the MSU Flame Rig, it was difficult to measure test section velocity profiles in this preliminary stage of development. Therefore, many calculations were predictions of flow behavior involving conservative estimations.

3.2 NASA Calculations

3.2.1 Surface Energy Balance Data Reduction Calculations

An energy balance at the surface of the fuel was calculated using the experimental data from NASA Rig drops. Surface energy values versus time during the entire drop were plotted to determine the characteristic energy values of these flames. This was done in order to see if reasonable energy values could be obtained experimentally at the fuel surface, since thin fuel microgravity flame energies have been measured in the past. Surface energy values at the peak temperature of the drop versus the number of flamelets formed in that particular drop were plotted. A relationship was sought that exhibited a "cutoff" energy where flamelet formation occurred. Since the energy of the flame often

determines its survival, a characteristic, or cutoff energy value was anticipated where the flame front could no longer sustain itself and would fragment into flamelets. In this case, there would be a definite distinction between peak energy values of tests with a large number of flamelets and tests with no flamelets (a flat front). The cutoff energy would show a connection between them. Finding this cutoff energy may lead to distinguishing values for the thin fuel flames, which could be applied to space flight safety. Furthermore, the relationship between flamelet formation and energy may lead to important relationships that can explain flamelet formation.

The surface energy balance illustrated in Figure 23 and shown in Equation 6 was

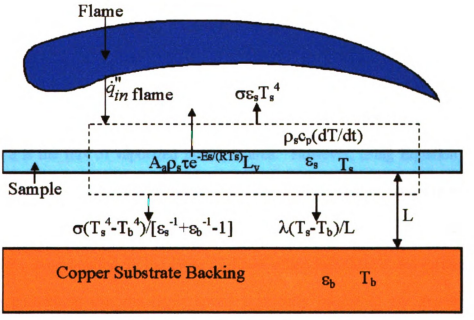

Figure 23. Fuel surface energy balance.

$$\sigma\varepsilon_S(T_S^4-T_\infty^4)+\frac{\sigma(T_S^4-T_b^4)}{\left(\frac{1}{\varepsilon_S}+\frac{1}{\varepsilon_b}-1\right)}+\lambda_{air}\frac{(T_S-T_b)}{L}+A_S\rho_S\tau e^{\left(\frac{-E_S}{RT_S}\right)}L_v+\rho_S c_p\frac{\partial T}{\partial t} = \dot{q}''_{in\ flame} \quad (6)$$

used to calculate and plot the net energy losses at the fuel surface for each test. In the above analysis, the energy equation was reduced to a two-dimensional system thereby making the control surface a series of one-dimensional inlets and outlets. The first term in Equation 6 represents the radiation from the fuel surface to the surroundings, with T_s being the variable surface temperature. The second term was the net radiation between the fuel and backing, with T_b being the variable backing temperature. The third term represents the conduction from fuel surface to backing, while the fourth is the pyrolysis or heat of vaporization term [29], which represents the flux of solid fuel being vaporized per area. The vaporization term was originally cast as:

$$\rho_s v_f L_v = vaporization\ term \qquad (7)$$

where

$$\rho_s v_f = \dot{m}'' = mass\ flux \qquad (8)$$

Equation 8 is the flux of vaporized mass per area. However, using Equation 8 for the mass flux in the energy equation caused unrealistic non-physical numbers two orders higher than real life measurements indicate. This was probably due to the fact that Equation 8 was accounting for the entire thickness of the fuel sheet in the surface density, and also postulating that the flame speed is directly related to the quantity of the vaporized mass. Instead, Equation 9 [29] was used to represent the vaporization term

$$A_S \rho_S \text{æ}^{\left(\frac{-E_S}{RT_S}\right)} L_V = vaporization\ term \qquad (9)$$

because it gave realistic values in the energy equation. Furthermore, it included the fuel half thickness in calculating the area density instead of the entire density as part of the

vaporization process, probably a more accurate depiction. Also, what made Equation 9 a better candidate was that unlike Equation 8, Equation 9 contains the surface temperature and activation energy. Thus the chemical processes and thermal properties of the fuel were accounted for as dominant forces in vaporizing the fuel rather than simply the flame velocity.

The last term on the left side accounted for the time change in total energy. The energy balance does not contain a total spatial change in enthalpy. It was hypothesized that the energy would not change significantly across a thin sample. The thickness of the sample was so small that all thermal properties and variables in the energy equation were estimated as constant across the thickness of the sample, so the fuel was considered to be thermally thin ($\{\Delta T(\text{across sample})/\Delta T(\text{characteristic})\}<<1$). The incoming heat flux $q''_{in\ flame}$ was the conduction and radiation from the flame to fuel surface. Changes in the streamwise (flow) direction were also neglected.

Table 1 defines the constants in Equation 6. From the relation in Equation 6, it

Table 1. Constants of surface energy balance equation.

A_s,	Pre-exponential factor,	5×10^{10} s^{-1} [27]
E_s	Activation energy for pyrolysis	139.6 kJ/kg [27]
c_p	Fuel specific heat	1260 J/(kg K)
L	Distance from fuel to substrate	.67 cm and 1 cm
L_v	Fuel latent heat of vaporization	368.5 kJ/kg
R	Universal gas constant	8.314 J/(mol K)
T_∞	Ambient Temperature	30 °C
ε_b	Substrate emissivity	Screens=.17, Cu=.03, Al=.04, Brass=.05
ε_s	Fuel emissivity	.95
λ_{air}	Conductivity of air @ atm Temp	.0263 W/(m K)
ρ_g	Gas density at ambient	1.2 kg/m^3
ρ_s	Fuel area surface density	.0182 kg/m^2
σ	Stefan-Boltzmann constant	5.67×10^{-8} $W/(m^2 K^4)$
τ	Half thickness of fuel sheet	.0004 in

was clear that the values needed to calculate the surface energy were the variable fuel surface temperature T_s, the substrate temperature T_b, and the derivative of the surface temperature with respect to time.

After a flamelet regime was located using the 2 second drop tower, tests were chosen in which the temperature of the fuel surface and the substrate were recorded using type K thermocouples. In addition, the flame position was tracked over time to obtain the flame speed. Each thermocouple was located in the middle of the sample at an estimated position where flamelets would occur. However, sometimes the flamelet did not pass directly through the thermocouple because it formed elsewhere on the sample. Therefore a smaller number of tests than originally planned produced the energy equation data. The population of tests was sufficiently large to accomplish the goal of determining typical energy curves for these tests.

3.2.2 Temperature Derivative Calculation

The derivative of the fuel surface temperature was calculated using a second order, central in time, Finite Difference method shown in Equation 10.

$$\frac{dT}{dt} = \frac{T(i+1) - T(i-1)}{2\Delta t} \qquad (10)$$

When this relation was used with the raw temperature data from the drops, it produced a noisy, essentially incoherent derivative. The temperature data were reduced by employing a routine from [49], [50] that "smoothed" the data. This algorithm produced a curve for the temperature and derivative that did not include the influence of measurement errors which rendered the derivative curve calculated from Equation 10 discontinuous.

Before the temperature values were smoothed and the derivative calculated, additional temperature points were generated. Temperatures recorded before the drop during the normal gravity flame were taken at .05sec. intervals, whereas temperatures during the drop were taken at .01sec. intervals. This change in time caused a spike or discontinuity in both the mollified temperature values and the time derivative. A linear interpolation program generated four fictitious temperature points between every original .05sec. interval, by calculating the slope of the line between each temperature point at the .05sec. interval. Then, using the .01sec. interval the corresponding new temperature was ascertained. This produced an even spacing of temperature values for smoothing the data.

The temperature values at equal time intervals were smoothed using a mollification process that was based on weighting the data using a "blurring radius", δ. The mollification algorithm was written based on equations from [49], [50]. Equation 11 and 12 show the calculation for each mollified point *f(n)* obtained from the data.

$$f(n) = \sum_{i=-3\delta}^{i=3\delta} p(i)Y(n+i) \qquad (11)$$

where

$$p(i) = \frac{1}{\delta\sqrt{\pi}} e^{\left(-\frac{i^2}{\delta^2}\right)} \qquad (12)$$

The value Y(n+i) was the original value of the measured temperature at point (n+i). The weighting function p(i) was an exponential function which has a value based on the distance from the original point. The negative sign in the exponential indicates that temperature values Y(n+i) far from the original point did not contribute as strongly as points near the temperature point being mollified. The larger the value of i, the less effect

it had on the mollified point. For example, for a blurring radius of δ=1, the summation was from –3 to 3 in integer values (-3,-2,-1,0,1,2,3). The three points before and the three points after the original temperature being mollified were multiplied by the weighting function calculated at each of those points and summed along with the value at i=0. For this point, the exponential was equal to one, so the contribution to the summation was just $1/(\delta\pi^{1/2})$. In this case with a radius of 3, the first mollified point in a list of data is shown in Equation 13. It was clear then that with a radius of δ=1, the first

$$f(1)=\frac{1}{(1)\sqrt{\pi}}\left[Y(-3)e^{\frac{-9}{1}}+Y(-2)e^{\frac{-4}{1}}+Y(-1)e^{\frac{-1}{1}}+Y(0)+Y(1)e^{\frac{-1}{1}}+Y(2)e^{\frac{-4}{1}}+Y(3)e^{\frac{-9}{1}}\right] \quad (13)$$

point that could be mollified in the list of data was point number 4 because the previous 3 points were needed for smoothing. The last point that could be mollified for this radius was the n-3 point since the three points in front of the mollified point were required. This will be discussed in following paragraphs.

Some points needed to be considered when choosing an effective blurring radius. If the radius chosen is too small, the mollified data resembles the noise and measurement errors in the original data. However, if the radius chosen is too large, the mollified data do not represent the true data and can possibly be offset in some places. For example, peak temperatures may be lower due to a large radius which includes many points that would "weigh" the data down. These behaviors have been observed in all types of data that have used this mollification routine. The best method to insure proper mollification was to begin with a low blurring radius, and then increase the radius and compare mollified groups of data to each other and the original data. This ensured that peak

temperatures would not be in large disagreement with the original data. Consequently, a continuous curve for the temperature that still represented the original data was produced. This study began with a radius of one and increased it to employ a radius of ten for calculation of the smoothed temperatures.

For the blurring radius of 10 used in this work, a significant amount of temperature data at the beginning and end of the test were not mollified. This was because the summation occurred from i = -30 to i = 30, so smoothing could not begin until the 31st temperature point, and it had to end at the (n-30) point. No points before the 30th or after the (n-30) points could be mollified because the summation included the 30 values before and after the smoothed temperature point. To try to mollify points before the 30th one when no data existed before them would cause the mollification to be weighted toward the side where points existed, giving an incorrect value.

In order to make the data not mollified appropriate for calculation of the derivative, the data at the beginning and end of the test was smoothed using a cubic spline, matching the ends to the smoothed temperature data. A computer program was developed to calculate a cubic polynomial that fit the data at the beginning and end of each set of temperature data. This was likewise done for the 30 end temperature points of each drop. From this a smooth profile of temperature points at the desired time values necessary for differentiation were calculated.

In the spline method, the following equation represents the data when solved for

$$a(t-t_o)^3+b(t-t_o)^2+c(t-t_o)+d=T(t) \qquad (14)$$

the constants a,b,c,d. In Equation 14 t_o was chosen so that time zero occurred where the spline curve was connected to the mollified data. So for a blurring radius of 10, $(t-t_o) = 0$

at points 30 and at n-30. These times were only used in this section of calculation. Once the spline was computed, the original times were used for the derivative and all other plots. The constants c and d were automatically determined by the boundary conditions between the spline curve and the mollified data. These boundary conditions insured that the curve was smooth and continuous where it joined the mollified temperatures. The smooth part was accomplished by enforcing continuity of temperature at the first mollified temperature value. This criterion solved the constant d. At time $(t-t_o) = 0$ the value of the polynomial equaled the first mollified temperature. Continuity was achieved by requiring a continuous derivative across the spline curve and mollified data. This meant that Equation 15 was satisfied at the end of the spline or at the point where the spline joined the smooth data.

$$\frac{dT}{dt}(t-t_o) = c = \frac{T(i+1)-T(i-1)}{2\Delta} \qquad (15)$$

This criterion solved for c. For example, in the spline at the beginning of the test T(i+1) was the second mollified point, while T(i-1) was the second to the last raw temperature point used in the spline algorithm.

The constants a and b were solved by generating a matrix using all the raw temperature values applying Equation 14 along with c and d. This produced a matrix of the form:

$$[f]=[A][x] \qquad (16)$$

which is further illustrated in Equation 17. The variables a and b, which are actually constants in this system of equations, were solved using the least squares method. From

$$[T(t-t_o)-d-c(t-t_o)]=\begin{bmatrix}(t-t_o)^3 & (t-t_o)^2\end{bmatrix}\begin{bmatrix}a\\b\end{bmatrix} \qquad (17)$$

the above method, an equation for temperature was used to create a smooth curve, and thus temperature values at the appropriate times were calculated for differentiation.

After the temperatures were mollified and the spline curves were used to obtain temperatures at either end of the smoothed data, two columns for time and corresponding temperature were constructed. The time period was over the entire drop. The mollification and spline data reduction processes produced a temperature curve that, when graphed, was smooth and continuous, so the derivative was now determined using a second order central in time scheme shown before in Equation 10.

$$\frac{dT}{dt}=\frac{T(i+1)-T(i-1)}{2\Delta t} \qquad (10)$$

Returning to the surface energy balance in Equation 6, the derivative in Equation 10 was

$$\sigma\varepsilon_S(T_S^4-T_\infty^4)+\frac{\sigma(T_S^4-T_b^4)}{\left(\frac{1}{\varepsilon_S}+\frac{1}{\varepsilon_b}-1\right)}+\lambda_{air}\frac{(T_S-T_b)}{L}+A_S\rho_S\tau e^{\left(\frac{-E_s}{RT_s}\right)}L_v+\rho_S c_p\frac{\partial T}{\partial t} = \dot{q}''_{in\ flame} \quad (6)$$

used for computing the time dependent term. The two radiation terms and conduction terms used the mollified fuel surface temperature that corresponded to the time and value of the derivative at that time. It was also concluded in testing that the temperature of the backing, which was recorded throughout the drop at a location directly behind the fuel thermocouple, did not change significantly from its initial (atmospheric) temperature. Even when the flame passed over it, the temperature of the substrate barely changed from T_{atm}. Therefore, in tests where T_b was not recorded, it was estimated to be the average temperature of the substrate during the drop, which was usually very near T_{atm}.

3.2.3 Peak Temperature Energy Loss versus Flamelets Calculation

In order to accomplish the second goal and compare energy values of different drops to determine if a "cutoff" energy existed, one characteristic temperature was chosen to substitute into Equation 6, so that there was only one energy value representing each test. The peak fuel surface temperature for each test was used because typically in past studies, this has been the temperature that dictated the instability of the flame at the leading edge. Choosing this temperature also caused the change in enthalpy term (dT/dt term) to vanish since the slope of the line at the peak temperature was zero. Therefore, the energy equation was reduced to:

$$\sigma\varepsilon_s(T_{sp}^4 - T_\infty^4) + \frac{\sigma(T_{sp}^4 - T_b^4)}{(\frac{1}{\varepsilon_s} + \frac{1}{\varepsilon_b} - 1)} + \lambda_{air}\frac{(T_{sp} - T_b)}{L} + A_s\rho_s\,\tau\, e^{\left(\frac{-E_s}{RT_{sp}}\right)}L_v = \dot{q}''_{in\ flame} \quad (18)$$

or

$$\dot{q}''_{net\ losses} = \dot{q}''_{in\ flame} \quad (19)$$

The energy losses due to radiation, conduction and heat of combustion for each test at the peak temperature, T_{sp}, were determined. Plotting these values for each test versus the number of flamelets for each test produced a relationship that yielded a critical energy flux value.

3.2.4 Flame Velocities

Flame velocities in normal and microgravity conditions were determined using the TRACKER software at NASA Glenn Research Center. These spread rates were used to compare flamelet velocities to microgravity normal gravity flame front velocities.

They were also used in the energy equation to determine the mass flux in the vaporization term. This term was, however, later calculated using a different expression. Video of each drop was digitized at NASA into thirty frames per second, then each frame of the drop was read into TRACKER. A ruler was located in one of the drop frames to determine a length scale for the drops. For each frame, the tip of the flame or flamelets was tracked, in which the software recorded the x and y positions of the flame that were later converted to actual length units. The y position of the flame was used in the analysis, since the flame traveled downward and not sideways toward the sample edges. Vertical flame position versus time was plotted in Excel and the slope of the line was calculated for the drops, which was the flame speed. Flamelets in microgravity were also tracked.

3.3 MSU Flame Rig Calculations

3.3.1 Scale Analysis

Figure 24 shows the schematic used to perform a scaling analysis in order to

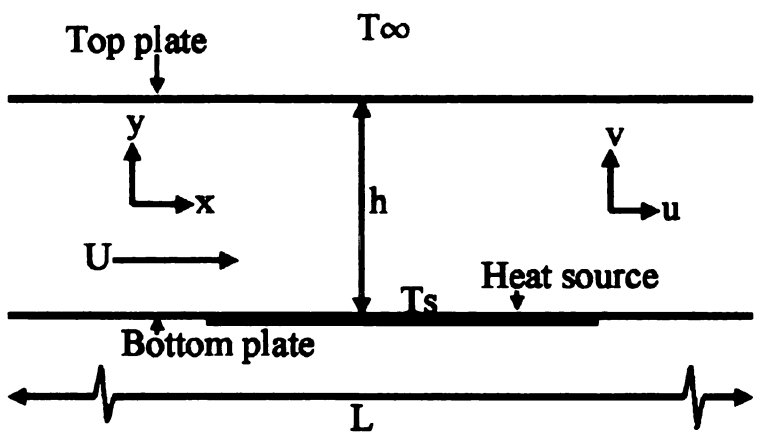

Figure 24. Schematic for scaling analysis of MSU Flame Rig.

check the assumption that the effects of buoyancy would be suppressed for test section heights, h, under 1.1cm. It was also desired to find the approximate upper limit of the test section height, h, which would suppress buoyant motion.

First, the governing equations of mass, momentum, and energy were defined in Equations (20-23) for the system. Species equations and chemical reaction terms were

Mass Conservation
$$\frac{\partial u}{\partial x}+\frac{\partial v}{\partial y}=0 \qquad (20)$$

x - Momentum Conservation
$$u\frac{\partial u}{\partial x}+v\frac{\partial u}{\partial y}=-\frac{1}{\rho}\frac{\partial P}{\partial x}+\nu\left(\frac{\partial^2 u}{\partial x^2}+\frac{\partial^2 u}{\partial y^2}\right) \qquad (21)$$

y - Momentum Conservation
$$u\frac{\partial v}{\partial x}+v\frac{\partial v}{\partial y}=-\frac{1}{\rho}\frac{\partial P}{\partial y}+\nu\left(\frac{\partial^2 v}{\partial x^2}+\frac{\partial^2 v}{\partial y^2}\right)-g \qquad (22)$$

Energy Conservation
$$u\frac{\partial T}{\partial x}+v\frac{\partial T}{\partial y}=\alpha\left(\frac{\partial^2 T}{\partial x^2}+\frac{\partial^2 T}{\partial y^2}\right) \qquad (23)$$

neglected because it was assumed that the bottom of the test section was a very hot plate, representing the flame, with temperature much greater than ambient. This would serve as the source of heat in this estimation.

In the MSU Flame Rig the characteristic test section height, h, is much smaller than the test section length, L, so ($h/L \ll 1$). Therefore, second derivatives with respect to x, ($\partial^2/\partial x^2$ terms), could be neglected since they would be much smaller than second derivatives with respect to y. Also, the Boussinesq approximation [43] was employed in the y-momentum equation where the change in pressure in the y direction is dictated by

the hydrostatic pressure gradient. Combining this with the gravity force term and using the equation of state, the governing equations become:

Mass Conservation
$$\frac{\partial u}{\partial x}+\frac{\partial v}{\partial y}=0 \qquad (20)$$

x - Momentum Conservation
$$u\frac{\partial u}{\partial x}+v\frac{\partial u}{\partial y}=-\frac{1}{\rho}\frac{\partial P}{\partial x}+\nu\left(\frac{\partial^2 u}{\partial y^2}\right) \qquad (24)$$

y - Momentum Conservation
$$u\frac{\partial v}{\partial x}+v\frac{\partial v}{\partial y}=g\beta(T_s-T_\infty)+\nu\left(\frac{\partial^2 v}{\partial y^2}\right) \qquad (25)$$

Energy Conservation
$$u\frac{\partial T}{\partial x}+v\frac{\partial T}{\partial y}=\alpha\left(\frac{\partial^2 T}{\partial y^2}\right) \qquad (26)$$

where $(T_s-T_\infty)=\Delta T$. Starting with mass conservation, Equation 20, and noting that the characteristic velocity in the x direction is U, the characteristic x value is L, and the characteristic y value is h, the velocity in the y direction scales as:

$$v\sim\frac{Uh}{L} \qquad (27)$$

From the original fact that (h/L)<<1, the y direction velocity, v, is neglected, and the x-momentum equation becomes:

$$u\frac{\partial u}{\partial x}=-\frac{1}{\rho}\frac{\partial P}{\partial x}+\nu\frac{\partial^2 u}{\partial y^2} \qquad (28)$$

$$inertia = pressure + friction$$

which scales to

$$\frac{U^2}{L},\ \frac{\Delta P_x}{\rho L},\ \frac{\nu U}{h^2} \qquad (29)$$

However, for very low flows, as in the MSU Flame Rig, the pressure and very large viscous forces would most likely dominate the inertia term in this equation due to the

close proximity of the plates and low Reynolds numbers. Therefore, the x-momentum equation renders a pressure versus friction balance, so the change in pressure in the x direction scales as:

$$\Delta P_x \sim \frac{\rho L \nu U}{h^2} \tag{30}$$

Likewise, the y momentum equation is:

$$g\beta\Delta T = \nu \frac{\partial^2 \mathrm{v}}{\partial y^2} \tag{31}$$

$$gravity = friction$$

The y-momentum equation therefore is a balance between gravity and viscous forces. The friction term was not neglected, even though the y velocity v is presumably negligible. This is because both the y-velocity and characteristic y are small, so the second derivative of the y velocity with respect to y may not necessarily be small. Equation 31 scales to:

$$g\beta\Delta T \sim \frac{\nu \mathrm{v}}{h^2} \tag{32}$$

$$gravity = friction$$

Now focusing on the energy equation, which when reduced, scales as:

$$\frac{U\Delta T}{L} \sim \frac{\alpha \Delta T}{h^2} \tag{33}$$

$$convection \sim conduction$$

From this, a scale for U is determined as:

$$U \sim \frac{\alpha L}{h^2} \tag{34}$$

By inserting this in the x-momentum equation, the pressure change in the x-direction is approximated as:

$$\Delta P_x \sim \frac{\rho L^2 \alpha \nu}{h^4} \qquad (35)$$

Using the y-momentum equation and realizing that the pressure depends on the hydrostatic gradient caused by the temperature difference, an effective pressure change in the y-direction is approximated in Equation 36.

$$\Delta P_y \sim \rho h g \beta \Delta T \qquad (36)$$

This is because the original pressure term in the y-momentum equation was approximated using the Boussinesq relation. Comparing the pressure changes in the x and y directions gives:

$$\frac{\Delta P_y}{\Delta P_x} \sim \frac{g \beta \Delta T h^5}{\alpha \nu L^2} \qquad (37)$$

Grouping terms together into non-dimensional units, Equation 37 is actually the Raleigh number based on the height of the test section times the ratio of $(h/L)^2$.

$$\frac{\Delta P_y}{\Delta P_x} \sim Ra_h \left(\frac{h}{L}\right)^2 \qquad (38)$$

Equation 38 is the key to suggesting that buoyancy may be neglected in the MSU Flame Rig. Since $(h/L) \ll 1$, the pressure ratio is very small. Then pressure changes in the y-direction are very small compared to pressure changes in the x-direction. Pressure changes in the x direction over the entire test section length were approximated to be much smaller than the pressure changes required to produce test section velocities. This is because there are no obstacles, such as screens or orifices, in the test section to induce

large pressure drops. Therefore, for the higher test section velocities like 30 cm/s, the velocity in the test section is assumed as this value over the whole length of the test section, so the change in x-velocity throughout the test section is believed to be very small. The change in pressure in the y direction is taken over the y-direction characteristic length or the test section height. In this case, if the pressure change in the y-direction were much less than x-direction pressure changes, then the y-direction velocities would be much smaller in magnitude than the x-direction velocities. This meant that for $(h./L)<<1$ and for low flow rates even as high as 30 cm/s, the y-direction velocities are much smaller than buoyant velocities. As a consequence, it was assumed that buoyant cells did not form because the characteristic velocities that support them were not present. In fact, as mentioned earlier, in theory, there is a critical Raleigh number below which buoyant cells may not form between two long parallel plates. For Raleigh numbers equal to or greater than 1708 [43], the commonly known *Benard cells* or buoyant motion will occur due to gravity and changes in temperature and density.

Equation 38 was calculated for various test section heights, in order to determine the upper limit where the test section height is too large and traces of buoyant motion would begin. In Table 2, several test section heights and two temperature differences were used to calculate the Raleigh number and pressure ratio. The test section length or x-direction scale, L, is 30in. (76cm.). The temperature difference between the flame and ambient was assumed as 600°C and 700°C. For both temperatures, the pressure ratio seemed to be much less than unity for all test section heights except 1.2cm. At 1.2cm., the Raleigh number was still below the critical number for convection, however, any test at this height would be suspect to have gravitational effects. This is because at a 1.2cm.

Table 2. Pressure ratio scaling values in the MSU Flame Rig.

T_s=600°C			
Test section height(cm)	h/L	Ra_h	$Ra_h(h/L)^2$
0.2	0.003	6.9	$4.8*10^{-5}$
0.5	0.006	109	0.004
0.8	0.01	446	0.049
1.0	0.013	873	0.15
1.2	0.016	1508	0.37
T_s=700°C			
0.2	0.003	5.8	$4.0*10^{-5}$
0.5	0.006	91	0.004
0.8	0.01	374	0.041
1.0	0.013	730	0.12
1.2	0.016	1261	0.31

test section height, $Ra_h(h/L)^2$ was not much less than one, and Ra_h was much closer to the critical Raleigh number than other heights. The critical Raleigh number (1708) is not necessarily a clear cutoff. Many numbers of this nature are approximate, in that buoyant motion may develop at values near 1708, and it may not be forming complete *Benard cells*. Therefore, it was assumed that the effects of buoyancy in the MSU Flame Rig were neglected for test section heights equal to or below 1cm., since both the scaling pressure ratio was much less than one and the Ra_h was below the critical value for buoyant cells.

3.3.2 Mass Flowrate Calculations

The desired volumetric flowrates shown in Table 3 for the velocity and test section height ranges for the MSU Flame Rig were calculated by multiplying the desired test section average velocities by the cross sectional areas of the test section. The largest flowrate, which corresponded to the largest cross sectional area times the largest velocity,

Table 3. Ranges of volumetric flow rates in MSU Flame Rig.

Ranges	Test Section Velocities (cm/s)	Test Section Heights (cm)	Test Section Cross Sectional Areas (ft^2)	Volumetric Flowrates in Test Section at STP (ft^3/hr)
Smallest	1	0.2	0.007	0.840
Largest	40	1.0	0.035	167

was 167ft^3/hr. The smallest flowrate, which corresponded to the smallest cross sectional area times the smallest velocity, was 0.84ft^3/hr. A range of 1-40cm/s was the test section velocity range because higher velocities than those in NASA tests were needed to produce the instabilities. This was because the top plate would also drain some of the heat from the flame. It was anticipated, though, that instabilities would occur below 40cm/s. This upper limit was an estimation of maximum flow velocity needed to ignite the sample and produce an initial flat even flame front. Therefore, to be safe 40cm/s was used for all flow calculations. The above range of flowrates in Table 3 was required for certain calculations to choose the correct flow orifices and porous plates.

3.3.3 Volumetric Flowrate Correction and Conversion

For the MSU Flame Rig, it was estimated that instabilities would probably occur between 1 and 30cm/s. However, the range of velocities that would produce unstable flames was not exactly known for each test section height. The only way to obtain this, was to conduct several preliminary tests for each plate height, and record the air speeds that produced the near extinction regime.

In order to pinpoint the range of velocities where instabilities occurred, a rotameter calibrated to standard conditions was utilized. Since the pressure of the air was known directly after the pressure regulator, the rotameter was placed at that point and volumetric air flowrate ranges were recorded for unstable flame conditions. From the volumetric flowrate, and assuming the entire MSU Rig system was sealed, the velocity could be indirectly obtained in the test section. Figure 25 illustrates this in a series of

1	Convert observed volume flowrate to actual volume flowrate at standard conditions.	$\Rightarrow Q_{ac} = Q_{obs}\sqrt{\frac{P_{atm}}{P_{ac}}}$
2	Convert actual volume flowrate to equivalent volume flowrate at standard conditions.	$\Rightarrow Q_{eq} = Q_{ac}\frac{P_{ac}}{P_{atm}}$
3	Calculate mass flowrate by multiplying converted flowrate times atmospheric density.	$\Rightarrow \dot{m} = \rho Q_{eq}$
4	Calculate test section velocity by dividing mass flow by atmopheric density and test section area normal to flow.	$\Rightarrow V_{test\,\mathrm{sec}} = \dot{m}/(\rho A)$

Figure 25. Calculation of test section velocities in MSU Rig from rotameter readings.

steps rather than numbered equations for ease of presentation. Since the rotameter was calibrated to atmospheric conditions, the conversion factor shown at the first step in Figure 25 was used to correct for the observed volume flowrate. The rotameter that was placed in-line at much higher pressures would read much lower volumetric flowrates since volume flowrate = mass flowrate/ density. At high pressures, the densities would also be high, thereby producing a much larger denominator than atmosphere, and consequently a lower volume flowrate. The second conversion factor at the second step in Figure 25 converted the observed volume flowrate to an equivalent volume flowrate at standard conditions. Therefore, the mass flowrate could be calculated from step 3 by multiplying the corrected volume flowrate times atmospheric density. By mass conservation, the correct test section bulk velocity was determined by dividing the mass flowrate by the density and test section area in the fourth step. In the correction and conversion factors in steps 1 and 2, instead of pressure values, densities are usually used. It was assumed, though, that air was an ideal gas and that there was little temperature fluctuation in the line. Also in this conversion, P_{ac} has usually been taken to be the outlet pressure of the rotameter. However, in this experiment, P_{ac} was taken to be the pressure indicated by the pressure regulator, which was placed directly before the rotameter. This was because the rotameter was placed at a very short distance away from the pressure regulator, and the pressure drop across the rotameter (supplied by the manufacturer) was negligible. The correction and conversion factors from steps 1 and 2 in Figure 25 were well known results of rotameter application and found in references by [51], [52], and [53].

3.3.4 Porous Plate Calculations

The porosity of the plates was chosen based on flow estimations and calculations, so that they would produce straight and laminar flow. First the minimum pressure change allowable that would produce laminar flow was calculated by estimating the maximum jet velocity in the plenum and calculating the dynamic pressure associated with it. Table 4 shows these results in the first row. Since the maximum velocity that would

Table 4. Pressure calculations for determining porous plate pressure drop.

Density ρ Upstream of Porous Plate	Dynamic Pressure $\frac{1}{2} \rho V^2$ for Jet Velocities V=40 cm/s	Pressure Drop ΔP Across Porous Plate 100 times $\frac{1}{2} \rho V^2$
1.2 kg/m^3	0.096 Pa ($1.4 * 10^{-5}$ psi)	9.6 Pa (.0014 psi)
7.6 kg/m^3	0.61 Pa ($8.8 * 10^{-5}$psi)	61 Pa (.0088 psi)

produce a stable front was assumed to be 40cm/s, then to be safe, this was chosen as the maximum velocity that would occur in the contraction or plenum. Furthermore, this maximum test section velocity was a very conservative number because the areas of the contraction and plenum were much larger than any test section area, so the velocities would be less than the test section velocity for the same mass flowrate. The porous plate was chosen so that the pressure drop across the plate was much larger than any dynamic pressure that occurred due to velocities upstream of the plate. In this way, undesirable flow patterns from these jets of air due to separation were dissipated in the plate because its pressure drop was so large. A large pressure drop was considered to be two orders of

magnitude higher or one hundred times larger than the dynamic pressure of any jets behind the plate. This gave a value of 9.6Pa. or 0.0014psi. From this calculation, the pressure drop across the porous plate helped to guarantee that any effects of the flow upstream of the plate did not create turbulent or undesirable flow downstream of the plate.

Different upstream densities of the flow were also taken into consideration in order to calculate the minimum pressure drop more accurately. From previous calculations it was determined that the largest density in the polyurethane tubing before the plenum of the system was 7.6kg/m^3. This value was obtained from the ideal gas law at ambient temperature and tubing pressure known from the pressure regulator. Therefore, the maximum possible density in the tubing would be less than this while the dynamic pressure was calculated using 7.6kg/m^3 to be conservative. Using this value, the pressure drop across the plate was still very small at 0.0088psi. From this analysis, it was evident that the smallest porous plate pressure drop allowed that would still drive the flow through the plate and minimize turbulent flow downstream was 14.7088psia.

The Mott Corporation[3] manufactured the porous plates and provided pressure and velocity behaviors in each plate for different pore sizes in the plate. Figure 26 shows this pressure and velocity data utilized to determine the porosity of the plates. The pressure drop corresponded to the pressure drop across the plate and the airflow corresponded to the velocity inside the plate. To decide the appropriate porosity, the maximum and the

[3] Trade names or manufacturer's names are used in this report for identification purposes only. This usage does not constitute an official endorsement, either expressed or implied, by Michigan State University or the National Aeronautics and Space Administration.

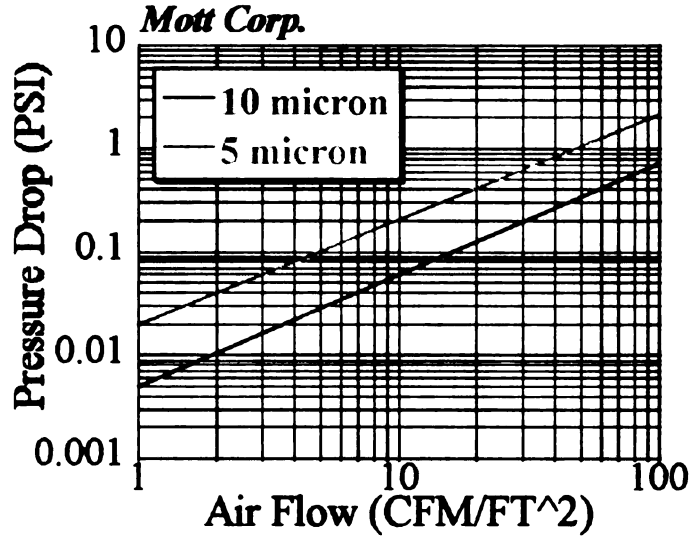

Figure 26. Pressure versus velocity behavior for Mott porous plates.

minimum velocity of the airflow directly after the plate was used. This was actually the test section average velocity. The velocity at the exit of the plates was chosen as an estimate because, in reality, the velocity of the air inside the plate was unknown. The minimum entry velocity in the test section was 1cm/s (1.97ft/min) and the maximum was 40cm/s (79ft/min). From the Mott data, it was apparent that the 5micron and 10micron size porosity plates were desirable because for the smallest velocity value (2ft/min), both plates gave a minimum plenum pressure drop above the 0.0088psi value calculated previously. From Figure 26, the 10micron plate showed a pressure drop of 0.01psi for 1.97ft/min velocity. Also, the highest pressure drop across the plates which corresponded to the largest velocity value (79ft/min) was approximately 2psi., which was possible in our system because the supply pressure of air was approximately 80psig.

3.3.5 Plenum Fill Time Calculations

The longest and shortest amounts of time required to fill the plenum were calculated. After these time periods, the plenum would be sufficiently pressurized, so that the correct velocity and therefore the desired flow conditions were established in the test section. At the beginning of each test, the largest flowrate for that test section area was used so that the sample was flushed with a large quantity of oxidizer for ignition. Therefore to determine the plenum/contraction fill time, the quantities in Figure 27 were calculated. For ease of presentation, the calculations are presented in a figure rather than

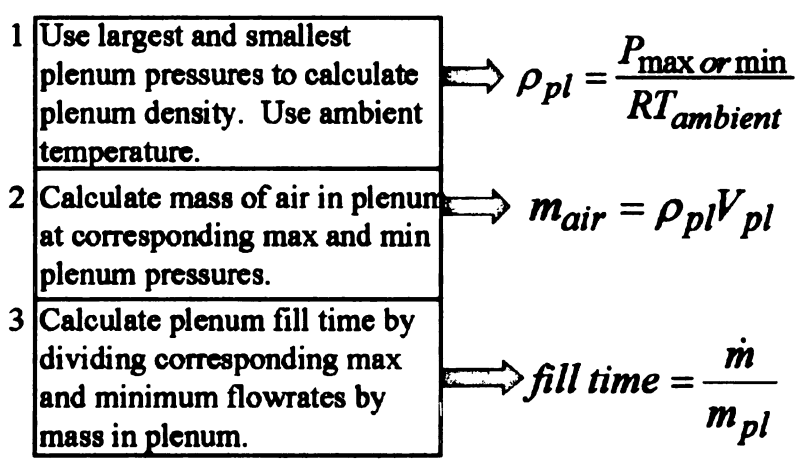

Figure 27. Plenum fill time calculations in MSU Flame Rig.

in the text. Before the first step, pressure limits of the plenum that corresponded to the largest velocities for the minimum and maximum test section areas were determined. For these calculations, flow was assumed to accumulate in the plenum/contraction and not flow through the porous plate. In reality, some flow was probably flowing through the porous plate before the driving pressure in the plenum contraction was established. The maximum and minimum pressure limits of the plenum were determined by adding

atmospheric pressure (14.7psi) to the high and low pressure drops (.4psi and 1psi) at 30cm/s (60ft/min) across the porous plate from the previous section. Using the pressure limits, the density in the plenum/contraction volume was calculated from the ideal gas law (step 1). From this density, the mass of air inside the plenum/contraction volume was calculated for the corresponding densities (step 2). Lastly, using the largest and smallest mass flowrates that corresponded to each of the pressure values that were originally used, the time to fill the plenum/contraction volume was computed by dividing the mass flowrates by the mass of air in the plenum/contraction volume (step 3).

Using the above analysis, it was assumed that test section velocities greater than 30cm/s would be required to ignite the sample. At this low-end ignition limit of pumping up the plenum, the longest fill time was calculated using the above equations and Mott pressure data. For 30cm/s and all test section heights, the longest plenum fill time was estimated to be less than 10sec. Therefore, it was concluded that this was the worst case scenario and the longest time period before steady flow conditions were established. For most tests, the plenum fill time would be even less than this because initial velocities would greater than 30cm/s. Before testing however, ignition usually did not occur within 10sec. of turning on the flow supply due to additional test preparations.

3.3.6 Entrance Length and Boundary Layer Calculations

The entrance lengths in the plane parallel to the Pyrex sides for all test section heights and corresponding velocities were calculated in this section using the analysis from Arpaci [54]. In the MSU Flame Rig, the entrance length in the test section was the distance from the porous plate after which the velocity profile no longer changes. The

concept of entrance length in the above mentioned plane in this apparatus is shown in Figure 28. The boundary layer was the region in which the flow velocity varied due to

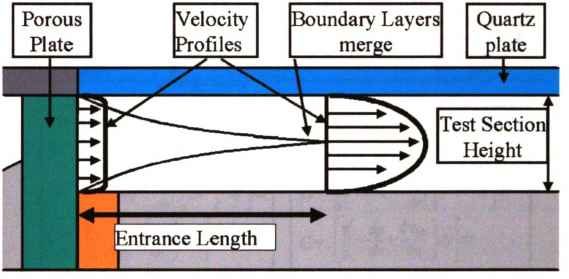

Figure 28. Entrance length in plane parallel to tunnel sides in MSU Flame Rig.

the viscous forces of the wall. Outside of the boundary layer was the freestream velocity or core flow, which was constant. When flow entered the duct, the boundary layers increased until they reached a maximum value and met. After this distance, fully developed flow in the form of the Poiseulle parabolic profile occurred.

The analysis began with the control volume denoted as CV in Figure 29, where the pressure acts on all points of the flow, not just the boundary layer. From the balance in Figure 29, the momentum equation for this control volume is:

$$\frac{d}{dx}\int_0^n uudy = -\frac{n}{\rho}\frac{dp}{dx} - \nu\left(\frac{\partial u}{\partial y}\right)_{y=0} \qquad (39)$$

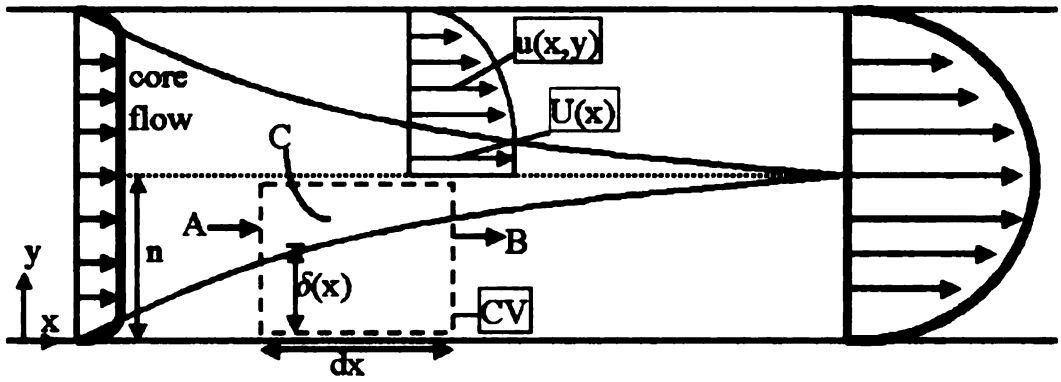

For Momentum Balance:

$$A = \int_0^n \rho u \frac{u^2}{2} dy$$

$$B = \int_0^n \rho u \frac{u^2}{2} dy + \frac{d}{dx}\left(\int_0^n \rho u \frac{u^2}{2} dy\right) dx$$

$$C = \left[\int_0^n \left(-\frac{dp}{dx} + \frac{\partial \tau_{yx}}{\partial y}\right) u dy\right] dx$$

For Mechanical Energy Balance:

$$A = \int_0^n \rho uu\, dy$$

$$B = \int_0^n \rho uu\, dy + \frac{d}{dx}\left(\int_0^n \rho uu\, dy\right) dx$$

$$C = \left[\int_0^n \left(-\frac{dp}{dx} + \frac{\partial \tau_{yx}}{\partial y}\right) dy\right] dx$$

Figure 29. Momentum and mechanical energy balances [54].

Where u is the velocity dependent on x and y, p is the pressure, ρ is the air density, and ν is the kinematic viscosity of the air. The mechanical energy equation for the control volume is:

$$\frac{d}{dx}\int_0^n \rho u \frac{u^2}{2} dy = -\int_0^n \frac{dp}{dx} u dy + \int_0^n \frac{\partial \tau_{yx}}{\partial y} u dy \qquad (40)$$

The following first order profile for velocity was assumed.

$$\frac{u}{U} = 2\left(\frac{y}{\delta}\right) - \left(\frac{y}{\delta}\right)^2 \quad ; \quad 0 \le y \le \delta \qquad (41)$$

$$1 \quad ; \quad \delta \le y = n$$

Along with the dimensionless variables:

$$\tilde{\delta} = \frac{\delta}{n} \quad , \quad \tilde{U} = \frac{U}{U_o} \quad , \quad \tilde{x} = \left(\frac{x}{n}\right)\mathrm{Re}^{-1} \qquad (42)$$

where U is the velocity in the core flow, δ is the boundary layer thickness, and Re is the Reynolds number based on the half channel width n. Equations 41 and 42 were substituted into Equations 39 and 40, which were then combined to yield the following relation between the dimensionless boundary layer thickness and the entrance length

$$7\tilde{\delta} + \frac{1233}{28}\ln\left(1-\frac{\tilde{\delta}}{3}\right) - \frac{17}{28}\ln(1-\tilde{\delta}) + \frac{99}{14}\frac{\tilde{\delta}}{1-\frac{\tilde{\delta}}{3}} = 10\tilde{x} = 10\left(\frac{x}{n}\right)\left(\frac{\nu}{U_o n}\right) \qquad (43)$$

located in the Reynolds number. The entrance length occurs where the dimensionless boundary layer thickness (δ tilde) is equal to one, when the boundary layers merge. Using a value of unity however, causes an infinite value of the natural logarithm, so the boundary layer was instead taken to be very close to unity. Substituting δ tilde equal to 0.99 into Equation 43 gave the entrance length x, which was within the dimensionless variable x tilde.

Table 5 shows the calculations of the entrance lengths in the plane parallel to the

Table 5. Entrance length ranges in plane parallel to tunnel side walls.

Velocity U_o (cm/s)	½ channel width (cm)	Reynolds #	Entrance length (cm)
1	0.1	0.67	0.02
40	0.1	26	0.66
1	0.5	3.3	0.41
40	0.5	133	17

tunnel side-walls for the maximum and minimum test section velocities and heights. The largest entrance length that was calculated for all the MSU Flame Rig flow conditions was approximately 17 cm (6.7 in). This was calculated using the largest possible velocity that would be used in the largest test section height, which would produce the largest possible Reynolds number. The sample was not placed at a downstream distance from the porous plate smaller than the entrance length because the boundary layers would still be developing. If it were, then the velocity profile would be changing over the sample and therefore possibly introducing more variables affecting flame instabilities. In the MSU Flame Rig, 2.3in. additional distance was allowed, so the beginning of the sample was 23cm. (9in.) from the porous plate location. By doing this, flow over the sample would always be fully developed, so that an approximate average velocity was estimated over the entire sample.

Entrance lengths were also calculated in the plane parallel to the quartz plate using Equation 43. In this dimension, the half channel width is 16.5cm. (6.5in.) because the width of the quartz plate or test section is 33cm. (13in.). From the results shown in Table 6, it was evident that boundary layers never merged since entrance lengths were so much larger than the length of the test section which was 84cm. (33in.). Therefore, the

Table 6. Entrance lengths in the plane parallel to quartz plate.

Velocity U_o (cm/s)	½ channel width (cm)	Reynolds #	Entrance length (cm)
1	16.5	104	460
30	16.5	3300	13830
40	16.5	4400	18440

sample or at least part of the sample was always located in the core flow. The boundary layer thickness on each side of the test section along the Pyrex sides was computed to determine where the sample was located in relation to the boundary layer. Before proceeding, it is important to point out that every effort was made to place most of the sample in the core flow in this dimension. However, due to the high cost of a large quartz plate, 33cm. (13in.) was the maximum width that could be purchased.

The boundary layers shown in Figure 30 along the sides of the Pyrex windows were computed using the Blasius equation [43].

$$\frac{\delta}{x} = \frac{4.92}{\mathrm{Re}_x^{1/2}} \qquad (44)$$

Here x is the location of the beginning or end of the sample in the test section, δ is the

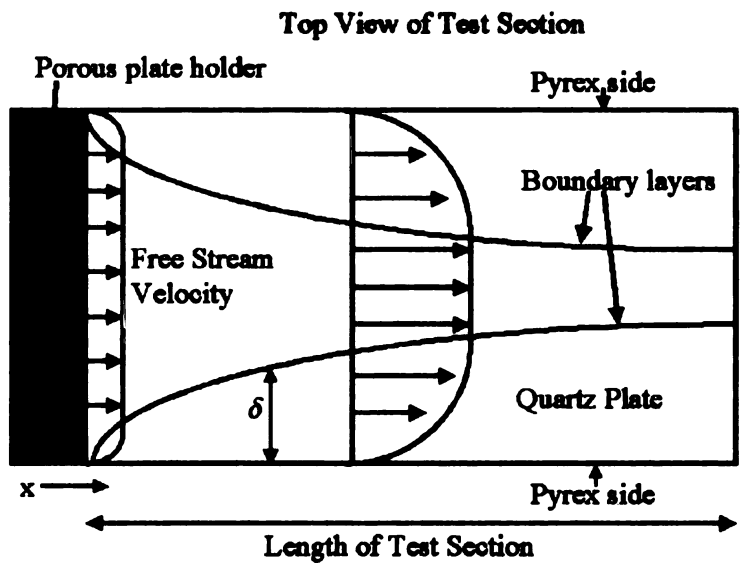

Figure 30. Boundary layers in plane parallel to quartz plate in MSU Flame Rig.

boundary layer thickness, and Re_x is the Reynolds number with respect to the location of the sample and test section velocities. Table 7 shows the boundary layer thickness at the

beginning and end of the sample shown in Figure 31. The beginning and end of the sample were chosen as locations to measure the boundary layer, to ascertain how the boundary layer changed along the sample and if the sample was located in the core flow.

Most of the boundary layer values indicated that the sample was in the freestream velocity in this dimension, but the maximum value of the boundary layer for all the MSU Flame Rig conditions at 1cm/s test section velocity was 12.5cm. (4.9in.). This value was obviously for the lowest test section velocity and at the end of the test section. For the same velocity at the beginning of the test section, the boundary layer was 9.2cm. (3.6in.) meaning the boundary layer grew 3.3cm (1.3in.) on each side along the sample. In the MSU Flame Rig, the sample was placed in the middle of the Aluminum tray at a distance of 6.4cm. (2.5in.) from the sides of the Pyrex walls shown in Figure 31. From Table 7, it was clear that the sample was located in the core flow for all test section velocities greater than or equal to 4cm/s. At this velocity, the boundary layer at the end of the sample was located at the very edge of the sample. Also from the table, at 2cm/s, at the beginning of the sample, the boundary layer was at the edge, however, it grew to include the edges of the sample downstream. Therefore, at 2cm/s, the sample edges were within the edge of the boundary layers.

Since we were studying flame instabilities, which are a function of velocity, the boundary layers for velocities lower than 4cm/s should be taken into consideration. If instabilities arose at the sides of the sample for this range of velocities, then explanations must include the effects of the changing velocity within the boundary layers. However,

Table 7. Boundary layer thickness at the beginning and end of sample.

Test Section Velocity in (cm/s)	Boundary layer thickness in (cm) at distance from beginning of test section to beginning of sample (9 in or 23cm)	Boundary layer thickness in (cm) at distance from beginning of test section to end of sample (17 in or 43cm)
1	9.2 cm	12.5 cm
2	6.5 cm	8.8 cm
4	4.6 cm	6.3 cm
10	2.9 cm	4.0 cm
30	1.7 cm	2.3 cm
40	1.4 cm	2.0 cm

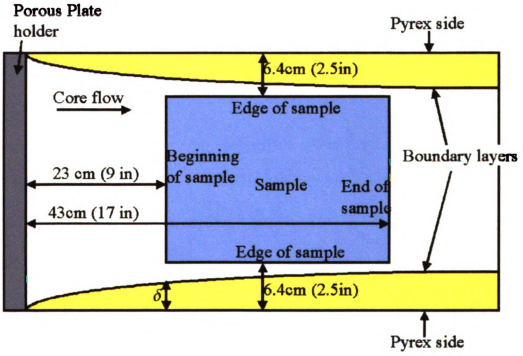

Figure 31. Sample location and boundary layers in MSU Flame Rig test section.

an argument can be made to show that this may be inconsequential. It was explained before that the MSU Flame Rig was really a Hele-Shaw apparatus. In this type of experiment, the viscous forces were so dominant in one dimension, that the plane of the other two dimensions would exhibit "inviscid" flow behavior. In fact, Hele-Shaw devices are used to observe inviscid and irrotational flow patterns ("Potential Flow") in the dimension for which the preceding boundary layers were being determined (Figure 31). A short sequence of calculations can show that flow is irrotational [42] in this top view plane in Figure 31. Therefore in this plane, the flow can be described using "Potential Flow Theory", so the viscous forces in this plane are presumed to be negligible. Consequently, the boundary layer would have had little effect on the flow across the sample in this plane. Explanations of the instabilities at the edges of the sample for the suspect velocities will include all parameters that can destabilize the flame front.

CHAPTER 4
RESULTS AND DISCUSSION

4.1 Overview

Drop tower results provided regions of flame instability, which were characterized by oscillating flamelets. Oscillation frequencies and behaviors were measured in size and flamelet intensity. Flame spread rates were calculated using Tracker. Select tests also included thermocouple measurements throughout the drop on the fuel surface and substrate. Thermocouple data in conjunction with flame spread results were applied to a fuel surface energy balance. Two types of energy balances were plotted: one energy balance over the entire test, and a second energy balance using the maximum temperature so tests could be compared. All results were preliminary, but beneficial for pinpointing required future measurements to quantitatively explain instability mechanisms. Drop tower tests indicated the necessary upgrades to the sample holder and diagnostics for the MSU Flame Rig and the International Space Station specifications.

The MSU Flame Rig was successfully completed, and preliminary flow measurements were recorded. An effective ignition system consistently formed flat, flame fronts in the test section. Flame instabilities were produced from a stable flame front, and video data were recorded.

4.2 NASA Drop Tower Results and Discussion

4.2.1 NASA Instability Regions

Initial groundwork testing performed without any substrates attempted to produce flame instabilities by reducing the oxygen concentration to the normal gravity extinction limits, which are 17-20%. Stable, one-dimensional flame fronts were not produced at

such low values, so an increase in heat loss was pursued instead. The heat loss parameter was introduced by placing a metal backing within 1cm. away from the back surface of the fuel. In most tests, a stable flat, flame front began in normal gravity, continued through transition to microgravity, and finally broke into separate flamelets that oscillated, recombined, or extinguished. A flame front resembling the original flame front often resulted when flamelets occasionally recombined.

A pictorial story line of a typical test is shown in Figure 32 on the following page. Most photographs of experimental tests in this thesis were manipulated using image-processing software so the flames and flamelets could be more easily viewed. This was done solely because many of the flames were dimmer than the video after being digitized into separate frames. If the images had been printed after being digitized, the geometry and colors of the flamelets would be indiscernible. The relative colors and intensities between flames or flamelets in the same picture were not changed. For a specific frame, the color or brightness of one flame was not improved without changing the other flames in the picture by the same amount. Therefore, the original contrasting features between flamelets was retained. Furthermore, the geometry of the flames and flamelets were not changed from the source video. Time zero is taken to be the instant a uniform normal gravity flame front was formed.

The flame spread rate direction is downward on all *top* views in this thesis, such as the ones shown in Figure 32. The transition to microgravity was denoted by the flame color change from yellow to blue, suggesting the decrease in oxidizer supplied to the flame due to the lack of buoyant motion. Transition duration depended on the velocity of the oxidizer. Soot formation was reduced in microgravity. The small bright spots were

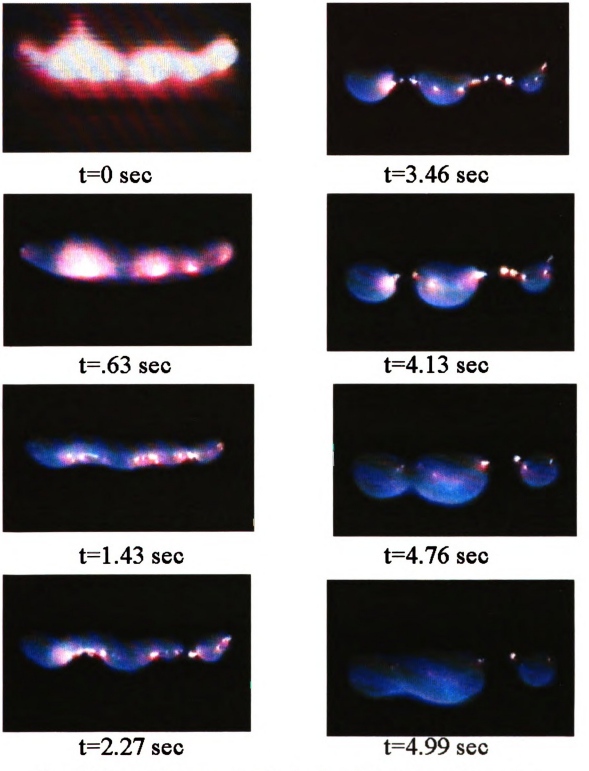

Figure 32. Typical drop tower test showing flamelet formation and interactions.

not flames but char pieces, regions of smoldering that usually did not survive. Instabilities occurred when the smooth flame front became corrugated and broke apart into separate flames. The substrate acted as a heat sink by absorbing heat from the backside of the sample. Without the heat sink, the flames would have otherwise continued as a flat flame front until the test was over, or all of the fuel was consumed. In essence, the backings allowed higher oxygen concentrations and higher opposed flow velocities. Air was used for all tests because the fuel was guaranteed to ignite for the smallest flow velocities (1cm/s) in normal gravity, or beginning test conditions. Opposed flow velocities dispensed any residual buoyancy that accumulated near the flame in the pre-drop normal gravity conditions. The air flow also assured sufficient spread rates that would undergo transition into flamelets. In tests with the substrate, the low opposed flow velocities were ample to produce a flat flame front in normal gravity, but high enough to sustain the microgravity flames and avoid blowoff (flow velocity is much larger than chemical reactions for flame to survive). In fact, the opposed flow rates were chosen so that the flame would continue regardless of the heat loss and also produce instabilities within the 2.2sec. drop time.

Aluminum foil was the first substrate, which helped attain the first goal of producing an observable region of instabilities. The results of this substrate are presented in Table 8.

An observable region of flamelets existed for velocities between 2cm/s and 4cm/s. For tests below 2cm/s of flow, the microgravity flame or flamelets always extinguished, and those above 4cm/s always generated a smooth flame front that did not break apart.

Table 8. Experimental results for drop tower tests with aluminum foil substrate.

Air Velocity (cm/s)	Number of tests conducted	Tests with flamelets	Tests that extinguished
2	2	1	1
3	3	1	1
4	6	4	0
5	3	0	0

Above 4cm/s the flame remained stable because enough oxidizer was delivered to burn all of the fuel across the entire sample and thus keep the front from corrugating. Below 2 cm/s, an insufficient amount of oxygen was supplied to the flame front and flamelets, which made them extinguish. Most flamelet development was seen at the 4cm/s velocity where four out of the six tests showed flamelets and none extinguished. For the lower air flow rates, the flamelets were most likely not receiving enough oxygen to survive, so they quenched. The main shortcoming of the aluminum foil backing was that it did not remain rigid during the tests. Instead, heating and cooling due to the flame would cause the foil to deform. This changed the foil/sample distance at different points along the sample, causing an uneven distribution of the heat sink. This irregularity in the substrate may have caused the onset of instabilities in local regions of the fuel. If one portion of the foil were wrinkled, placing it closer to the sample, then at that point more heat may be drawn from the flame. This could cause the flame to break apart at that point. In order to control the substrate distance from the sample, thicker, more rigid substrates such as steel, copper, and brass were later utilized.

A thicker steel backing produced a larger region where flame instabilities were observed because the conductivity of steel was four to ten times smaller than aluminum. The results are shown in Table 9. To account for the thicker heat sink, the steel was

Table 9. Experimental results for drop tower tests with steel substrate.

Air Velocity (cm/s)	Number of tests conducted	Tests with flamelets	Tests that extinguished
1	3	2	1
1.5	2	2	0
2	4	3	0
3	3	3	0
4	3	2	0
5	1	0	0

placed further from the sample than the aluminum foil. This reduced the heat being absorbed from the flame, and possibly aided in producing a larger instability range. In these tests, flamelets were seen at tunnel velocities between 1cm/s and 4cm/s.

Similar ranges for the copper and brass substrates were produced. However, only the beginning two substrate results are shown because the first goal of showing an observable region of microgravity flame instabilities was accomplished. Some solid backings were painted black to change the emissivity of the substrate. These results will be discussed in a later section. It was discovered that if steel screens were used as backings, which allowed air to diffuse from the back of the sample, a flatter beginning flame front resulted. The screens, though, were no longer used because a better igniter system like in the MSU Flame Rig was installed which produced excellent initial flame fronts. Also, the diffusing air towards the back of the sample added another complication for future models.

From these tests, the fact that different substrates produced similar instability ranges, supported regarding these instabilities as a fundamental attribute of diffusion flames.

4.2.2 NASA Instability Characteristics

The top and side camera views, like those shown in Figures 33a and 33b,

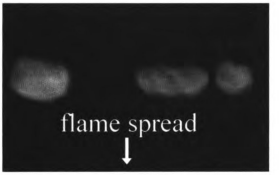

Figure 33a. Flamelet top view.

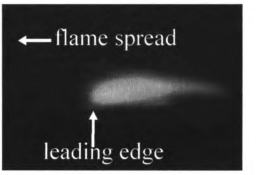

Figure 33b. Flamelet side view.

illustrated that the flamelets were three-dimensional entities. The top view shows oval or circular flamelets, and side view shows the familiar crescent shape. Flame spread direction for all *side* views was to the left, or in the direction the leading edge pointed. Flame spread for all *top* view flames was always downward. The two views indicated that any numerical computer simulation of such flames must be three-dimensional. For flames close to extinction, the leading edge of the flamelet lifted vertically away from the paper. A time sequence of this is shown on the next page in Figure 34. As the drop progressed, the flame became thinner denoting possibly a decrease in chemical reaction intensity. The leading edge lifted more and moved back towards the tail until it finally disappeared. Therefore, it was evident that the flame needed more oxygen because it was "reaching" away from the fuel surface. Standoff distances (the distance from flame to fuel) of these flames were larger than stable flames, indicating they were fuel rich and

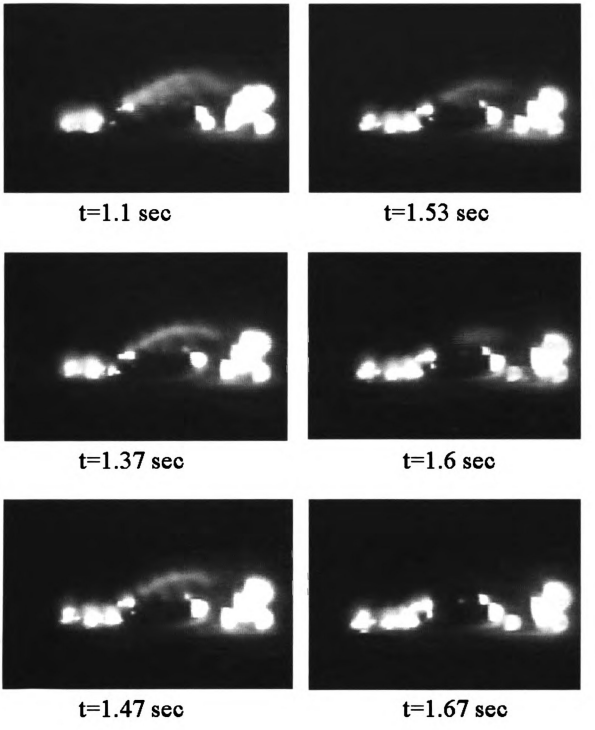

Figure 34. Side view of progression of flamelet extinction.

needed more oxidizer. Stable flamelets that lasted throughout the drops had leading edges that were closer to the sample than unstable flamelets. Even though the nature of the flamelets suggested that an entire three-dimensional simulation is necessary, valuable information was discovered from two-dimensional analyses of experimental results that will be discussed in later sections.

The side view also showed that sample to substrate distance affected the flamelets and flame fronts. For substrate distances close to the sample (around 5mm.), only the top side of the flame spread along the sample because enough heat was removed that the flame quenched on that rear sample side. Examples of this are shown in the previous Figures 33b and 34. For substrate distances between 0.5-0.8cm., the flame partially wrapped around the leading edge of the sample. In other words, the usual crescent shaped flame spread on the top; however, at the leading edge, the flame wrapped around to the backside of the sample near the substrate. On the backside, though, only part of the crescent shape was seen. Substrate distances around 1cm. were far enough away from the sample that another flame which mirrored the top flame formed, so two crescent shaped flames spread on both sides of the fuel.

For the 10.5cm. sample width that was used in these tests, usually no more than three flamelets would form. Sometimes only one or two flamelets occurred, however, when three were produced as in Figure 35, they were frequently evenly spaced across the sample. This spacing suggested that flamelets could not survive very close to each other due to the fuel and oxygen transport regions around the flamelets. If the flames were too close to each other, one of them would consume the oxidizer influx near the second flame, depleting it of a necessary component. This would cause the other flamelet to

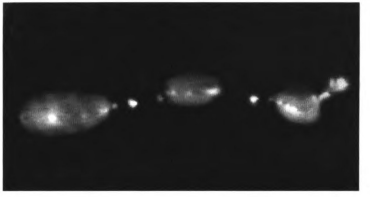

Figure 35. Typical spacing between three flamelets.

extinguish. In fact, this is exactly what happened in certain tests. In some drops like the one shown in Figure 36a and 36b, the flame front corrugated and separated into flamelets

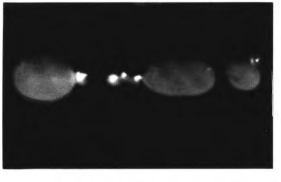

Figure 36a. Test with close flamelets.

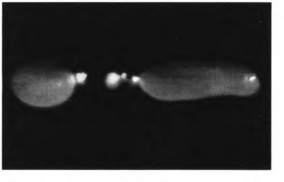

Figure 36b. Combination of flamelets.

that were quite close to one another. Usually, one of the flamelets was larger than the other one. As time progressed, the larger flamelet grew in surface area and seemed to swallow the smaller flamelet. In another view, the smaller flamelet extinguished. Sometimes the recombination of the two produced a mini flame front that extended partially across the surface. The mini flame front in Figure 36b was the result of the

combination of the right two flamelets shown in Figure 36a. In other drops, the larger flamelet increased or remained the same size. In all of these cases, it was clear that a definite region around the flamelets existed where the fuel and oxygen transport was crucial to the survival of the flamelet. It was concluded that the even spacing in some tests was a semi-stable configuration in which sufficient fuel and oxidizer enabled the flamelets to exist.

Flamelets near extinction would oscillate. From the top view, the flamelet would grow in size, shrink, and then grow again. This motion was quantified and will be discussed in greater detail in the next section.

Flamelets were either circular or oval from the top view. Examples are shown in Figure 37a and Figure 37b. The more stable flamelets were oval, with the major axis

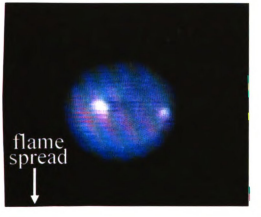

Figure 37a. Spherical flamelet.

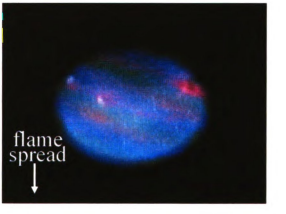

Figure 37b. Oval flamelet.

along the width of the sample and the minor axis along the direction of flame spread. They resembled mini flame fronts on a smaller scale. Circular flamelets were closer to extinguishing. Flamelets that would shrink to quenching were always circular, and this

rapid decrease in size was seen at the lowest air velocities. This suggested that stability depended highly on oxygen delivery to the flamelet. The fact that the shape was circular near extinction also insinuated that the flamelets near extinction might be trying to create a "lowest energy configuration" to survive. Many processes in nature tend toward the least energy possible, and an example is the raindrop, which is spherical in shape because this is the geometrically lowest attainable energy-state.

All flames and flamelets in microgravity were blue in color implying lower temperatures than flames in normal gravity which were yellow from the high soot production. The lower temperatures occurred because the absence of buoyancy made the diffusion of fuel vapor and oxidizer the primary source of mixing, so the flame burned less vigorously in microgravity than normal gravity. As seen from the previous figures, the intensity of blue was different in various regions of the flamelets. Oval flamelets had bright blue leading edges with more diffuse backs. This was enhanced for more stable oval flamelets because these flamelets would not oscillate, but spread down the fuel. The leading edge and sides of the flamelets were bright blue tracing out the shape of a bowl, whereas the far middle and back portions were less luminous. Circular flamelets near quenching had a more homogenous distribution of the color intensity. One possible explanation for these differences in intensity is that the more stable oval flamelets were attempting to become a fuel front due to an adequate amount of fuel and oxidizer. The leading edge of this mini flame front was preventing three dimensional oxidizer flow from traveling to the back of the flame so the chemical reactions were weaker indicated by the decrease in color. The intensity of circular flamelets was more uniform because oxidizer could reach the back portion of the flame by traveling along the sides of the

flamelet. Therefore, chemical reactions in the back of the flame would be more intense in the circular rather than oval flamelets. Furthermore, circular flamelets were near extinction and attempting to achieve a lower energy limit. These are all incipient rationalizations for which attempts at quantification will be made in future testing.

A very interesting characteristic that was also seen in Dartfire testing of thick fuels by Olson [55], was that the side flamelets near the insulating holder would sometimes propagate ahead of the middle flamelet or horizontal line of the flame front. This phenomenon was mainly seen in the longer time period testing in the Zero-G drop Tower. An example is shown in Figure 38. One possibility for this behavior was that the

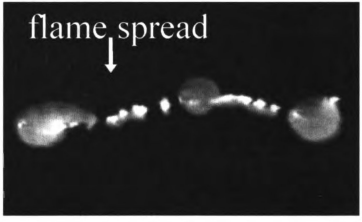

Figure 38. Typical test with faster side flamelets.

side of the flamelet close to the edge of the holder contained more oxygen than the side near another flamelet. On the sides, there were no adjacent flamelets to compete with for oxygen, so the three-dimensional oxygen transport mechanism was correspondingly magnified. Another explanation was that the holder, which was not a perfect insulator,

may have been conducting heat ahead of the flamelet feeding the flame with energy, and thereby increasing the flame speed. Future investigations will address quantifying and supporting the above proposed explanations.

In the 5 Second Drop Tower, flame fronts corrugated and broke apart into flamelets that oscillated, recombined, or extinguished. However, air velocities in the 5 Second Tower in which flamelets were observed were larger (4-10cm/s) than in the 2.2 Second Tower (1-5cm/s). This may have been caused by the back-pressure regulator used to regulate airflow in the test section in the 5 Second Tower or by the fact that the gravity levels in this facility are lower. The same flame phenomena, though, were seen in the tests in the Zero-G tower as in the 2.2 Second Tower.

4.2.3 NASA Flamelet Oscillations

In many tests, flamelets exhibited oscillatory motion in size from the top view. Flamelet oscillations always began as an increase in the surface area, then a decrease, and repetition of this action until the drop ended. A time sequence of this is shown in Figure 39 on the next page. In the time sequence, the right flamelet formed at 2.25 seconds, shrank to its smallest size at 3.36 seconds, then grew larger at the end of the drop. This periodic change in size indicated the beginning of oscillatory behavior, which most likely would have continued if the drop time were longer. In some cases, the flamelet would shrink to quenching after a couple of oscillations. For most tests, though, the short drop time would end before the flamelets extinguished. Thus, it was not possible to determine if the oscillations would persist indefinitely, which supported the longer duration of testing needed in space flight.

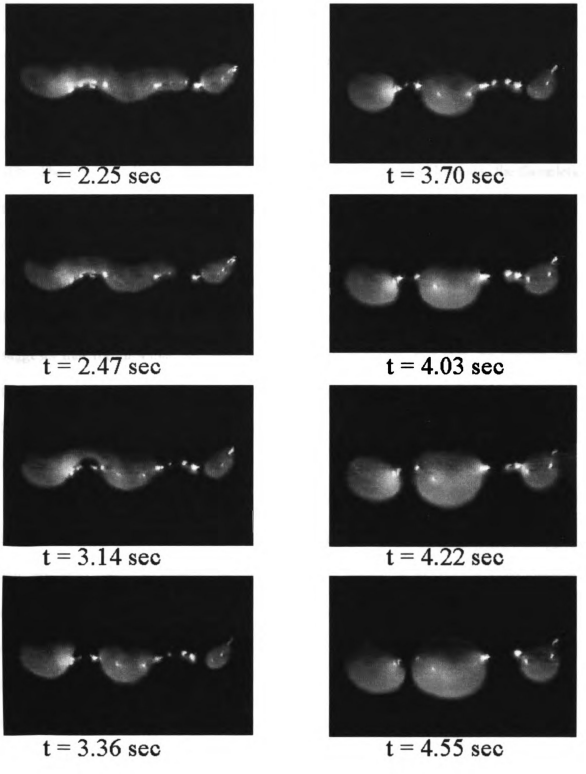

Figure 39. Time sequence of right flamelet oscillations.

Oscillations were much more prominent along the major axis of the flamelet, parallel to the width of the sample. Minor axis movement was much less extreme. Therefore, oscillation frequencies were measured using the major axis. Examples of oscillations along the major axis are shown in the plots in Figure 40a. The line along which the major axis was measured for the first plot in Figure 40a is shown in Figure 40b. The results in Figure 40a had identical air flow velocities. However, the flamelets measured were located at different parts of the sample, so frequencies were not affected by position on the sample. Time zero was the instant that the flamelet formed from the flame front within the 2.2sec. drop interval. Frequencies were always on the order of 1Hz., the same frequency as the microgravity candle flame experiments, [4]. This suggests that the unstable mechanisms are fuel independent, and that the present and future related studies can be applied to fundamental knowledge of the near extinction limit region. One limitation in these tests was that no more than 2 oscillations were seen in the 2.2 Second Tower.

The oscillations indicated that the gas phase processes were unsteady. A potential interpretation is that the flamelet increased its surface area to enhance diffusional oxygen delivery, then shrunk to preheat the fuel and sustain the chemical kinetics. The flamelet continued this balance mechanism until it recombined with another or could no longer endure and extinguished. As the flame moved outward, the chemical kinetic times were longer compared to flow times so the Damkohler number became smaller. Therefore, since the mixing of the fuel and oxidizer was faster than the reaction, one or both of the reactants leaked through the reaction zone. This may have caused a thermal diffusive instability.

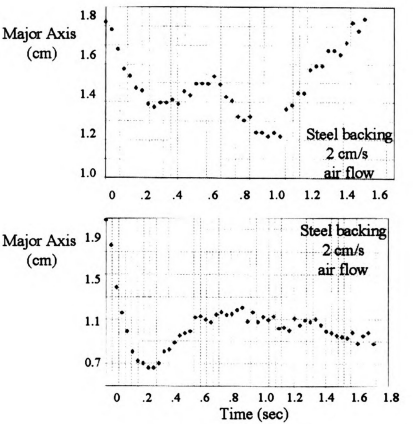

Figure 40a. Examples of time periods of major axis flamelet oscillations.

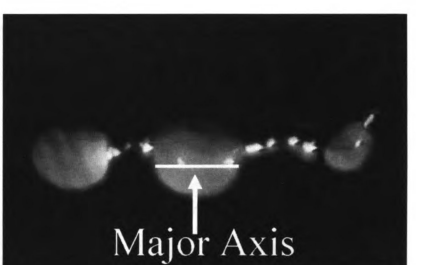

Figure 40b. Major axis of oval flamelet.

Oscillations were never seen at the lowest oxidizer velocity with the aluminum foil backing, but were seen at the same flow rates with the steel backing. This showed that the stability of the flamelets was directly related to the backing material, distance between backing and sample, and oxidizer velocity. Future tests will strive to determine these relationships in more depth.

Tests conducted in the 5 Second Drop Tower were in general agreement with the 2.2 Second Tower. Oscillations were observed and occurred along the major axis, and the substrate backing greatly affected the heat loss and thus instabilities. Oscillation frequencies were the same order of magnitude as 2.2 Second Tower tests. In this tower, some flamelets continued to oscillate during the entire drop without extinguishing while others quenched or recombined to form a new flame front.

In some of the 5 Second Drop Tower experiments, flamelet intensity in the blue region was tracked over time and showed an oscillatory nature. Figure 41 shows a frame for a typical test in which this behavior occurred. In Figure 42a, the change in blue

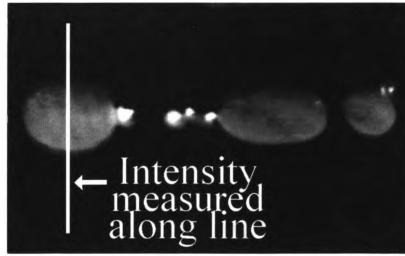

Figure 41. Line profile along which intensity measurements were taken.

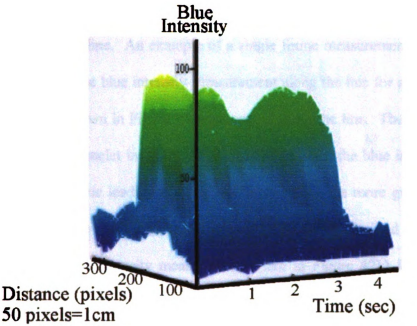

Figure 42a. Intensity in blue region over drop time along line profile in Figure 41.

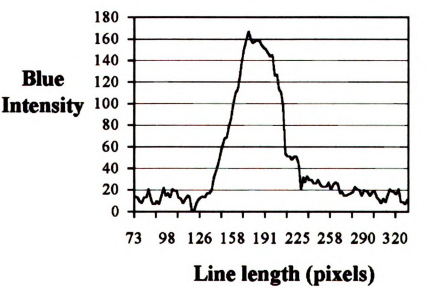

Figure 42b. Intensity measurement for single frame of drop with flamelet along line profile in Figure 41.

intensity along the white line profile shown in Figure 41 was measured over the time of the drop. For each frame of the video, the intensity in the blue region was measured at every pixel along the line. An example of a single frame measurement is in Figure 42b. This plot represents the blue intensity measurement along the line for a frame in the drop when the flamelet shown in Figure 41 was located along the line. The "hump" in Figure 42b represents the flamelet intensity. The steep increase in the blue intensity on the left denotes the intense blue leading edge of the flame, while the more gradual decrease on the right indicates the more diffuse back. Figure 42a was obtained by "stacking" the consecutive frames of intensity measurements (like in Figure 42b) for the entire drop time.

From Figure 42a, it was evident that the blue intensity of the flamelet oscillated throughout the drop. Sometimes, the intensity was measured in the dead space between flamelets during the drop since they would recombine with others or extinguish. The oscillatory nature, however, was not due to the absence of a flame along the line. For example, the oscillations in Figure 42a were not because the flamelet extinguished during part of the drop. In Figure 41, the flamelet was present along the line for the entire drop. The oscillatory results indicated a periodic fluctuation in the chemical processes of the flamelets, not just the size. Since it was evident that energy processes may be oscillating, these measurements pointed out the need for quantitative temperature measurements.

4.2.4 NASA Flame Spread Rates

Flame spread rates in microgravity were calculated by tracking the leading edge of the flame or flamelet over the entire drop. All plots showed a linear curve, for which the slope was the spread rate. Figure 43 displays the relation between flame spread rate,

opposed air velocity and backing distance for both microgravity and normal gravity flames. The backing distance is denoted by the size of the bubble radius, so a larger

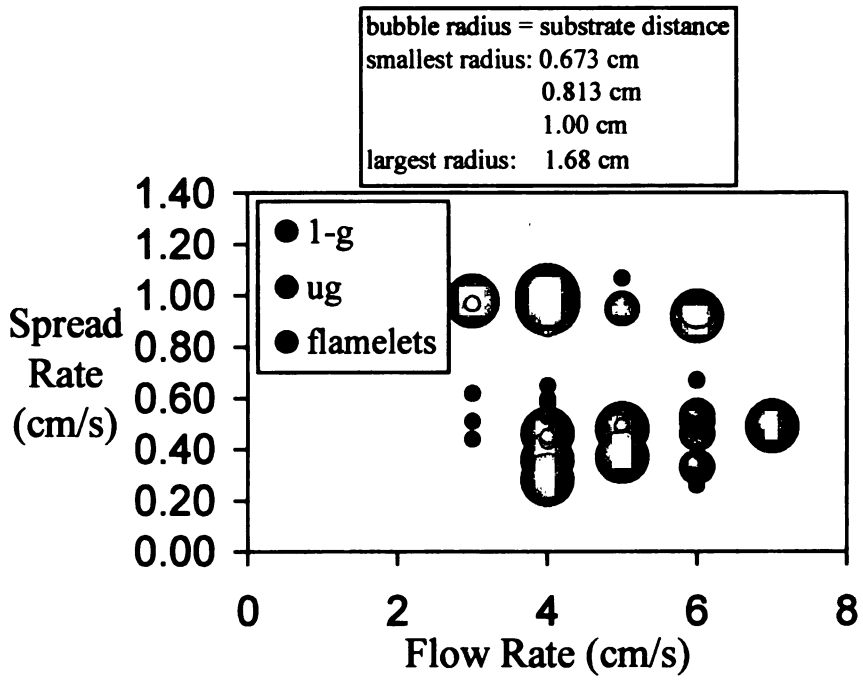

Figure 43. Flame speeds versus substrate distances and air flowrates.

radius means that the backing was further from than sample than for a smaller bubble radius. The purpose of this plot was to check that the flame spread rates for flame fronts and flamelets were plausible and to study any relationships that may exist between flame spread rate and substrate distance.

Normal gravity spread rates did not change due to the opposed oxidizer flow or the change in backing distance. This was consistent with the opposed flow velocities being smaller than buoyant flows, which dominate the spread rates at low flow in normal gravity. The buoyant velocities created vigorously burning flames that were much hotter

than microgravity flames, so the substrate was not an effective heat sink that altered the spread rates. Nearly all microgravity flame fronts and flamelet spread rates were much lower than the normal gravity spread rates due to the weaker burning rates and lower temperatures in microgravity from lack of buoyant mixing. Only one microgravity flame had a large spread rate near normal gravity values. This occurred for the largest substrate distance, so the substrate was totally ineffective.

Figure 43 shows that the substrate distance influenced the spread rates for microgravity flame fronts and flamelets more than the oxidizer flow rate. For most oxidizer flowrates, approximately the same range of microgravity flame velocities was produced. However, for each individual flowrate, the microgravity flamelet and flame front spread rates varied. Therefore, it was concluded that backing distance was a primary parameter that affected microgravity flame spread rates and flame behavior.

4.2.5 NASA Surface Energy Balances

Energy balances at a single point on the surface of the fuel were calculated throughout the entire drop. From the calculations presented in Sections 3.2.1-3.2.3, the surface energy losses due to radiation, conduction, and vaporization, plus the total enthalpy change in time throughout the drop were plotted. The sum of these quantities equaled the unknown heat flux coming in from the flame. In particular, Equation 6 was

$$\sigma\varepsilon_S(T_s^4 - T_\infty^4) + \frac{\sigma(T_s^4 - T_b^4)}{\left(\frac{1}{\varepsilon_s} + \frac{1}{\varepsilon_b} - 1\right)} + \lambda_{air}\frac{(T_s - T_b)}{L} + A_S\rho_S\tau e^{\left(\frac{-E_s}{\bar{R}T_s}\right)}L_v + \rho_S c_p\frac{\partial T}{\partial t} = \dot{q}''_{in\ flame} \quad (6)$$

calculated for each time step in the drop and graphed. Examples of these energy balance curves are shown in Figure 44. In the plot, the large increase in energy represents flame

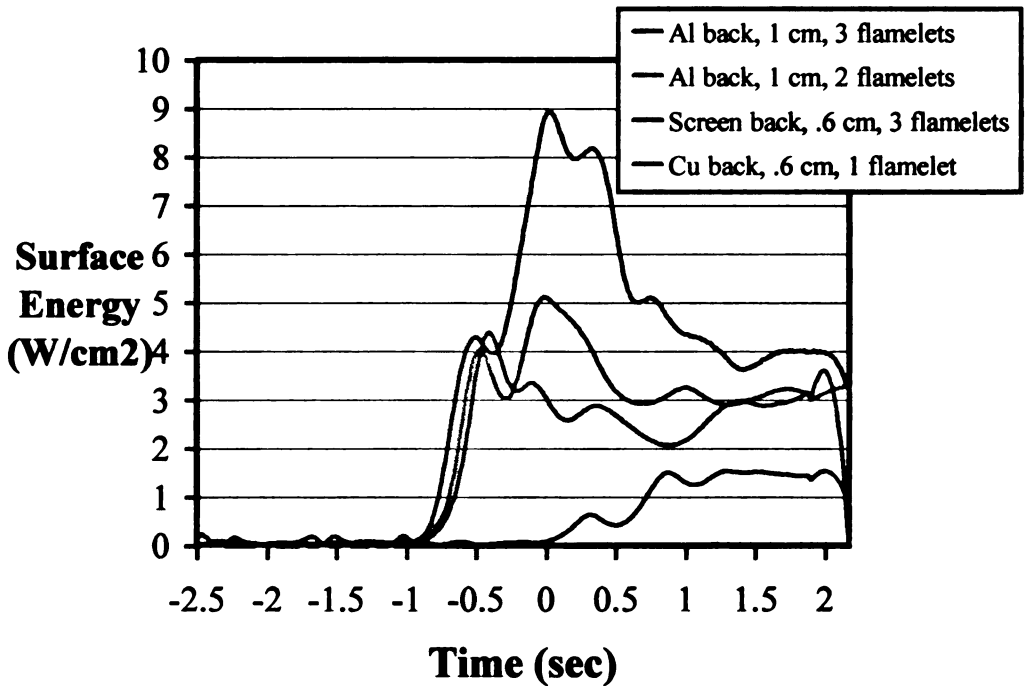

Figure 44. Typical surface energy balances for 2 second drops.

passage over the thermocouple (point on the surface where the data was recorded). At the beginning of the tests, the temperature of the fuel surface was room temperature. As the flame approached the thermocouple, the temperature of the surface increased in a very short period of time indicating the vaporization of fuel. Many tests like those in Figure 44 had energy values at the end of the drop larger than zero. This was most likely due to the fact that most drops ended while flamelets were still present. Therefore, the tail end of the flame would have still been traveling over the thermocouple, causing temperatures and consequently energy values exceeding atmospheric values.

Most drops had energy values between $1 W/cm^2$ and $10 W/cm^2$, which was consistent with previous studies of microgravity flames such as [27]. In Figure 44,

surface energies were compared for drops with different, substrates, substrate distances, and numbers of flamelets. Time zero was the beginning of the drop, and one flamelet denotes a uniform flame front that did not break apart. In Figure 44, the drop with three flamelets showed the surface to have larger amounts of energy losses than drops with fewer flamelets. This agreed with observations that tests with more flamelets were unstable compared to a stable uniform flame front because they were closer to extinction. It was also concluded that radiation terms dominated the energy balance, which agreed with current near limit extinction theory of flames. When compared with other energy terms, such as conduction, vaporization, etc., in all but one test radiation accounted for over eighty percent of the total energy contribution.

The above conclusions were the first step in assessing the validity of the measurements and preliminary calculations. In the future, a detailed gas phase energy balance will be attempted, so that a more comprehensive energy analysis can be completed. This will lead to a better understanding of the thermal diffusive (Lewis number effects) or hydrodynamic contributions to flame instabilities.

4.2.6 NASA Peak Temperature Surface Energy Balances

Surface energy values at the peak temperatures for tests versus the number of flamelets formed were analyzed. The goal was to see if a relationship between flamelet formation and energy existed. The peak temperature was chosen because in theory, it was the temperature that would most likely dictate the instability of the flame at the leading edge. In the energy balance from equation 18, the conduction from paper to

$$\sigma\varepsilon_s(T_{sp}^4 - T_b^4) + \frac{\sigma(T_{sp}^4 - T_b^4)}{(\frac{1}{\varepsilon_s} + \frac{1}{\varepsilon_b} - 1)} + \lambda_{air}\frac{(T_{sp} - T_b)}{L} + A_s\rho_s\tau e^{\left(\frac{-E_s}{RT_{sp}}\right)}L_v = q''_{net\,losses} \quad (18)$$

backing, radiation and reradiation from backing to surface, and vaporization terms were summed. The contribution from the change in total energy (time dependent term) was zero since at the peak temperature, the slope was zero. Therefore, the energy balance was really the maximum of net losses from the surface. These net losses equaled the incoming radiation and conduction from the flame.

The number of flamelets formed versus the peak energy losses for each test are shown in Figure 45. Since flamelets did not always pass over the thermocouple or

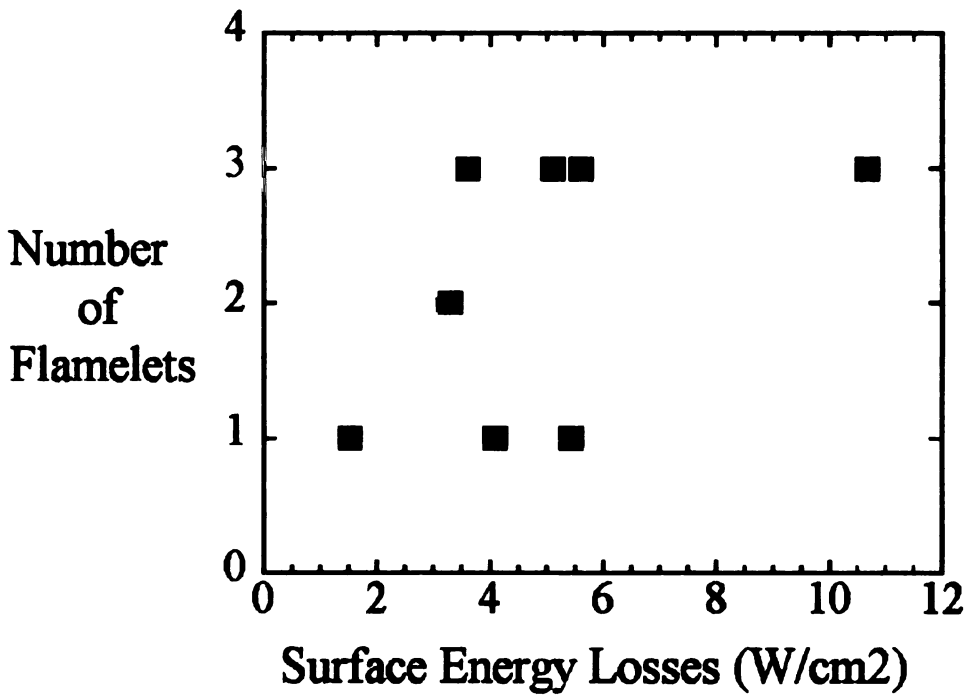

Figure 45. Number of flamelets versus peak energy losses.

thermocouples would break, not all drops were included in Figure 45. In the plot on the vertical axis, one flamelet corresponded to a single flame front. It was anticipated that the losses at the peak temperatures would be closely related to any flame instabilities. As

expected, a region between 3W/cm^2 and 6W/cm^2 of losses occurred at flamelet formation. However, the plot also implied that in tests with more flamelets, the flamelets had greater net losses than a single flame front that stretched across the sample. The two outlying points showed this: the test with the flame front, with losses of 1.5W/cm^2, and the test with three flamelets, with losses around 10W/cm^2. This was expected because flamelets were more unstable compared to uniform flame fronts, most likely because of large energy losses. The interesting feature of this plot is the qualitative feature that exhibited a critical net loss of energy at which flamelet formation occurred. There was a general critical region of losses between 3 and 6 W/cm^2 common to all tests, regardless of the number of flamelets. In this region, the large energy losses caused by the substrate made it difficult for the flame to survive, so the flame front had to fragment into smaller flames in order to exist. It is important to note that Figure 45 shows the beginnings of a qualitative trend, and more tests are needed to define a critical net loss quantity. Thus, this will be the basis for measuring surface energy losses in future tests as well as searching for gas phase energy connections with number of flamelets.

4.3 MSU Flame Rig Results and Discussion

4.3.1 MSU Flame Rig Flowmeter Verification

The in-line flowmeter, or rotameter, readings and correction and conversion factors explained in Chapter 3.3.3 were verified. The flowmeter readings were ultimately used for calculating the bulk test section velocity using mass conservation. This was accomplished using the calibrated sonic orifices for low flow velocities. The orifices came with a calibration sheet that gave the volumetric flowrate at standard conditions for

different upstream pressures. The calibrations were NIST (National Institutes of Standards and Technology) standard, so the given flowrates were precise.

Before determining if it was feasible to use the flowmeter in-line and correct for density changes, the flowmeter was validated under the environment that it was calibrated which was standard conditions. To do this, the pressure regulator, orifice, and flowmeter were placed in a line connected to the 95psig air supply. A block diagram of the setup is shown in Figure 46a. The losses of the tubing were considered negligible since the tube lengths were less than one foot. The flowmeter exhausted to atmosphere. Since the tubing was short and the flowmeter had negligible pressure losses, it was assumed that the downstream side of the orifice was at atmosphere. If the flowmeter were accurate, then the measurements from this setup would match the volumetric flow measurements of the calibrated orifice, since both were at standard conditions.

The flowmeter readings at atmospheric conditions compared well to the calibrated orifice readings shown in Figure 46b. Two orifice sizes were chosen to test the flowmeter. Since the flowmeter and orifice calibrations were at standard conditions, it was only necessary to compare volumetric instead of mass flowrates because the densities were the same. From Figure 46b, it was clear that the flowmeter worked properly. Volume flowrates for the meter working at standard conditions were very close to the calibrated values from the orifice. The flowmeter readings were slightly higher than the orifice readings. The average error between the flowmeter and calibrated values for both orifices was 6.5%. This was most likely because the resolution of the flowmeter was smaller by one factor of ten than the calibrated values of the orifices.

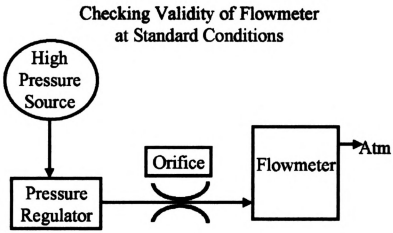

Figure 46a. Setup for verifying flowmeter at atmospheric conditions.

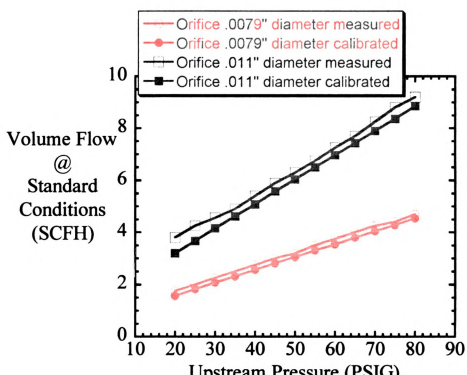

Figure 46b. Volume flowrates of flowmeter at atmospheric conditions for two orifices.

The next step was to test the validity of placing the flowmeter in-line and using the correction and conversion factors in Chapter 3.3.3 to calculate the correct mass flowrate. In this setup shown in Figure 47a, the flowmeter was being tested for its operation in-line, so it was placed before the orifice at pressures indicated by the pressure regulator. At pressures higher than atmospheric, the flowmeter had to be corrected for the change in density of the air moving through it by multiplying the flowrate times $(P_{atm}/P_{ac})^{1/2}$. This gave the actual flowrate at the in-line pressure. The actual flowrates were then converted to standard conditions (atmospheric) by multiplying the actual flowrate times (P_{ac}/P_{atm}). Therefore, the corrected and converted flowrates of the in-line flowmeter could be compared to the volumetric flowrates given by the calibrated orifice because both were at standard conditions. If it functioned properly, then the corrected and converted volumetric flowrates would be the same or close to calibrated orifice flowrates by mass conservation. The result of comparing the flowmeter with the previous used calibrated orifice with 0.011in. diameter is shown in Figure 47b. The smaller diameter orifice was not used because the flowmeter inline values were below the flowmeter scale and could not be determined.

From Figure 47b, the flowmeter measurements that were corrected for inline pressures and converted to atmopheric conditions were close to the calibrated values of the orifice. The corrected and converted meter values were generally lower than the calibrated values, and were not as accurate as measurements taken when the flowmeter was at atmospheric conditions. Larger deviations from calibrated values were seen as the pressure increased. However, the average error between measurements was 10%. Therefore, it was concluded that the flowmeter could be used to estimate the bulk

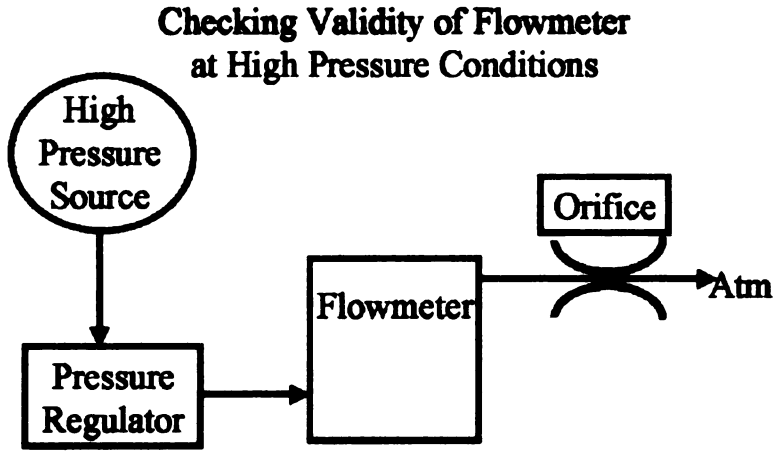

Figure 47a. Setup for verifying flowmeter at inline pressure conditions.

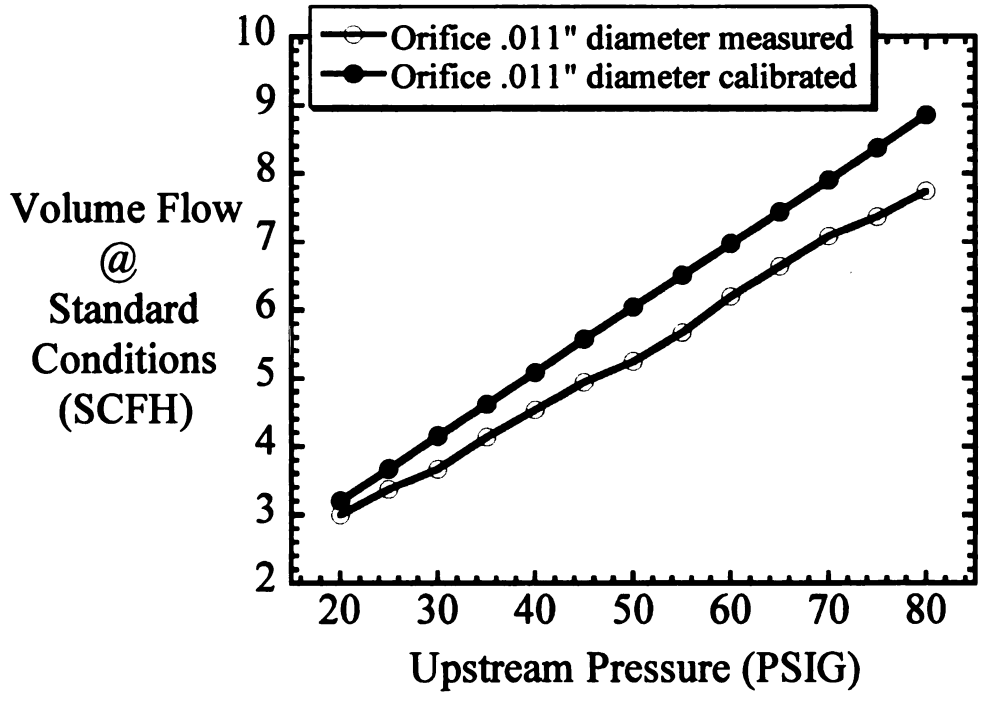

Figure 47b. Comparison of flowmeter to calibrated orifice at inline conditions.

velocity flow in the test section within 10%. This was acceptable because in the preliminary testing encompassing this thesis, approximate ranges of velocities where instabilities occurred were desired. After these ranges are confirmed, more sophisticated means of measuring test section velocity will be utilized. Also, to reduce error, tests were run at pressures of 60psig and below.

4.3.2 MSU Flame Rig Flame Instabilities

Preliminary testing in the MSU Flame Rig made it evident that many more dynamic instability behaviors may be seen in a zero gravity environment. The MSU Flame Rig produced flame instabilities similar to drop tower experiments, and additional unstable behaviors not seen in NASA tests. Initial flame fronts and flame instabilities required test section velocities above 10cm/s compared to NASA tests. Generally, instabilities were seen from 5-28cm/s, using predominantly the needle valve. As the flow velocity decreased below 28cm/s, the flame front corrugated and broke into smaller blue flames or yellow flamelets. A time sequence of a typical test in the MSU Flame Rig is shown in Figure 48. Times are located in the lower right corner of each frame. Total test times during which flame instabilities formed and developed were much longer than NASA tests. Most tests lasted 1-5min. Higher flowrates were needed in the MSU Flame Rig than in the NASA Rig in order to establish a flat flame front because there was no buoyant motion to feed the flame and the top plate of the test section was probably removing heat away from the flame. The top plate basically was forcing the flame into an enclosed area with a limited supply of oxygen, most likely not sufficient enough for ignition. Therefore, test section velocities as high as 30 to 40 cm/s were employed at ignition.

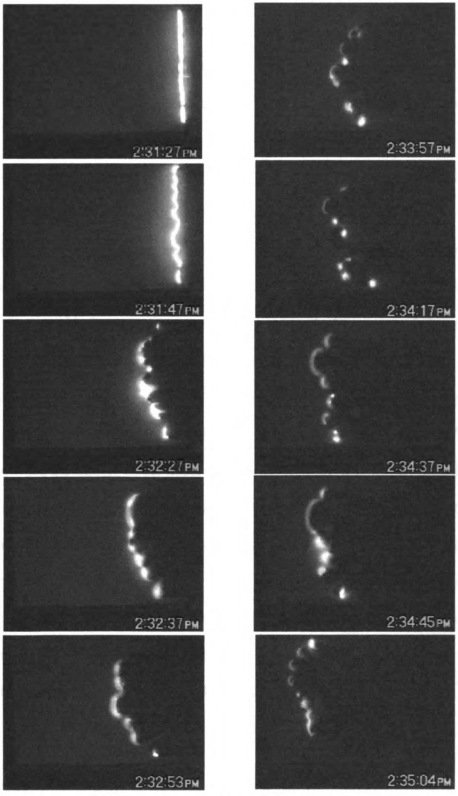

Figure 48. Typical progression of MSU Flame Rig test.

After a uniform flame front was generated across the sample, the flow was steadily and slowly decreased. In these tests, both heat loss and diminished oxygen supply produced the instabilities. As the oxidizer flow was reduced, distinct behaviors would occur. In some tests, the entire flame front slowly oscillated tracing out a sinusoidal motion like a standing wave produced by a string with fixed nodes. The flame front would then turn from yellow and sooty to a very thin and blue front that was on the order of a few millimeters in thickness. A time sequence of this is shown in Figure 49. Less than thirty frames per second were digitized from the MSU tests because more than this would give huge quantities of information when images were downloaded. Therefore, frames with the same time stamps are not identical frames, and they denote a change of the flame within one second. In Figure 49, the beginning front became corrugated like a sine wave at t=20 seconds. The flame front resembled a standing wave by oscillating throughout the test until it became a thin blue front. The "wave" motion can be seen when the middle of the flame that started concave with bulges on either side, would periodically protrude forward. When this happened, the flame bulges on the sides became flatter, and then it repeated, while thinning and becoming blue. The motion of the concave middle changing to flattening sides is shown from t=20 to 21sec., again from t=21 to 27sec., and again from t=28 to 40sec. The frames that show the most prominent concave middle with bulging sides were the first frame at t=20sec., the second frame at t=21sec., the first frame at t=29sec. At t=40sec., the flame is totally flat.

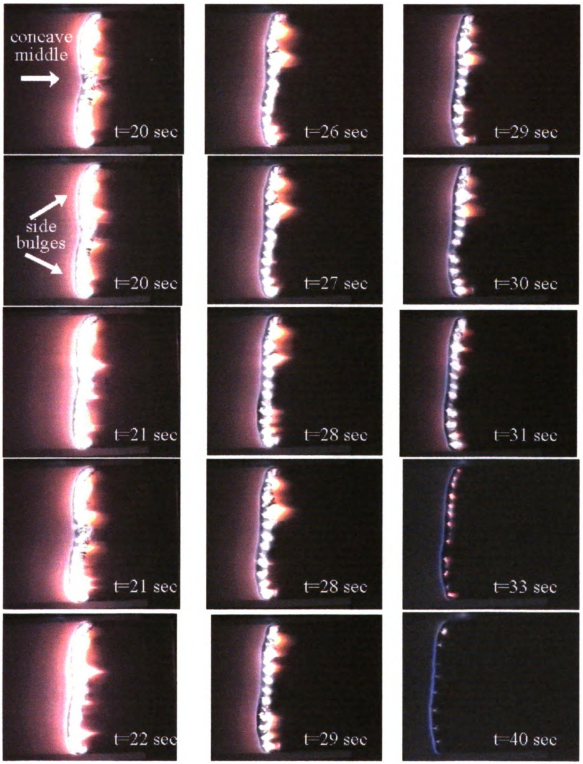

Figure 49. Oscillatory motion of entire flame front in MSU Flame Rig test.

After the flame front became thin and blue, small flames behind it sometimes remained. These would later turn into flamelets that generated a corrugated flame front with many smaller sine waves. Some flamelets survived while others extinguished. An example is in Figure 50.

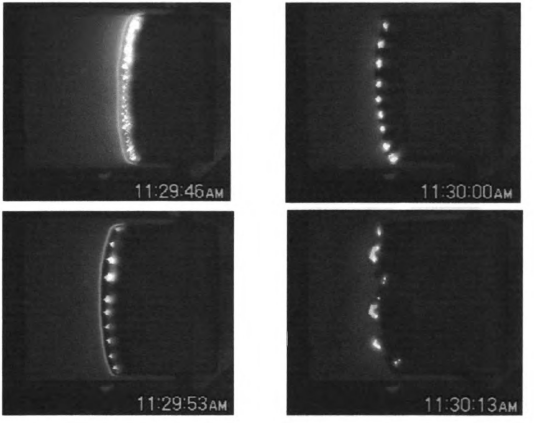

Figure 50. Time sequence of a uniform flame front changing into flamelets in MSU Flame Rig.

In other tests, very fast pulses traveled periodically across (parallel to) the initial flame front or across already formed flamelets. As the flame front advanced, there were also flashes of light moving across it. Figure 51 shows a time sequence of a test with

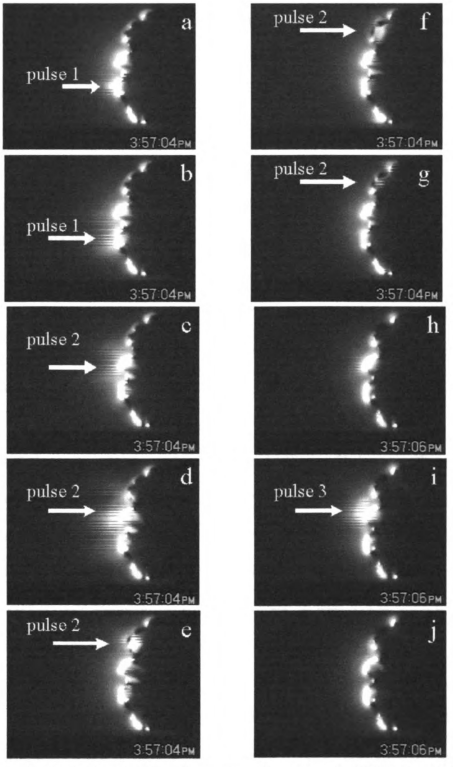

Figure 51. Periodic pulses travelling across flame front in MSU Flame Rig.

pulses moving across the flame. The pulses were in the region of the photos with bright lines. The lines appeared because the pulses were moving so fast that the camera could not capture them clearly. The pulses had a very fast frequency much larger than the drop tower flamelet oscillation frequencies, with one pulse usually proceeding across the flame in under a second. Therefore, the frames in Figure 51 were labeled from a to j to signify their order. Pulses usually originated at the middle of the sample and moved outwards disappearing at the edges. This was most noticeable from frames c to g. The bright pulse started in the middle in frame, and progressed upward in the picture to the sample edge. The pulse reached the edge in frame f as it is located under the last cusp at the top of the picture. In frame g, it was still present, but had lost intensity, and had disappeared in frame h. A third pulse commenced again in frame i, but was so fast that it disappeared in the last frame, j.

The tests with uniform flame fronts that exhibited sinusoidal curves, like in Figure 49, resembled the tests with the fast pulses like in Figure 51 because the sinusoidal motion was like a very slow pulse across the flame front. The trailing yellow sooty part of the flame in Figure 49 also exhibited sinusoidal behavior, moving like a slow pulse across the flame. In experiments with pulses, the flame front was usually yellow and sooty. Sometimes, both mechanisms would be present, as tests would begin with pulses and then progress to the slow sinusoidal motion, turning into the thin blue flame front.

The pulses moving across flamelets would sometimes cause the flamelets to extinguish. An example of this is shown in Figure 52. Again, the frames were labeled in order from a to j. In frame a, there were mini flame fronts or blue cusp flames burning over the sample. The first pulse, shown by the bright spot in frame b, occurred in the

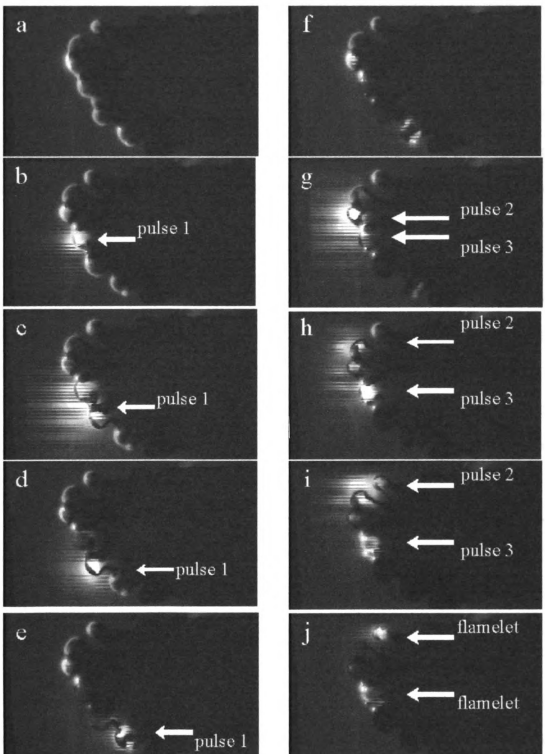

Figure 52. Periodic pulses that extinguish flamelets and flame fronts in MSU Flame Rig.

middle of the sample. As the pulse moved downward in the photo to the edge of the sample, shown in frames c through f, it extinguished the blue cusp flames, present in frame a. In frame g, two new pulses formed in the middle of the sample. Pulses 2 and 3 moved opposite each other to the edges of the sample. From this motion, pulse 2, which went upward in the photo, extinguished the remaining blue cusps on the upper side of the sample. However, after the two pulses had moved outwards, two flamelets remained and continued to burn over the sample. This quenching phenomenon resembled more the hydrodynamic instability, in that the motion of the pulse extinguished the flamelets or smaller blue cusp flames, like blowing out a candle. In NASA tests, when flames moved near each other, they usually combined. The larger flamelet would swallow the smaller and become bigger still. However, in the MSU Flame Rig, it was as though the force of the pulse created a blowout condition for the flamelet, in which the flow times were much larger than the chemical processes, so the flamelet could not sustain itself. Pulses rarely ever moved across the beginning uniform thin blue flame front.

After the flame pulsed or became thin and blue, it corrugated as oxidizer was reduced and broke apart into smaller flames that resembled the drop tower flamelets. The flamelet produced fingering patterns very similar to the smoldering combustion fingers seen by Zik [44]. An example of a test in which this action transpired is in Figure 53.

The flamelets in the MSU Flame Rig test oscillated, however, their frequencies were very fast compared to the drop tower flamelet frequencies. The oscillations were also a periodic increase and decrease in flamelet surface area, so it is likely that very similar controlling processes as in the drop towers flamelets are present in the MSU Flame Rig. The MSU flamelets were yellow, not blue like the drop tower tests. Some-

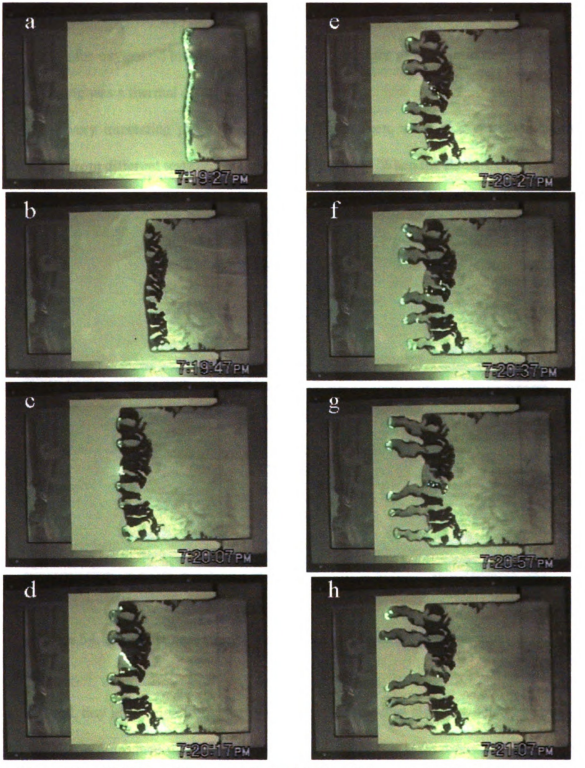

Figure 53. MSU Flame Rig test with unstable flamelets producing fingering pattern.

times the flamelets would extinguish, or if they were close enough, would recombine into a larger flame. Often, they did not recombine, implying that adjacent flamelets were competing for oxygen. This would affect the mass transfer of reactants, suggesting that the fingering was a thermal diffusive instability.

A very interesting phenomenon that was also seen, were blue crescent flames. Examples from different tests are illustrated in Figure 54. When the flame front became

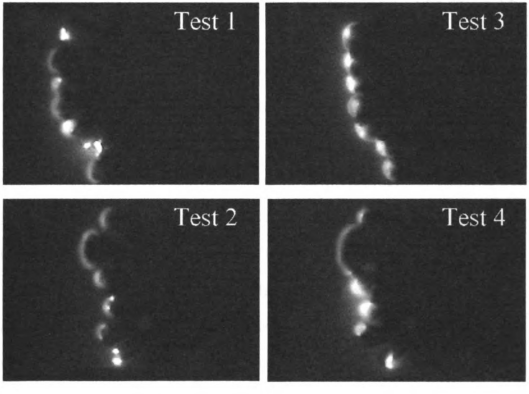

Figure 54. MSU Flame Rig tests with stable cusp flames and unstable flamelets.

corrugated, tiny blue flame fronts that were very thin and cusp shaped would form across the sample and produce the fingering pattern. In many cases, flamelets and blue cusps were present. All four tests in Figure 54 contained flamelets, which were the smaller yellow circular flames. Test 1 contained three flamelets, one at the top and two at the

bottom of the picture; Test 2 had one at the bottom; Test 3 showed flamelets across the whole sample, some behind the cusps; Test 4 had four at the bottom.

The cusp flames looked nearly identical to the stable blue oval flamelets with bright leading edges as seen in the drop tower tests. The difference though, was that the MSU tests did not have diffuse backs, only a leading edge or cusp. This may have been a result of the quartz plate prohibiting flow over the top of the flame. Therefore, there was no three dimensional oxygen-transport behind the flame. This would have been due to the flame filling most of the cross sectional area and preventing oxidizer flow over itself. The MSU Flame Rig blue cusps always had oval crescent fronts, not circular ones like some of the NASA flamelets. The oval shape of the cusps made them appear as mini-flame fronts like the oval flamelets in the NASA tests. The leading edge of the cusps acted again as a barrier to three-dimensional transport of oxygen that traveled from the sides to the back of the flame. This was because the flame front was not spherical, so the oxidizer could not be uniformly distributed to the back of the flame, so there were little or no chemical reactions in that area. The close proximity of the plate worked in conjunction with this to prevent oxidizer from flowing over the top of the flame. Thus there were no reactions behind the cusps compared to the diffuse backs of the flamelets in the drop towers.

Like the drop tower tests, the blue crescent flames were much more stable than the oscillating flamelets because they did not oscillate. In fact the flamelets would often oscillate very fast, and then flamelet would transform into a bright blue cusp. It appeared as though the flamelet oscillations provided the mechanism for gaining a more stable state. In some cases though, oscillations would result in extinction. One possible

explanation for the pulses across the flame front and sinusoidal nature was that the reduction of the oxidizer velocity was changing the time scales of the gas phase processes. As a result, it was possible that there existed different modes of frequency in flamelet instability behaviors. In the drop tower testing, 1Hz. may be the dominant frequency seen at the low time scales produced by the low velocities. In the MSU Flame Rig, there are higher oxidizer velocities, so it is possible that the dominant frequency of oscillation is much higher and the lower frequency behavior is present but can not be detected by simply looking at the video.

More interesting was the fact that the flamelets sometimes traveled along the underside of the fuel sample. The MSU Flame Rig was arranged so that oxidizer flowed across the top and bottom of the fuel sample. It was anticipated that the underside of the flame near the substrate would not be present like in the NASA tests. Instead, the flamelets were sometimes traveling closer to under the fuel than on the top of the sample. One explanation could be that the fuel char would curl under and obstruct the flow, producing an accumulation of oxidizer under the sample, and making a more favorable flame environment in that area. Future testing will employ ashless filter paper to try to remedy this. During some tests, the flamelets under the sample appeared as though they had extinguished, so all that was left was a finger. The flamelet would either extinguish or transform into a stable blue cusp that would appear along the finger on the top side of the sample. Since the cusps were more stable than flamelets, it is possible that they were able to survive above the sample where there may have been less oxidizer.

In some tests, the flat yellow flame front would turn into the thin blue front, which would continue to the end of the sample without corrugating. The flame front was

parabolic instead and did not break apart. An example of this is shown in Figure 55 with time stamps in the lower right corner. When the flame reached the edge of the sample, it

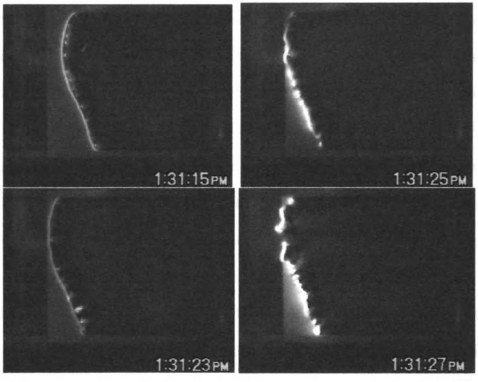

Figure 55. Burn out of sample by thin flame front in MSU Flame Rig.

was still thin and blue. If there were any flamelets behind the sample, oscillations began, as quick flashes of light. However, as soon as the fuel was totally consumed in the middle of the sample, the front turned from blue to sooty yellow as the remaining sides of the flame consumed the rest of the fuel. In these cases, the flame was acting like a barrier to the incoming oxidizer, so the flame was weak and blue. The oxygen was only being received from the direction of the leading edge of the flame. There was most likely no flow behind the flame front, so there was no multi-dimensional feeding of oxygen to the

flame. The flame, which stretched across the entire sample and was almost the width of the test section, resembled a solid object and also filled most of the cross sectional area of the test section. Therefore, the flow was forced to either become part of the chemical reaction or to pass around the sides of the flame. A solid object in this type of flow field would produce considerable drag behind it, causing many vortices and non-uniformity in the flow. It is possible that this was not sufficient to feed oxidizer behind the flame to turn it yellow and sooty. When the flame front split in two after the fuel burned out, a rush of oxygen flowed through the middle of the sample, which produced a more vigorously burning flame, indicated by the yellow color. This behavior helped to support the previous explanations that the stable blue cusps in the MSU Flame Rig and oval flamelets in the drop towers acted as barriers to the opposed oxidizer flow.

Flames in the MSU Flame Rig displayed many different instability processes. Different behaviors hinted at the particular type of instability mechanism. The oscillating flamelets pointed to a thermodiffusive instability because it is well known that this mechanism promotes bulges in flame fronts, due to imbalance in heat and mass diffusion. In the MSU Flame Rig, the bulges were exaggerated to the point that flamelets produced fingering patterns. Zik *et al.* [44] concluded that the smoldering fingering patterns were predominantly caused by a thermodiffusive mechanism because the finger flames competed for oxygen causing diffusion fields that were directed at the front and sides of the flame. This appeared to be likely in the MSU Flame Rig because a full-fledged finger flamelet rarely combined with an adjacent flamelet. However, the pulsing action of the flames implied a hydrodynamic mechanism because they were so powerful, that they sometimes extinguished the weak flames in the vicinity. The pulsing action was not seen

in the NASA tests, in which the flow was constant. The MSU Flame Rig induced unstable flames using both heat loss and reduced flow, so it was likely that both instability mechanisms existed. Further quantitative testing is needed in the future.

4.3.3 Discussion of MSU Flame Rig versus Drop Towers.

The similarity of flame instabilities seen in the MSU Flame Rig to those in the NASA drop towers show that it is possible to use a Hele-Shaw apparatus as a supplement to studying microgravity flames. This does not mean that Hele-Shaw devices can or should replace drop towers. As with all experiments, there are definite unwanted side effects. The Hele-Shaw apparatus is not in a true zero gravity environment. It only simulates it, at the expense of having a large heat sink very near the top of the burning sample. This could be affecting the heat flux and energy processes of the flame. Furthermore, a Hele-Shaw apparatus will always produce very viscous dominated flow due to the close proximity of the two plates. In many cases, researchers would like to have a uniform flow profile across their samples. To obtain any resemblance of bulk plug flow, higher velocities are needed. However, this would undermine the effect of the tunnel since flows well above buoyancy driven flows are required because the purpose of the apparatus is to simulate flows that are not larger than buoyant velocities in any direction. Despite these limits, there are definitely advantages of the MSU Flame Rig. Most importantly, unlike the drop towers, test times are unlimited. Consequently, instabilities of thicker fuels can be tested, since it is very difficult to produce them in the drop towers due to slow spread rates. Also, the oxidizer velocity can be varied *in situ*, and very wide samples of many widths may be incorporated. The fact that the flame instabilities in the MSU Flame Rig resemble those in the drop towers supports the use of

this device for microgravity experiments. In effect, coupled with drop tower or airplane experiments, the MSU Flame Rig can be very helpful in gaining more information about thin and thick fuel instabilities under simulated microgravity conditions.

CHAPTER 5
CONCLUSIONS

Instability regions of flames in microgravity spreading over a thin solid fuel were found for different substrate backing materials. The unstable nature was shown when a flat flame front would corrugate and then break into flamelets. The flamelets oscillated, recombined, or extinguished, and always traveled in the direction of the opposite oxidizer flow. Oscillations were on the order of 1Hz., which was comparable to microgravity candle results. Line profile measurements showed oscillatory, unstable behavior of the intensity of the flamelets in the blue region. Flamelet spread rates for different substrate distances were usually less than microgravity flame spread rates. Substrate spacing affected microgravity flame spread rates and also determined the existence of flames on the backside of the sample. An energy balance at the fuel surface during the drop produced flux values that were of the same order as previous studies. More importantly, when peak surface energy flux values were compared with number of flamelets for each drop, an area where there was a "cutoff" flux was evident. This critical region may provide some indication of the minimum energy of the flamelets. These preliminary tests and measurements in the NASA drop towers revealed an instability regime of microgravity flames that can survive at flow rates near those on the Space Station and Space Shuttle. Such flames could possibly compromise the safety of the people onboard these vehicles. In effect, the need for further studies to determine the underlying processes of unstable microgravity flame behavior was demonstrated.

Using fluid dynamic principles, a Hele-Shaw device called the MSU Flame Rig was successfully constructed which was capable of producing low opposed flow

velocities, variable test section heights, and a burning sample on the floor of the test section in order to simulate flame spread in a low buoyant atmosphere. The flowmeter readings of the device were verified so that approximate bulk flow velocities could be determined in the test section. The wind tunnel incorporates various fuel widths, and a substrate backing for thin samples, whose distance was variable. A successful igniter system was fabricated that produced flat flame fronts like NASA tests. These flame fronts became corrugated and broke into flamelets similar to drop tower results when the flowrate was decreased. Flamefronts were blue, with yellow flamelets. Additional dynamic processes were present in the MSU Flame Rig, as the very thin flame front would often oscillate as a whole, like a standing wave or sinusoidal curve. The flame front also broke into tiny flames, which oscillated at frequencies higher than flamelet frequencies in NASA tests. Fingerlike smoldering also occurred analogous to previous works. Generally, many different frequencies and unstable behaviors in the MSU Flame Rig were present for flames in the near extinction limit regime. Observations suggested that both the thermal diffusive and hydrodynamic mechanisms affected flame instabilities. The MSU Flame Rig appears to be a very valuable tool for studying flame spread rates in a reduced buoyant atmosphere. It will aid in the selection of thick fuels to be tested on the International Space Station. The MSU Flame Rig showed that weak flames can survive under low flow conditions common to many everyday environments as well as those on the Space Station. Further studies of the flame mechanisms in the MSU Flame Rig may give some indication of flame behavior in zero gravity environments, helping to ensure the safety of persons living and working in enclosed microgravity environments.

CHAPTER 6
FUTURE WORK

This thesis was a preliminary portion of a "Flight Definition" project called ATHINA for NASA Glenn Research Center Microgravity Combustion Branch and MSU. Work is in progress to incorporate additional diagnostics in the Combustion Tunnel Rig (CTR) so more knowledge of the flame instability nature will be gained. In particular, the igniter system that inspired the MSU Flame Rig design has been added to the CTR. A gas phase energy balance will supplement the solid fuel balance to determine the energy processes controlling flamelet formation. Particle Image Velocimetry (PIV) measurements are being tested in normal gravity, leading to the development of a system on the CTR. The PIV will help to determine the multidimensional flow fields of the flame. Heat flux sensors are also being tested to measure flame heat fluxes. Fuels similar to the filter paper will be tested. Drop tower testing will help to determine the conditions and necessary equipment for tests on the International Space Station (ISS). Airplane (KC135) experiments that provide approximately twenty seconds of microgravity will help determine selection of thicker fuels that can be tested on the ISS.

For the MSU Flame Rig, a definite range of instability conditions for four different thin fuels will be determined. Thermocouple measurements will give fuel surface and substrate temperatures for energy balance calculations. A hotwire placed near the test section opening will be calibrated to the flowmeter, so unsteady flow rates can be measured. The hotwire will also indicate the fluctuation intensities in the test section. Due to low Reynolds numbers, it is unlikely that any genuine turbulence exists there. More sophisticated flowmeters will be incorporated in the apparatus, as well as pressure transducers. Microphones or other devices capable of measuring the pulse

frequencies and flamelet oscillations will be tested at different locations in the test section. Since the ranges of velocities where instabilities occur has been obtained, the next step will be to set the velocity at one value (as in the NASA tests) and try to produce a flame front that corrugates into unstable fingering patterns. Then the NASA tests and MSU tests can be more closely compared. Most importantly, fuels thicker than paper will be tested and instability ranges recorded. Computer simulations using CFD software will be attempted to model a simplified system with comparisons to experimentation.

BIBLIOGRAPHY

BIBLIOGRAPHY

1. Burke, S. P., and Schumann, T. E. W., 1928, "Diffusion Flames," *Industrial & Engineering Chemistry,* Vol. 20(10), pp. 998-1004.

2. deRis, J. N., 1969, "Spread of a Laminar Diffusion Flame," *Twelfth Symposium (International) on Combustion,* The Combustion Institute, pp. 241-252.

3. Friedman, R., 1993, "Fire Safety Practices in the Shuttle and the Space Station Freedom," *Proceedings of the Second International Microgravity Combustion Workshop,* N93-20204, Cleveland, OH, Sept. 15-17, pp.213-225.

4. Dietrich, D. L., Ross, H. D., Shu, Y., Chang, P., and T'ien, J. S., 2000, "Candle Flames in Non-Buoyant Atmospheres," *Combust. Sci. and Tech.,* Vol. 156, pp. 1-24.

5. Olson, S. L., 1997, "Buoyant Low Stretch Stagnation Point Diffusion Flames over a Solid Fuel," Ph.D. Thesis, Case Western Reserve University.

6. Olson, S. L., Baum, H. R., and Kashiwagi, T., 1998, "Finger-Like Smoldering over Thin Cellulosic Sheets in Microgravity, *"Twenty-Seventh Symposium (International) on Combustion,* The Combustion Institute, pp. 2525-2533.

7. deRis, J. N., 1968, "The Spread of a Diffusion Flame over a Combustible Surface," Ph.D. Thesis, Harvard University.

8. McAlevy, R. F., and Magee, R. S., 1969, "The Mechanisms of Flame Spreading over the Surface of Igniting Condensed-Phase Materials," *Twelfth Symposium (International) on Combustion,* The Combustion Institute, pp. 215-227.

9. McAlevy, R. F., Magee, R. S., and Wrubel, J. A., 1967, "Flame Spreading at Elevated Pressures over the Surface of Igniting Solid Propellants in Oxygen/Inert Environments," *Meeting of the Western States Section of the Combustion Institute.*

10. Lastrina, F. A., Magee, R. S., and McAlevy, R. F., 1971, "Flame Spread over Fuel Beds: Solid-Phase-Energy Considerations," *Thirteenth Symposium (International) on Combustion,* The Combustion Institute, pp.935-948.

11. Magee, R. S., and McAlevy, R. F., 1971, "The Mechanism of Flame Spread," *J. Fire Flammability,* Vol. 2, pp. 271-297.

12. Friedman, R., 1968, "A Survey of Knowledge About Idealized Fire Spread over Surfaces," *Fire Res. Abstr. Rev.,* Vol. 10, pp. 1-8.

13. Sirignano, W. A., 1972, "A Critical Discussion of Theories of Flame Spread Across Solid and Liquid Fuels," *Combust. Sci. Technol.*, Vol. 6, pp. 95-105.

14. Sirignano, W. A., 1974, "Theory of Flame Spread Above Solids," *Acta Astronaut.*, Vol. 1, pp. 1285-1299.

15. Feng, C. C., and Sirignano, W. A., 1977, "Further Calculations Based Upon a Theory of Flame Spread Across Solid Fuels," *Combust. Flame,* Vol. 29, pp. 247-263.

16. Fernandez-Pello, A. C., and Williams, F. A., 1975, "Laminar Flame Spread over PMMA Surfaces," *Fifteenth Symposium (International) on Combustion,* The Combustion Institute, pp. 217-231.

17. Fernandez-Pello, A. C., and Williams, F. A., 1977, "A Theory of Laminar Flame Spread over Flat Surfaces of Solid Combustibles," *Combust. Flame,* Vol. 28, pp. 251-277.

18. Parker, W., 1972, "Flame Spread Model for Cellulosic Materials," *J. Fire Flammability,* Vol. 3, pp.259-269.

19. Hirano, T., and Kinoshita, M., 1975, "Gas Velocity and Temperature Profiles of a Diffusion Flame Stabilized in the Stream over a Liquid Fuel," *Fifteenth Symposium (International) on Combustion,* The Combustion Institute, pp. 379-387.

20. Hirano, T., and Kanno, Y., 1973, "Aerodynamic and Thermal Structures of the Laminar Boundary Layer over a Flat Plate with a Diffusion Flame," *Fourteenth Symposium (International) on Combustion,* The Combustion Institute, pp. 391-398.

21. Frey, A. E., and T'ien, J. S., 1979, "A Theory of Flame Spread over a Solid Fuel Including Finite-Rate Chemical Kinetics," *Combust. Flame,* Vol. 36, pp. 263-289.

22. Altenkirch, R. A., Eichhorn, R., and Shang, P. C., 1980, "Buoyancy Effects on Flames Spreading Down Thermally Thin Fuels," *Combust. Flame,* Vol. 37, pp. 71-83.

23. Wichman, I. S., 1992, "Theory of Opposed-Flow Flame Spread," *Prog. Energy Combust. Sci.*, Vol. 18, pp. 553-593.

24. Olson, S. L., Ferkul, P. V., T'ien, J. S., 1988, "Near Limit Flame Spread over a Thin Solid Fuel in Microgravity," *Twenty-Second Symposium (International) on Combustion,* The Combustion Institute, pp. 1213-1222.

25. Bhattacharjee, S., Altenkirch, R. A., Srikantaiah, N., and Vedha-Nayagam, M., 1990, "A Theoretical Description of Flame Spreading over Solid Combustibles in a Quiescent Environment at Zero Gravity," *Combust. Sci. and Tech.*, Vol. 69, pp. 1-15.

26. Olson, S. L., 1991, "Mechanisms of Microgravity Flame Spread over a Thin Solid Fuel: Oxygen and Opposed Flow Effects," *Combust. Sci. and Tech.*, Vol. 76, pp. 233-249.

27. Bhattacharjee, S., Altenkirch, R. A., Olson, S. L., Sotos, R. G., 1991, "Heat Transfer to a Thin Solid Combustible in Flame Spreading at Microgravity," *Transactions of the ASME (Journal of Heat Transfer)*, Vol. 113, pp. 670-676.

28. Altenkirch, R. A., Bhattacharjee, S., Olson, S. L., Sacksteder, K., 1993, "Opposed-Flow Flame Spreading in Reduced Gravity," *Proceedings of the Second International Microgravity Combustion Workshop*, N93-20206, Cleveland, OH, Sept. 15-17, pp.237-243.

29. Bhattacharjee, S., Altenkirch, R. A., Sacksteder, K., 1996, "The Effect of Ambient Pressure on Flame Spread over Thin Cellulosic Fuel in a Quiescent, Microgravity Environment," *Transactions of the ASME (J. Heat Transfer)*, Vol. 118, pp. 181-190.

30. Blackshear, P. L., and Murty, K. A., 1967, "Some Effects of Size, Orientation, and Fuel Molecular Weight on the Burning of Fuel Soaked Wicks," *Eleventh Symposium (International) on Combustion*, The Combustion Institute, pp. 545-552.

31. Orloff, L., and deRis, J., 1971, "Modeling of Ceiling Fires," *Thirteenth Symposium (International) on Combustion*, the Combustion Institute, pp. 979-992.

32. Chan, W. Y., and T'ien, J. S., 1978, "An Experiment on Spontaneous Flame Oscillation Prior to Extinction," *Combust. Sci. and Tech.*, Vol. 18, pp. 139-143.

33. Kirkby, L. L., and Schmitz, R. A., 1966, "An Analytical Study of the Stability of a Laminar Diffusion Flame," *Combust. Flame*, Vol. 10, pg. 205.

34. Baliga, B. R., and T'ien, J. S., 1975, "Unsteady Effects on the Low Pressure Extinction Limit of Solid Propellants," *AIAA J.*, Vol. 13(12), pp. 1653-1656.

35. Chao, B. H., Law, C. K., and T'ien, J. S., 1990, "Structure and Extinction of Diffusion Flames with Flame Radiation," *Twenty-Third Symposium (International) on Combustion*, The Combustion Institute, pp. 523-531.

36. Chen, R. H., Bradley Mitchell, G., Ronney, P. D., 1992, "Diffusive-Thermal Instability and Flame Extinction in Nonpremixed Combustion," *Twenty-Fourth Symposium (International) on Combustion*, The Combustion Institute, pp. 213-221.

37. Linan, A., 1974, "The Asymptotic Structure of Counterflow Diffusion Flames for Large Activation Energies," *Acta Astronaut.*, Vol. 1, pp. 1007-1039.

38. Kim, J. S., 1996, "Diffusional-Thermal Instability of Diffusion Flames in the Premixed-Flame Regime," *Combust. Sci. and Tech.*, Vol. 118, pg. 27-48.

39. Kim, J. S., 1997, "Linear Analysis of Diffusional-Thermal Instability in Diffusion Flames with Lewis Numbers Close to Unity," *Combust. Theory & Modeling,* Vol. 1, pp. 13-40.

40. Cheatham, S., and Matalon, M., 1996, "Near-Limit Oscillations of Spherical Diffusion Flames," *AIAA J.*, Vol. 34(7), pp.1403-1409.

41. Matalon, M., 1999, "Instabilities in Non-Premixed Combustion," *Thirty-Seventh AIAA Aerospace Sciences Meeting and Exhibit,* AIAA 99-0584, Reno, NV, Jan. 11-14.

42. Potter, M. C., and Foss, J. F., 1982, Fluid Mechanics, Great Lakes Press, Inc., Okemos, MI, pp. 392-393.

43. Bejan, A., 1995, Convection Heat Transfer, Second Edition, Wiley-Interscience, New York, pp. 252-256, pp.48-49, pp.159-161.

44. Zik, O., Olami, Z., Moses, E., 1998, "Fingering Instability in Combustion," *Phys. Rev. Lett.*, Vol. 81, pg. 3868-3871.

45. Ivanov, A. V., 1997, "A Study of Material's Combustion Processes in Microgravity," *Russian Space Agency Keldysh Research Center,* Technical Report No. 2625, on treaty No. 920/9-5208/95:400-I/34-95 project TM-9.

46. Olson, S. L., 1997, Combustion Tunnel User's Guide, *NASA Glenn Research Center.*

47. Baines, W. D., and Peterson, E. G., 1951, "An Investigation of Flow Through Screens," *Transactions of the ASME,* Vol. 73, pp. 467-480.

48. Prandtl, L., 1932, "Herstellung einwandfreier Luftstrome (Windkanale)," *Handbuch der Experimentalphysik,* Vol. 4, part. 2, pg. 73, *(NACA Technical Memorandum No. 726).*

49. McMasters, R. L. IV, 1997, "Modeling Heat Transfer for Parameter Estimation in Flash Diffusivity Experiments," Ph.D. Thesis, Michigan State University.

50. Murio, D., 1993, The Mollification Method and the Numerical Solutions to Ill Posed Problems, Wiley-Interscience, New York.

51. Omega Engineering, Inc., 1995, The Flow and Level Handbook, Vol. 29, Omega Engineering, Inc., Stamford, CT.

52. Miller, R. W., 1989, Flow Measurement Engineering Handbook, Second Edition, McGraw Hill, Inc., New York, pp.(14-46)-(14-58).

53. The ASME Special Research Committee on Fluid Meters, 1971, Fluid Meters Their Theory and Application, *Report of the American Society of Mechanical Engineers Research Committee,* Sixth Edition, editor Howard Bean, The American Society of Mechanical Engineers, New York, pp. 81-89.

54. Arpaci, V. S., and Larsen, P. S., 1984, Convection Heat Transfer, Prentice-Hall, Inc., New Jersey, pp. 146-150.

55. Wichman, I. S., and Olson, S. L., 1998, "Investigation of Diffusion Flame Tip Thermodiffusive and Hydrodynamic Instability Under Microgravity Conditions," *Research Proposal submitted in response to NASA Research Announcement NRA-97-HEDS-01, Microgravity Combustion Science: Research and Flight Experiment Opportunities.* Accepted and funded Jan. 1999 under contract number NCC3-662, Project Monitor Dr. Fletcher Miller.